DISSERTATION
submitted to the
Combined Faculties for the Natural Sciences and for Mathematics
of the Rupertus Carola University of
Heidelberg, Germany
for the degree of
Doctor of Natural Sciences

presented by
Diplom-Geoökologe Olaf Ippisch
born in Fürth

Oral examination: 19th December, 2001

Coupled Transport in Natural Porous Media

Referees: Prof. Dr. Kurt Roth
              Prof. Dr. Peter Bastian

Gekoppelte Transportprozesse in natürlichen porösen Medien

Da die Wechselwirkungen zwischen verschiedenen Transportprozessen für eine Reihe interessanter Systeme wichtig sind, wurde ein System partieller Differentialgleichungen und effektiver Parameterfunktionen für die Untersuchung des gekoppelten Wasser-, Wärme-, Gas- und Stofftransportes formuliert und in einem State-of-the-Art Computermodell implementiert. Dabei wurde für die Beschreibung des gekoppelten Gas-/Wassertransportes eine neue Druck/Druckformulierung entwickelt.

Mit dem Modell wurde der Wasser- und Energiehaushalt eines Permafrostbodens simuliert, wobei die wesentlichen Phänomene reproduziert werden konnten. Unterschiede lassen sich durch Heterogenität und die Sensitivität des Modells auf die Änderung der hydraulischen Parameter erklären. Während Wasserdampf- und Stofftransport keine Auswirkung auf das Ergebnis der Simulation hatten, erwies sich der Transport flüssigen Wassers als wichtig für den Energietransport nahe dem Gefrierpunkt.

Bei der Untersuchung der Auswirkung der gewählten Parametrisierung und des verwendeten Modells auf die Simulation eines Multistep Outflow Experiments zeigten sich Unterschiede zwischen Richardsgleichung und Zweiphasen-Modell nur bei Verwendung einer Brooks-Corey Parametrisierung. Mit dem Zweiphasen-Modell ergab sich dann eine langsamere Entwässerung und eine Hysterese beim Aufsättigen, was gut mit experimentellen Befunden übereinstimmt.

Coupled Transport in Natural Porous Media

As the interactions between transport processes are important for a number of interesting systems, a set of partial differential equations and appropriate parameter functions for the study of coupled water, heat, gas and solute transport was formulated and a state of the art computer model for the numerical solution of the equation system was created. A new phase pressure/partial pressure formulation for the coupled transport of liquid and gas phase was developed.

The model was used to simulate the water and energy dynamics of a permafrost soil. A good qualitative agreement was achieved. Differences between modeled and measured data could be explained with heterogeneity in combination with the model's sensitivity to a change in hydraulic parameters. Water vapor and solute transport had no effect on the simulation result but transport of liquid water proved to be an important heat transfer process near 0 °C.

The impact of the chosen parameterization and model on the simulation of a multistep outflow experiment was analyzed. Differences between a model based on Richards' equation and a twophase model only occurred when the Brooks-Corey parameterization was used. The results of the twophase model showed a retarded drainage and a hysteresis during imbibition which is in good agreement with experimental results.

Acknowledgments

In our endeavor to understand reality we are somewhat like a man trying to understand the mechanism of a closed watch. He sees the face and moving hands, and even hears the ticking, but he has no way of opening the case. If he is ingenious enough he may form some picture of a mechanism which could be responsible for all the things he observes, but he may never be quite sure his picture is the only one which could explain his observations.
    – Einstein and Infeld (1966) –

It is not possible to finish a research project like this without the help of a lot of people. So it's time now to say thank you to

- Kurt Roth for his support, his many helpful suggestions and for many extended discussions (not only) about soil physics.

- Peter Bastian as he always had a helping hand when I got stuck with some numerical problems.

- Julia Boike, who is not only an excellent field scientist and a valuable colleague, but a close friend I would not want to miss.

- Hans-Jörg Vogel for lots of encouragement and professional support.

- Paul Ouverduin for great times in Ny Ålesund and San Francisco and the proof reading of this work.

- Hans Graf for the permission to use data measured at the 'HSPM'.

- Ute Wollschläger. She often helped me to keep a realistic view.

- Marco Bittelli with whom I had some inspiring discussions about freezing soils.

- Hermann Lauer, Mihael Brajdic and Günter Balschbach for the assistance in the installation of a Linux cluster and in the common struggle against all types of computer problems.

- all colleagues at the University of Hohenheim and the Institut für Umweltphysik in Heidelberg.

- the Alfred-Wegener-Institute.

- all my personal friends, who helped me through some difficult times.

- the "unknown helper" as a substitute for all the people I forgot to mention.

Finally I'd like to thank my family. Without their support it would not have been possible for me to finish my study.

Contents

Contents

List of Figures

Notation

Scalar values, functions and sets are denoted by normal letters (e.g. $p_l, k_r, S_i, \ldots$). Vectors are typeset in boldface symbols (e.g. $\mathbf{x}$), whereas tensors are written in boldface italic letters (e.g. $\boldsymbol{K}$).

Lowercase Latin Symbols

b_i, b_j	Control volumes
b_i^k, b_j^k	Sub control volumes
∂b_i	Boundary of control volume i
c_l^a	Concentration of dissolved air in the liquid phase [mole/m^3]
c_l^s	Concentration of solute in the liquid phase [mole/m^3]
$c_{l_i}^s$	Concentration of solute species i in the liquid phase [mole/m^3]
c_l^w	Concentration of water in the liquid phase [mole/m^3]
$e_1,\ldots,e_k$	Elements
$\mathbf{e}_j$	Unity vector
f_{S_i}	Damping parameter of ice on liquid phase permeability [–]
g_a, g_b, g_c	Form factors for the de Vries model [–]
h_m	Matrix head [m]
j^a	Molar air flux [mole m^{-2} s^{-1}]
j^e	Energy flux [W/m^{-2}]
$j_{\mathrm{conv}_l}^e$	Convective energy flux in the liquid phase [W/m^{-2}]
$j_{\mathrm{conv}_g}^e$	Convective energy flux in the gas phase [W/m^{-2}]
j_{lat}^e	Latent heat flux [W/m^{-2}]
j_{cond}^e	Conductive energy flux [W/m^{-2}]
j_g^i	Total flux of component i in the gas phase [mole m^{-2} s^{-1}]
j_l^i	Total flux of component i in the liquid phase [mole m^{-2} s^{-1}]
$j_{g_D}^i$	Molar flux of component i in the gas phase due to molecular diffusion [mole m^{-2} s^{-1}]
j_N^k	Flux at Neumann boundary
j^s	Molar solute flux [mole m^{-2} s^{-1}]
j^w	Molar water flux [mole m^{-2} s^{-1}]

j^w_{infreeze}	Water flux between the high flow domain and the normal liquid phase [mole m^{-2} s^{-1}]
$k^{O_2}_H$	Henry coefficient for oxygen [Pa]
$k^{N_2}_H$	Henry coefficient for nitrogen [Pa]
k^i_H	Henry coefficient of gas i [Pa]
k^i	Ratio of the average temperature gradient in particles of type i to the average temperature gradient in the surrounding medium [–]
k_{r_g}	Relative permeability of the gas phase [–]
k_{r_l}	Relative permeability of the liquid phase [–]
$k_{r_{l_{\text{hf}}}}$	Relative permeability of the high flow domain [–]
n	Van Genuchten parameter [–]
$\mathbf{n}^k_{ij}$	Outward directed normalized vector normal to γ^k_{ij}
m	Van Genuchten parameter [–]
p_{ad}	Capillary pressure above which adsorption forces are prevalent [Pa]
p_{atm}	Gas pressure in the free air above the soil [Pa]
p_{cap}	Capillary pressure below which capillary forces are prevalent [Pa]
p^a_g	Partial pressure of air [Pa]
p_c	Capillary pressure [Pa]
p_e	Air entry pressure [Pa]
p_g	Gas phase pressure [Pa]
p^w_g	Partial pressure of water [Pa]
p_l	Liquid phase pressure [Pa]
p^i_g	Partial pressure of gas i [Pa]
q^a	Air source/sink term [mole m^{-3} s^{-1}]
q^e	Energy source/sink term [W/m^{-3}]
q_l	Volumetric liquid phase flux [m^3/s]
q^s	Solute source/sink term [mole m^{-3} s^{-1}]
q^w	Water source term [mole m^{-3} s^{-1}]
r	Pore radius [m]
rH	Humidity [–]
t	Time [s]
v_l	Pore water velocity [m/s]
v^w_l	Molar volume of liquid water [m^3/mole]
v^w_i	Molar volume of ice [m^3/mole]
$\mathbf{x}_i$	Position of vertex i
$\mathbf{x}^k_{ij}$	Barycenter of sub-control volume face i
z	Height [m]
z_0	Reference height [m]

Uppercase Latin Symbols

A	Flux term
C_s	Volumetric heat capacity of the matrix [J m^{-3} K^{-1}]
C_g^a	Molar heat capacity of air [J mole^{-1} K^{-1}]
C_g^w	Molar heat capacity of water vapor [J mole^{-1} K^{-1}]
C_i^w	Molar heat capacity of ice [J mole^{-1} K^{-1}]
C_l^w	Molar heat capacity of liquid water [J mole^{-1} K^{-1}]
D_g^i	Dispersion coefficient of component i in the gas phase [m^2/s]
D_l^i	Dispersion coefficient of component i in the liquid phase [m^2/s]
D_g^{ij}	Binary diffusion coefficient of components i and j in the gas phase [m^2/s]
$D_{g_T}^w$	Diffusion coefficient for water vapor transport due to a temperature gradient [mole m^{-1} s^{-1} K^{-1}]
$D_{g_{pc}}^w$	Diffusion coefficient for water vapor transport due to a moisture gradient [mole s m^{-1} kg^{-1}]
$D_{g_\text{atm}}^w$	Diffusion coefficient for water vapor transport in free air [m^2/s]
E	Energy density [J/m^3]
F_{ij}^k	Area of sub-control volume face [m^2]
ΔH_{lg}^w	Molar phase change enthalpy of water vapor at reference temperature [J/mole]
ΔH_{il}^w	Molar phase change enthalpy of ice at reference temperature [J/mole]
$\boldsymbol{J}$	Jacobi matrix
J_g	Volumetric convective flux of the gas phase [m/s]
J_l	Volumetric convective flux of the liquid phase [m/s]
$\boldsymbol{K}_l$	Hydraulic conductivity [m^3 s kg^{-1}]
$\boldsymbol{K}_g$	Gas phase conductivity [m^3 s kg^{-1}]
M	Storage term
M_i	Molar mass of component i [kg/mole]
M_w	Molar mass of water [kg/mole]
Q	Source term
R	Ideal gas constant [J mole^{-1} K^{-1}]
S	Saturation [–]
S_{e_g}	Effective gas phase saturation [–]
S_{e_l}	Effective liquid phase saturation [–]
S_g	Gas phase saturation [–]
S_i	Ice phase saturation [–]
S_l	Liquid phase saturation [–]
S_{l_hf}	Liquid phase saturation of the high flow domain [–]
S_{r_g}	Residual gas phase saturation [–]

S_{r_l}	Residual liquid phase saturation [–]
S_l^w	Entropy of liquid water [J/K]
S_i^w	Entropy of ice [J/K]
S_{tot}^w	Total water saturation (liquid water plus ice) [–]
T	Temperature [K]
V_i^k	Volume of sub-control volume [m³]
$(\nabla T)_g$	Average temperature gradient in the gas phase [K/m]
X_l^w	Molar fraction of water in the liquid phase [–]
X^i	Volumetric fraction of component i [–]
X_l^i	Molar fraction of gas i in the liquid phase [–]

Lowercase Greek Symbols

α	Van Genuchten parameter [Pa^{-1}]
α	Exponent in mixing formula [–]
α_h	Heat exchange parameter [W m^{-2} K^{-1}]
χ_g	Stress partition factor for the gas phase [–]
χ_i	Stress partition factor for the ice phase [–]
χ_l	Stress partition factor for the liquid phase [–]
ϵ_a	Relative permittivity of air [–]
ϵ_i	Relative permittivity of ice [–]
ϵ_m	Relative permittivity of the soil [–]
ϵ_s	Relative permittivity of the soil matrix [–]
ϵ_w	Relative permittivity of water [–]
η_i	Parameter function
γ	Contact angle [–]
γ_{ij}^k	Sub control volume face
λ	Brooks-Corey parameter [m]
λ	Heat conductivity [W m^{-1} K^{-1}]
λ_0	Heat conductivity of the surrounding medium [W m^{-1} K^{-1}]
λ^i	Heat conductivity of component i [W m^{-1} K^{-1}]
λ_*	Heat conductivity of a soil without vapor transport [W m^{-1} K^{-1}]
λ_{eff}	Effective heat conductivity of a soil [W m^{-1} K^{-1}]
μ_l	Dynamic viscosity of the liquid phase [Pa s]
μ_g	Dynamic viscosity of the gas phase [Pa s]
ν^a	Total molar density of air [mole/m³]
ν_g^a	Molar density of air in the gas phase [mole/m³]
ν^s	Total molar density of solute [mole/m³]
ν^w	Total molar density of water [mole/m³]
ν_g^w	Molar density of water in the gas phase [mole/m³]
ν_i^w	Molar density of ice [mole/m³]

$\nu_{g_0}^w$	Molar density of saturated water vapor above a solution [mole/m^3]
$\nu_{g_0}^{w\bullet}$	Molar density of saturated water vapor above pure water [mole/m^3]
ν_g^i	Molar density of component i in the gas phase [mole/m^3]
ϕ_i	Nodal basis function i
ψ_g	Gravitational potential [J/m^3]
ρ_g	Density of the gas phase [kg/m^3]
ρ_l	Density of the liquid phase [kg/m^3]
ρ_l^w	Density of liquid water [kg/m^3]
σ_e	Effective stress [Pa]
σ_n	Neutral stress [Pa]
σ_{la}	Surface tension of the liquid phase/air phase interface [J/m^2]
θ_w	Volumetric water content [–]
τ	Tortuosity in the Mualem model [–]
$\upsilon_i,\ \upsilon_j$	Vertices
ξ	Tortuosity factor [–]
ξ_g	Tortuosity factor for the gas phase [–]

Uppercase Greek Symbols

Γ	Model boundary
Ω	Model domain
Φ	Porosity [–]
Π_o	Osmotic pressure [Pa]

Norms, Operators

∇	Divergence operator
∇	Gradient operator

Indices

e	Energy
$g,\ l,\ i$	Gas, liquid, ice phase
s	Soil matrix

Exponents

a, w, i, s Components: air, water, ice, solute
k Control volume
n Index for discretized time

1 Introduction

Coupled transport processes are important for two rather different but nevertheless very relevant environmental problems: Global warming and the pollution of groundwater.

Water, heat and solute transport processes are strongly coupled in freezing or thawing soils. As a significant part of the earth's continental area ($\sim$ 25 % of the exposed land surface in the Northern Hemisphere, Zhang et al. 1999) is underlain by permafrost[1] and permafrost soils are an important storage of organic carbon and methane, a thawing of wide areas could lead to a dangerous feedback for global climate change (Goulden et al. 1998). A 12 to 15 % reduction of the near-surface permafrost area and a 15 to 30 % increase of the active layer[2] thickness is indicated by recent modeling studies (Anisimov and Nelson 1996, Anisimov and Nelson 1997, Anisimov et al. 1997) for the middle of the 21st century. For the prediction of the future development of climate, the understanding of the water and heat dynamics of permafrost soils is therefore of great significance. The possibility to simulate the response of permafrost soils to global warming would facilitate reliable climate predictions.

Many permafrost soils are heterogeneous due to slow weathering and periglacial mixing processes in cool climates. An adequate description therefore requires at least two-dimensional models. However most of the models commonly used are either one-dimensional (Nakano and Brown 1972, Jansson 1998, Flerchinger and Saxton 1989, Padilla and Villeneuve 1992, Shoop and Bigl 1997, Zhao et al. 1997) or they are intended for the modeling of frost heave and ice lense development and have a simplified description of water and energy transport (O' Neill and Miller 1982, Fowler and Krantz 1994, Selvadurai et al. 1999, Li et al. 2000).

Another problem of great environmental and economic importance is the pollution of groundwater. Computer models based on Richards' equation (Richards 1931) are often used to predict the transport of dissolved chemicals (especially pesticides, fertilizers and heavy metals). However, the interaction of gas phase and liquid phase is assumed to be negligible in the derivation of Richards' equation. This is not true at high water saturations, which can occur during infiltration events and are of great

---

[1]Permafrost is defined as ground or substrate that is continuously below 0 °C for two or more years (National Research Council of Canada 1988).

[2]The active layer is the temporarily unfrozen part at the surface of a permafrost soil.

importance for the transport of contaminants.

The objective of this study is the development of a flexible, stable and robust model with state-of-the-art numerical solvers to study the coupled water, heat, solute and gas transport in frozen and unfrozen soils at the laboratory to plot scale. Two- and three-dimensional simulations must be possible in order to represent the heterogeneity of a soil. Although mechanical processes are important in freezing soils, they are not considered explicitly, as this would be beyond the scope of this study. However, the possibility to integrate a mechanical model later was accommodated in the development. The model is used to simulate the heat and water dynamics of a permafrost site near Ny Ålesund, Spitsbergen and of laboratory experiments commonly used to estimate the water transport properties of soils.

2 Theory of Coupled Transport Processes in Porous Media

A set of equations for the description of coupled mass and energy transport in frozen and unfrozen soil and porous media is developed in this chapter. A discussion of basic concepts is followed by the formulation of balance equations, flux laws and the specification of parameter functions.

2.1 System Description

Soils are complex dynamic entities. The soil surface usually has some microrelief and is covered by different types of vegetation. Horizontal layers, soil horizons, of varying size and extension can be seen in the soil profile. The horizons are often composed of lumps of material called aggregates separated by a network of pores. The aggregates themselves are a mixture of different mineral components with smaller pores in between. Water, heat and solutes are transported, ions and organic molecules adsorbed and released, minerals are decomposed and newly created, and the soil is populated by an incredible variety of bacteria, insects and animals. Under the influence of climate, the soil structure is changed by swelling and shrinking, freezing and thawing.

In this study soil is envisaged as a porous medium composed of a solid matrix and an interconnected pore space filled with water, air and solutes. Water, solutes and dissolved air (the consideration of dissolved air is necessary to solve some numerical difficulties) form the liquid phase[1] and the gas phase consists of air and water vapor. The components[2] are transported by diffusion and convective transport processes in liquid and gas phase. Energy is associated with the heat capacity of the components

---

[1] A phase is defined as a "chemically and physically uniform or homogeneous quantity of matter that can be separated mechanically from a nonhomogeneous mixture and that may consist of a single substance or of a mixture of substances" (Encyclopaedia Britannica 2001). In this study, besides the soil matrix, a liquid, gas and ice phase are considered

[2] A component is defined by Bear and Bachmat (1991) as part of a phase that is composed of an identifiable homogeneous chemical species or of an assembly of species (ions, molecules). The three components water, air and one solute are used in this work.
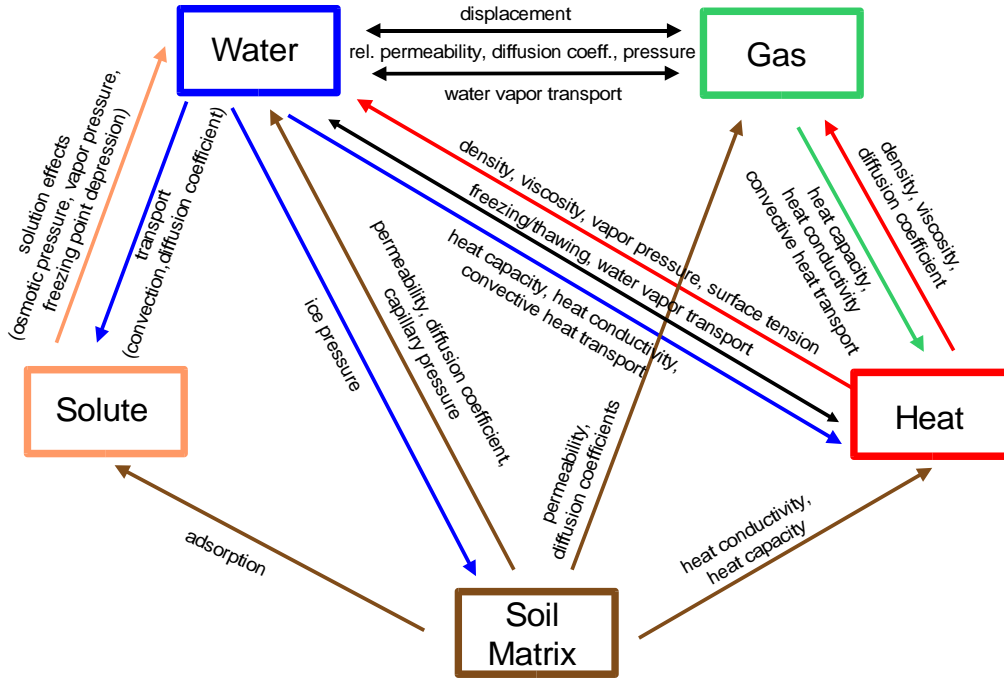
Figure 2.1: The main elements of a natural porous medium and their interactions as considered in this work

and the phase change of water. Mass movements and heat conduction transport energy. Figure 2.1 shows the main elements and their interactions.

For simplicity, a detailed analysis of solute transport is not performed. Only the transport of one solute, representing ionic strength, is taken into account. Mechanical interactions are also not considered in detail. Although they might be quite important in freezing porous media, the complexity of the interactions is beyond the scope of this work.

2.2   Basic Considerations

2.2.1   Continuum Approach

The observable phenomena and their description are closely linked to the resolution with which an porous medium is analyzed. At least three scales can be distinguished.

Molecular scale
At the molecular scale the interactions between individual atoms and molecules in the pore space and the solid material are treated explicitly. Interesting variables

are the velocity and mass of the molecules, their rotation, and the distribution of electrical charges. Interaction is dominated by electrical forces either on large distances if charged particles or surfaces are involved, or in the short range, when atoms or molecules collide.

Pore scale

The motion of individual molecules can be averaged, if the mean free path length[3] is much larger than the scale of interest. Positions, velocities and molecular masses are replaced by continuous state variables like density, pressure or temperature. Regions with a distinct change in state variables (e.g. in density: liquid/gas) are called phases. In a porous medium normally more than one phase coexist (gas phase/liquid phase/solid phase). Molecules may be able to change from one phase to another.

If the mean free path length is large compared to the pores of the solid, transport can be described by Knudsen diffusion. Interactions between molecules in the pore space and the solid material (including the geometry of the solid material) are lumped into the Knudsen diffusion coefficient.

If the mean free path length is much smaller than the pore diameter, the Navier-Stokes equations can be applied. The average interactions between molecules in the mobile phase are described by the effective parameters viscosity and diffusion coefficient. The surface properties and geometry of the pore space must be treated by appropriate boundary conditions. High resolution measurements of the geometry of the pore space are limited to small sample volumes. The speed of available computers also sets tight bounds to the size of a sample which can be simulated with a pore scale model.

Continuum scale

On the continuum scale phases are treated as continuous fields. At each point of space there are no longer distinct phases, but fractions of different phases. The phases are not mixed but microscopic geometry is no longer resolved (Figure 2.2). Phase boundaries and the geometry of the pore space are taken into account by new effective parameters like permeability. Transition from pore scale to continuum scale is possible if the pore space is either homogeneous above a certain scale or heterogeneities are hierarchical. The applicability of a continuum scale model for porous media is therefore closely linked to the existence of a so called "representative elementary volume" (REV).

---

[3]The mean free path length is defined as the mean distance a molecule travels before hitting another molecule
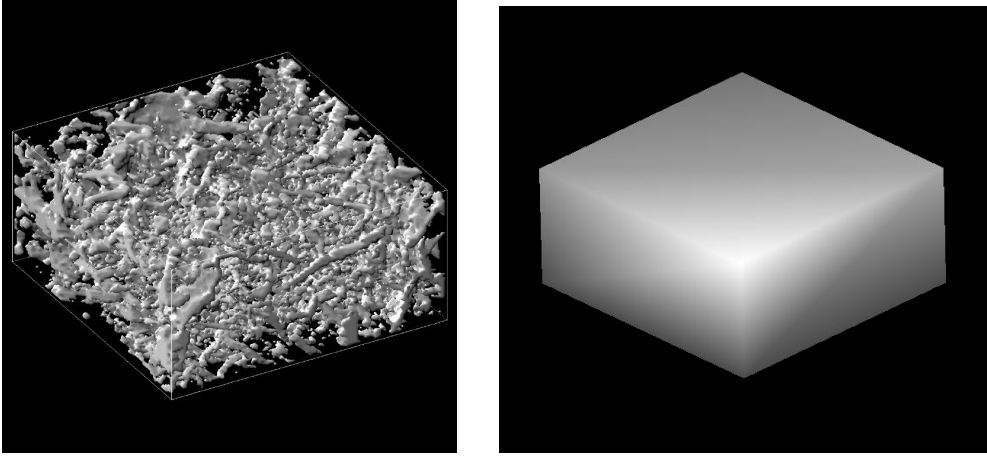
Figure 2.2: Schematics representation of a porous medium at pore scale (left) and continuum scale (right)

2.2.2   Representative Elementary Volume

If a horizontal pressure gradient in x-direction is applied to a water saturated soil column, the water transport is often described with Darcy's law (Darcy 1856):

$$q_l = -K_l \cdot \frac{\partial\, p_l}{\partial\, x}, \tag{2.1}$$

where q_l is the volumetric flux, K_l is a material specific parameter called hydraulic conductivity and p_l is the liquid phase pressure. If we know the flux and pressure field at the pore scale, we can calculate K_l at a certain position by averaging over a certain volume. If the averaging volume is gradually increased, we might get a result similar to figure 2.3. For small averaging volumes the variations are quite large, as changes of velocity and pressure can be very large at small distances (either large pores, small pores or solid material are included). With increasing volume less new information is incorporated. The variations are getting smaller until a plateau may be reached. If we increase the volume even further the value might change again, because of large scale heterogeneities. The plateau exists only, if the pore space is homogeneous at least at some intermediate scale. The smallest volume at which the average value does no longer change significantly with changing averaging volume is called "representative elementary volume" (cf. Bear 1972).

The REV can be different for different effective parameters (porosity, hydraulic conductivity, ...). Transport in a porous medium can only be described at the continuum scale, if a common REV for all necessary effective parameters exists. In general the existence of an REV can not be proven easily for a specific porous medium. The applicability of a macroscale description must be verified by comparison of results from experiment and simulation.
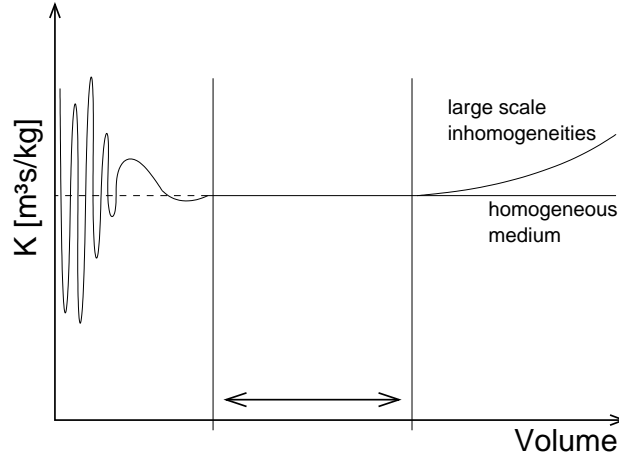
Figure 2.3: Change of hydraulic conductivity with increasing averaging volume. The conductivity is essentially constant in the marked interval

Heterogeneity due to changes of composition or pore space geometry at a larger scale can be considered by using different sets of effective parameters for each region. Effective parameters can also have tensorial character (e.g. permeability) to represent directional differences in the structure of the pore space.

2.2.3 Further Assumptions

The following basic assumptions are made in the description of the system:

- Air can be treated as a single gas. Oxygen, nitrogen and carbon dioxide are not treated separately. Air and water vapor are assumed to be ideal gases.

- Dissolved air and the modeled solute can be considered to be ideal solutes. In the solution they behave exactly like water molecules.

- Local thermodynamic equilibrium is assumed. Kinetic effects are not taken into account.

2.3 Balance Equations

To derive continuum scale transport equations, the principle of mass and energy conservation is used to formulate balance equations for each component.

For a non-isothermal system consisting of water, gas and one solute we get a system of four partial differential equations:

$$\frac{\partial \nu^w}{\partial t} + \nabla \cdot j^w = q^w \tag{2.2}$$

7

$$\frac{\partial \nu^a}{\partial t} + \nabla \cdot j^a = q^a \tag{2.3}$$

$$\frac{\partial \nu^s}{\partial t} + \nabla \cdot j^s = q^s \tag{2.4}$$

$$\frac{\partial E}{\partial t} + \nabla \cdot j^e = q^e \tag{2.5}$$

with ν^w, ν^a, ν^s: Molar density of water, air, solute [mole/m^3]
       E: Energy density [J/m^3]
       j^w, j^a, j^s: Molar flux (water/air/solute) [mole m^{-2} s^{-1}]
       j^e: Energy flux [W/m^{-2}]
       q^w, q^a, q^s: Source/sink term (water/air/solute) [mole m^{-3} s^{-1}]
       q^e: Energy source/sink term [W/m^{-3}]

2.3.1   Storage Terms

The total mass of a component is calculated as sum over the phases. If we assume that the gas phase is composed of water vapor and air, the liquid phase of water, solute and dissolved air and the ice phase of pure water, we get the storage terms:

$$\nu^w \;\; = \;\; \Phi \cdot \left(S_g \cdot \nu_g^w + S_l \cdot c_l^w + S_i \cdot \nu_i^w \right) \tag{2.6}$$

$$\nu^a \;\; = \;\; \Phi \cdot \left(S_g \cdot \nu_g^a + S_l \cdot c_l^a \right) \tag{2.7}$$

$$\nu^s \;\; = \;\; \Phi \cdot S_l \cdot c_l^s \tag{2.8}$$

with Φ: Porosity [–]
       S_g, S_l, S_i: Phase saturation[4] (gaseous/liquid/ice) [–]
       ν_g^w, ν_g^a: Molar density of water and air in the gas phase [mole/m^3]
       c_l^w, c_l^a, c_l^s: Concentration[5] of water, air, solute in the liquid phase [mole/m^3]
       ν_i^w: Molar density of ice [mole/m^3]

Energy storage can be computed from porosity, phase saturations and the heat capacity of the components. As we use liquid water at 0 °C as reference state, the phase change enthalpy of water vapor and ice must be taken into account as well. If we use the phase change enthalpies at the reference temperature in this storage equation, the phase change enthalpy varies with temperature in the model due to the different heat capacity of ice, water and vapor. Figure 2.4 shows a comparison of the resulting temperature dependence of the phase change enthalpy of ice with a formula fitted to experimental results (Spaans and Baker 1996). As we assume an

---

[4]The saturation is defined as the fraction of pore space occupied by a phase.
[5]The term concentration is used instead of the term molar density in solutions, as the concentration also depends on the composition of the liquid phase.
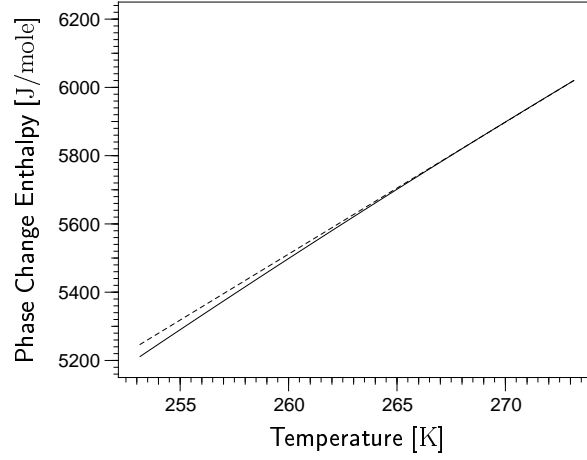
Figure 2.4: Molar enthalpy of the phase change liquid water/ice resulting from the balance equation (dashed line) and fitted to measured values (solid line)

ideal solution, dissolved molecules behave like water molecules and the molar heat capacities C_l^a, C_l^s and C_l^w are identical.

$$
\begin{aligned}
E \;=\; & T \cdot \left\{ \Phi \cdot \left[S_l C_l^w \left(c_l^w + c_l^a + c_l^s \right) + S_g \left(C_g^a \nu_g^a + C_g^w \nu_g^w \right) + S_i C_i^w \nu_i^w \right] \right. \\
& \left. + (1 - \Phi) \cdot C_s \right\} + \Delta H_{lg}^w \Phi S_g \nu_g^w - \Delta H_{il}^w \Phi S_i \nu_i^w
\end{aligned}
\tag{2.9}
$$

with
T: Temperature [K]
C_l^w, C_g^w, C_g^a, C_i^w: Molar heat capacities (liquid water,vapor,air, ice) [J mole^{-1} K^{-1}]
C_s: Volumetric heat capacity of the matrix [J m^{-3} K^{-1}]
ΔH_{lg}^w, ΔH_{il}^w: Molar phase change enthalpies of water vapor and ice at reference temperature [J/mole]

2.3.2   Flux Laws

The formulation of flux laws is a central step in the development of a model. One possibility is the definition of a potential for every component and the calculation of the flux as product of the negative gradient of the potential and an effective parameter. For water the "hydraulic potential" is defined as the energy difference between bound water in a porous medium with dissolved solutes and free, pure water at a reference height. However this potential can hardly be measured and as an integral quantity it is also difficult to calculate. The gravitational potential for example is usually (e.g. Kutilek and Nielsen 1994) given as $\psi_g = \rho_l^w g(z - z_0)$. This is only correct if the density of water is constant. If the density varies, a term $g(z - z_0)\nabla \rho_l^w$ would occur in $\nabla \psi_g$ besides the gravity force $\rho_l^w g\,\mathbf{e}_z$, where $\mathbf{e}_z$ is the

9

unity vector in z-direction. The correct expression for ψ_g in the case of varying density is $\int_{z_0}^{z} \rho_l^w(z)gdz$.

An alternative approach specifies the transport processes and relates them to gradients of state variables which can be measured. Water for example is transported by convection[6] driven by gravity and the gradient of liquid phase pressure, and by diffusion[7]. In laboratory experiments the liquid phase pressure can be measured with tensiometers and pressure transducers. At very low water contents water is transported in liquid films on solid surfaces. As this is normally included into the calculation of convection, the liquid phase pressure may also become negative. This reminds us that further research on water transport in very dry porous media is needed. The resulting transport equations are:

$$J_l \;=\; -\boldsymbol{K}_l(S_l)\cdot(\nabla p_l - \rho_l \cdot g) \tag{2.10}$$

$$j_l^i \;=\; c_l^i \cdot J_l - D_l^i \cdot \nabla \nu_l^i \tag{2.11}$$

$$J_g \;=\; -\boldsymbol{K}_g(S_g)\cdot(\nabla p_g - \rho_g \cdot g) \tag{2.12}$$

$$j_g^i \;=\; \nu_g^i \cdot J_g - D_g^i \cdot \nabla \nu_g^i \tag{2.13}$$

with $J_g,\,J_l$:   Volumetric convective flux of the gas/liquid phase [m/s]

$\rho_l = \sum\limits_{i=w,a,s} c_l^i M_i$:   Density of the liquid phase [kg/m^3]

$\rho_g = \sum\limits_{i=w,a} \nu_g^i M_i$:   Density of the gas phase [kg/m^3]

M_i: Molar mass of component i [kg/mole]

$\boldsymbol{K}_l(S_l),\,\boldsymbol{K}_g(S_g)$:   Liquid/gas phase conductivity tensor [m^3 s kg^{-1}]

p_l: Liquid phase pressure [Pa]

$p_g = \sum\limits_{j=w,a} p_g^j$:   Gas phase pressure [Pa]

$p_g^w,\,p_g^a$:   Partial pressure of water/air [Pa]

g: Acceleration of gravity [m/s^2]

$j_l^i,\,j_g^i$:   Total flux of component i in the liquid/gas phase [mole m^{-2} s^{-1}]

$D_l^i,\,D_g^i$:   Dispersion coefficient of component i in the liquid/gas phase [m^2/s]

Equation 2.10 is equivalent to the Darcy-Buckingham-Equation (Buckingham 1907).

Energy is transported either by convection of the gas and liquid phase, as latent heat with water vapor or by heat conduction. This processes can be described by (de Vries 1958):

$$j^e = j^e_{\mathrm{conv}_l} + j^e_{\mathrm{conv}_g} + j^e_{\mathrm{lat}} + j^e_{\mathrm{cond}} \tag{2.14}$$

---

[6]Convection is defined as transport of a phase as a whole

[7]Diffusion is defined as transport of molecules, resulting from concentration gradients, relative to a frame of reference in which the phase as a whole is stationary

where

$$
\begin{aligned}
j^e_{\text{conv}_l} &= T \cdot C^w_l \cdot J_l & (2.15) \\
j^e_{\text{conv}_g} &= T \cdot \sum_{i=w,a} C^i_g \cdot j^i_g & (2.16) \\
j^e_{\text{lat}} &= \Delta H^w_{lg} \cdot j^w_g & (2.17) \\
j^e_{\text{cond}} &= -\lambda(S_l, S_g) \cdot \nabla T & (2.18)
\end{aligned}
$$

with $\lambda(S_l, S_g)$: Heat conductivity [W m^{-1} K^{-1}].

2.3.3 Multiphase Transport and Richards' Equation

Liquid and gas phase transport are coupled as they share the same pore space. Due to its smaller viscosity, the gas phase is much more mobile than the liquid phase. It is often assumed that the gas phase is mobile enough to be always (nearly) at atmospheric pressure and to be no obstacle to the liquid phase flow. Gas and liquid phase transport can then be decoupled. The result is Richards' equation (Richards 1931), which is identical to the combination of equations 2.2, 2.6 and 2.10 if $p_g = p_{\text{atm}}$ is used in the calculation of S_l.

2.4 Effective Parameters

To fill the flux laws and balance equations with life, we have to specify the effective parameters used in the calculation of storage terms and in the flux laws.

2.4.1 Soil Water Characteristic

In experiments a strong relationship between the water content of a porous medium and the pressure difference between liquid and gas phase is observed. This relation will be called "soil water characteristic" in this work. The pressure difference between gas and liquid phase pressure is called "capillary pressure" $p_c = p_g - p_l$ as water is bound by capillary forces at high saturations. A gas phase develops in a pore if the capillary pressure is higher than the entry pressure p_e of the pore

$$
p_e = \frac{2\sigma_{la}\cos(\gamma)}{r}. \tag{2.19}
$$

with σ_{la}: surface tension of the liquid phase/air phase interface [J/m^2]
γ: contact angle [–]
r: pore radius [m]

With increasing capillary pressure smaller and smaller pores drain. At very high capillary pressures, water retention is no longer caused by effects of capillarity, but by interaction between solid surfaces and water films.

The soil water characteristic is generally highly nonlinear. It is also often strongly hysteretic, which may be a result of of gas phase entraption and/or varying contact angles between a receding or advancing wetting front.

It is convenient to represent the soil water characteristic by a parameterization fitted to the measured data. The two most popular models have been formulated by van Genuchten (1980) and by Brooks and Corey (1966).

If we define an effective saturation S_{e_l}

$$S_{e_l} = \frac{S_l - S_{r_l}}{1 - S_{r_l} - S_{r_g}}, \tag{2.20}$$

the van Genuchten model is given by

$$S_{e_l} = [1 + (\alpha p_c)^n]^{-m} \tag{2.21}$$

and the Brooks-Corey parameterization is

$$S_{e_l} = \begin{cases} (p_c/p_e)^{-\lambda} & p_c \geq p_e \\ 1 & p_c < p_e \end{cases}. \tag{2.22}$$

S_{r_g}, S_{r_l}, α, n, m, λ and p_e are empirical parameters. S_{r_g} and S_{r_l} are called residual gas and water saturation and m is often assumed to be $m = 1 - \frac{1}{n}$. Both parameterizations approach each other for $\alpha p_c \gg 1$ if $\alpha^{-1} = p_e$ and $mn = \lambda$. p_e is the entry pressure associated with the biggest pores in the porous medium connected to the gas phase. The van Genuchten model does not consider an entry pressure, which implies the assumption of the existence of a fraction of pores with infinite diameter.

2.4.1.1 Temperature Dependence

As the soil water characteristic is a result of capillary effects in moist porous media it should change with the temperature dependence of surface tension. Döll (1996) gives a thorough review of literature on the temperature dependence of the water characteristic and comes to the conclusion that "it appears that the surface tension model for the temperature dependence of the water retention curve underestimates the effect of temperature by a factor of 1 to 8. This factor seemingly decreases with increasing saturation, but is more or less independent of temperature." As possible reasons she mentions entrapped air, different behavior of soil solution and pure water and influence of temperature on the contact angle γ (Equation 2.19). As no definite explanation exists which makes a calculation of the effect possible, only the temperature dependence of capillary pressure will be considered in this work. The water characteristic is scaled according to the formula:

$$S_l(p_c, T) = S_l(\frac{p_c}{\sigma_{\mathrm{rel}}^*(T)}) \tag{2.23}$$

with

$$\sigma_{\text{rel}} = \sigma_w(T)/\sigma_w(T_0)$$

$$\sigma_{\text{rel}}^* = \begin{cases} 1.0 & p_c \geq p_{\text{ad}} \\ 1.0 + \frac{(p_c - p_{\text{ad}})}{(p_{\text{cap}}\sigma_{rel} - p_{\text{ad}})} & p_{\text{ad}} > p_c > p_{\text{cap}}\sigma_{rel} \\ \sigma_{rel} & p_c \leq p_{\text{cap}}\sigma_{rel} \end{cases} . \tag{2.24}$$

This scaling takes care of the fact that capillary effects are not relevant for water in very small pores, where liquid adsorption on solid surface prevails. p_{ad} is the capillary pressure above which the soil water characteristic is dominated by surface adsorption and the soil water characteristic doesn't have to be scaled any more due to changes of surface tension. p_{cap} is the potential below which the soil water characteristic is dominated by capillary forces. Values of $1.5 \cdot 10^7 Pa$ and $1.5 \cdot 10^8 Pa$ were chosen for p_{cap} and p_{ad}, which correspond to pore radii of 10 and 1 nm. T_0 is the temperature at which the soil water characteristic was measured. With a standard deviation of ± 0.08 N/m a linear approximation can be used between 10 and 100 °C for the temperature dependence of the surface tension of pure water according to Jasper (1972):

$$\sigma_{la}(T) = 116.19 \, \text{N/m} - T \cdot 0.1477 \, \text{N m}^{-1}\text{K}^{-1}. \tag{2.25}$$

This function is used for temperatures above 0 °C; below 0 °C surface tension is assumed to be constant.

2.4.1.2 Gas Phase Saturation

The sum of saturations is always equal to one. The gas phase saturation is therefore $S_g = 1 - S_l$ in unfrozen or $S_g = 1 - S_l - S_i$ in frozen porous media.

2.4.1.3 Freezing Curve

In frozen soils water does not freeze completely at the freezing point. Measurements show a more gradual decrease of the liquid water content and even at temperatures of -10 °C liquid water is still present. This phenomenon is explained in analogy to unsaturated unfrozen soils, by capillary and surface adsorption forces (Figure 2.5). As solutes are excluded from the ice phase, osmotic pressure has also to be considered. The surface tension σ_{wi} of the water/ice interface is found to be approximately half the surface tension σ_{wa} of the water/air interface. Spaans and Baker (1996) found that water characteristic and freezing curve could be related to each other. The pressure difference at the water ice interface can be calculated from the Clausius-Clapeyron equation.

$$v_l^w dp_l - v_i^w dp_i = \left(S_l^w - S_i^w\right) dT = \frac{\Delta H_{il}^w}{T} dT \tag{2.26}$$
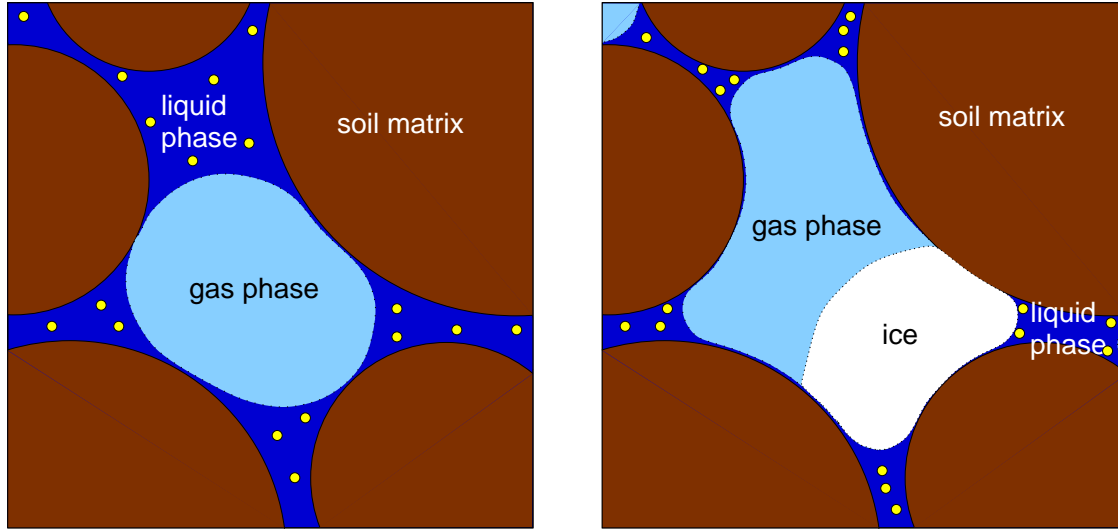
Figure 2.5: Schematic representation of the pore space before (left) and after (right) freezing. Complete exclusion of solutes (yellow) from the ice phase is assumed

with S_l^w, S_i^w: Entropy of liquid water, ice [J/K]
$v_l^w = (\nu_l^w)^{-1}$, $v_i^w = (\nu_i^w)^{-1}$: Molar volume of liquid water/ice [m³/mole]

If we assume that the molar volumes are not temperature and pressure dependent and the phase change enthalpy is not pressure dependent, this equation can be integrated and yields

$$(\nu_l^w)^{-1} (p_l - p_{\text{atm}}) - (\nu_i^w)^{-1} (p_i - p_{\text{atm}}) = \int_{T_0}^{T} \frac{\Delta H_{il}(T^*)}{T^*} dT^* \qquad (2.27)$$

$$\implies \quad p_l - p_i = \nu_l^w \cdot \int_{T_0}^{T} \frac{\Delta H_{il}(T^*)}{T^*} dT^* + \left(\frac{\nu_l^w}{\nu_i^w} - 1 \right) \cdot (p_i - p_{\text{atm}}) \qquad (2.28)$$

If we calculate the osmotic pressure Π_o using the assumption of complete exclusion of the solutes from the ice phase we can calculate the liquid phase pressure at a temperature T below the freezing point from:

$$p_l(T) = p_i + \Pi_o + \nu_l^w \cdot \int_{T_0}^{T} \frac{\Delta H_{il}(T^*)}{T^*} dT^* + \left(\frac{\nu_l^w}{\nu_i^w} - 1 \right) \cdot (p_i - p_{\text{atm}}). \qquad (2.29)$$

Miller (1980) got the same equation by a slightly different derivation.

Using $p_c = p_i - p_l(T)$ the unfrozen water content can then be calculated from the soil water characteristic. This derivation is only an approximation. Difficulties arise from the difference in surface tension at the water/air and water/ice interface. If capillary forces are not prevalent, like in dry soils or in very clayey soils this

difference is not relevant and the unfrozen water content can be derived directly using the formula above. If the soil is completely saturated so that only water/ice interfaces exist the pressure differences between liquid and ice phase should be scaled with the ratio of surface tensions. In the range between these extremes it depends on the geometry of the gas and ice phase. Two extreme cases can be imagined: Either the whole liquid phase is covered by ice and there are only water/ice and ice/air interfaces, or the ice is concentrated at a few points and water/air interfaces are prevalent (Figure 2.5). As this question has not been answered until today (Miller (1980) hints at a tendency of the ice to reduce the number of ice/air interfaces), the unfrozen water content is derived without any scaling due to differences in surface tension in this work.

2.4.2   Gas and Liquid Phase Conductivity

It is not easy to measure the gas and liquid phase conductivity of a porous medium. The saturated conductivities are usually measured directly, but boundary effects are hardly negligible and the results have a large standard deviation. The unsaturated conductivity can either be measured directly at distinct capillary pressures or it can be derived from multistep outflow measurements by inverse modeling. Unlike the soil water characteristic, the conductivities are only mildly hysteretic if expressed as function of saturation.

Conductivity can be separated in absolute permeability, relative permeability and dynamic viscosity:

$$\boldsymbol{K}_l = \boldsymbol{K} \cdot \frac{k_{r_l}(S_l)}{\mu_l} \tag{2.30}$$

$$\boldsymbol{K}_g = \boldsymbol{K} \cdot \frac{k_{r_g}(S_g)}{\mu_g} \tag{2.31}$$

The absolute permeability tensor is a material property of the porous medium, the dynamic viscosities μ_l and μ_g are specific for the fluid/gas, whereas the relative permeabilities k_{r_l} and k_{r_g} depend in a complex manner on the geometry of the solid phase and the arrangement of the phase boundaries.

Mualem (1976) derived a parameterization for the relative permeability using the assumption that the porous medium can be regarded as a bundle of interconnected capillaries and that the distribution of capillary radii is given by the soil water characteristic:

$$k_{r_l}(S_{e_l}) = S_{e_l}^\tau \int\limits_0^{S_{e_l}} \frac{dS}{p_c^2(S)} \bigg/ \int\limits_0^1 \frac{dS}{p_c^2(S)} \tag{2.32}$$

with τ called "tortuosity" factor. Mualem modified this function after comparison with the conductivity functions of 50 soils to:

$$k_{r_l}(S_{e_l}) = S_{e_l}^{\tau} \left[\int_0^{S_{e_l}} \frac{dS}{p_c(S)} \bigg/ \int_0^1 \frac{dS}{p_c(S)} \right]^2 \tag{2.33}$$

If the van Genuchten model (Equation 2.21) is inserted for the water characteristic, we get:

$$k_{r_l}(S_{e_l}) = S_{e_l}^{\tau} \left[1 - \left(1 - S_{e_l}^{1/m} \right)^m \right]^2 \tag{2.34}$$

$$k_{r_l}(p_c) = \frac{\left\{ 1 - (\alpha p_c)^{n-1} \left[1 + (\alpha p_c)^n \right]^{-m} \right\}^2}{\left[1 + (\alpha p_c)^n \right]^{m\tau}} \tag{2.35}$$

With the Brooks-Corey model (Equation 2.22) the Mualem model yields:

$$k_{r_l}(S_{e_l}) = S_{e_l}^{2+\tau+2/\lambda} \tag{2.36}$$

$$k_{r_l}(p_c) = \begin{cases} [p_c/p_e]^{-2-\lambda[\tau+2]} & p_c \geq p_e \\ 1 & p_c < p_e \end{cases} \tag{2.37}$$

The tortuosity factor τ was set to 0.5 by Mualem. Today it is often used as additional fitting parameter.

Dury et al. (1999) derive the gas phase permeability defining S_{e_g} analogue to S_{e_l} using the same derivation as for the liquid phase. They get

$$k_{r_g}(S_{e_g}) = S_{e_g}^{\tau} \left[1 - \left(1 - S_{e_g} \right)^{1/m} \right]^{2m} \tag{2.38}$$

for the van Genuchten and

$$k_{r_g}(S_{e_g}) = S_{e_g}^{\tau} \left[1 - \left(1 - S_{e_g} \right)^{(1+\lambda)/\lambda} \right]^2 \tag{2.39}$$

for the Brooks-Corey model. Additionally they demonstrated that it might be necessary to adjust the equations if the gas phase becomes discontinuous before full water saturation is reached. Heterogeneity in combination with the air entry pressure of the pores might be one reason for this observation. Other transport processes like diffusion of dissolved gases and the rising of air bubbles might get important. As some of these processes are included explicitly in this work the approach of Dury et al. (1999) is not used.

As the liquid phase distribution is determined by interactions of liquid and solid phase even in frozen porous media, the liquid phase conductivity is still calculated from liquid phase saturation. Additional friction at boundaries between liquid phase and ice is neglected. Gas permeability in a frozen soil is much harder to estimate,

as it depends much more on the ice distribution. For this work it is assumed that the coarsest pores are filled with air and gas phase conductivity can be calculated in the same way as in unfrozen soils. These assumptions will lead to an overestimation of both liquid and gas phase conductivities.

If huge amounts of water infiltrate into a frozen soil during snowmelt in spring, water can also infiltrate into the coarse pores filled with air and into macro pores generated by mechanical processes during freezing. The assumption that water is always in the finest pores, which is the basis of the Mualem model, is then no longer valid and infiltration could be much faster than expected. Stähli et al. (1999) suggested a model which includes this effect by introducing a high flow domain for water which's conductivity is given by:

$$k_{r_{l_{\mathrm{hf}}}} = e^{-S_i/fs_i} \cdot \left(k_{r_l}(S_l + S_i + S_{l_{\mathrm{hf}}}) - k_{r_l}(S_l + S_i) \right) \tag{2.40}$$

f_{S_i} is a fitting parameter describing the damping effect of ice and $S_{l_{\mathrm{hf}}}$ is the liquid phase saturation of the high flow domain. Water in the high flow domain refreezes with time. The water flux between high flow domain and the normal liquid phase is given by

$$j^w_{\mathrm{infreeze}} = \alpha_h \frac{T}{\Delta H^w_{il}}. \tag{2.41}$$

As this model introduces two new fitting coefficients f_{S_i} and the heat exchange parameter α_h, which can not be measured independently, and as the aim of this work is to study the physical interactions in porous media based on a deterministic process model, this approach is not used.

2.4.3 Diffusion Coefficients

Depending on gas phase density two different descriptions have to be used for gas diffusion in porous media: Knudsen diffusion and molecular diffusion.

Knudsen diffusion is not important in natural porous media. It occurs only if gases diffuse in very small pores[8] or at very low pressures. The mean free path length is then much larger than the pore radius and the probability for a molecule to hit the pore wall is much higher than the probability to hit another molecule.

If the mean free path length is much smaller than the pore diameter, molecules collide with each other more often than with the pore walls. Molecular diffusion therefore depends mainly on the composition of the gas or liquid phase. The presence of the porous medium nevertheless influences the diffusion processes.

In free space, molecular diffusion of two gases can be described by Fick's law:

$$j^i_{g_D} = -D^{ij}_g \nabla \nu^i_g \tag{2.42}$$

---

[8]at normal temperature and pressure Knudsen diffusion occurs at a pore radius smaller than 50 nm (Schulz 1995).

with $\quad j_{g_D}^i$: Molar flux of component i due to molecular diffusion [mole m^{-2} s^{-2}]

$\quad\quad D_g^{ij}$: Binary diffusion coefficient of components i and j [m^2/s]

$\quad\quad \nu_g^i$: Molar density of component i in the gas phase [mole/m^3].

Fick's law is no longer applicable if there are more than two components or in the presence of walls. It can be shown still to be valid for a trace gas or solute with a very small concentration. However it has been frequently applied for the calculation of gas diffusion (Findikakis and Leckie 1979, Lindgren and Rasmuson 1994, Baehr and Baker 1995, Freijer and Leffelaar 1996) and solute transport in soils. The porous medium is taken into account by multiplication of the binary diffusion coefficients with a saturation dependent relative diffusion coefficient $\xi(S)$.

A better founded theory for the transport of a gas mixture in a porous medium is given by the dusty gas model. In this model soil particles are treated as very big gas molecules, which are stationary in the frame of reference (Thorstenson and Pollock 1989a, Thorstenson and Pollock 1989b, Cunningham and Williams 1980, Mason et al. 1967). From this assumption an equation system can be derived which describes molecular diffusion, Knudsen diffusion and viscous flow as well as nonequimolar flux. Nonequimolar flux results from the different speed of gas molecules with different mass at the same temperature. Molecular diffusion then results in a pressure gradient, generating a quasi-viscous counter flux. As this equation system can not be solved explicitly for the flux of individual gases, it is difficult to incorporate in a coupled model and would increase computing time significantly. In this work gas and solute transport therefore are calculated with the modified Fick's law despite the legitimate problems. It is necessary to check at a later time if the dusty gas model yields better results. The effect of nonequimolar flux can be approximated if diffusion coefficients are adapted for molecules with different mass, which leads to a pressure gradient and a net flux.

There are a lot of formulas for the estimation of the saturation dependent relative diffusion coefficient. In a study made by Jin and Jury (1996)

$$\xi(S) = \frac{S^2\Phi^2}{\Phi^{2/3}} \tag{2.43}$$

gave the best correspondence with measured gas diffusion coefficients. A diploma thesis by Ott (1996) confirmed the applicability of this formula. It is used in this work for both gas and solute transport.

2.4.4 Water/Solute Interaction

It is often suggested to include an osmotic potential $\psi_o = -\Pi_o$ into the hydraulic potential driving the water transport. An osmotic pressure Π_o exists between a
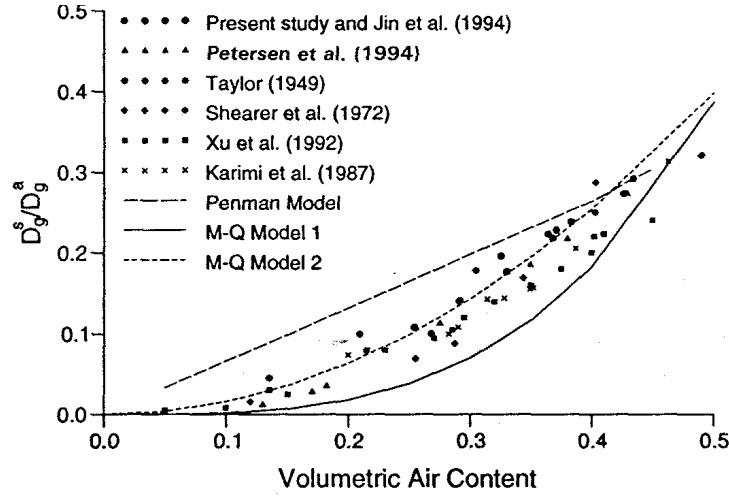
Figure 2.6: Comparison of measured relative diffusion coefficients with different tortuosity models. Penman Model: $\xi_g(S_g\Phi) = 0.66 S_g\Phi$, M-Q Model 1: $\xi_g(S_g\Phi) = (S_g\Phi)^{10/3}/\Phi^2$, M-Q Model 2: $\xi_g(S_g\Phi) = (S_g\Phi)^2/\Phi^{2/3}$ (from Jin and Jury 1996)

solution and pure water separated by a membrane which is permeable to water molecules but not to the solutes. It can be calculated as

$$\Pi_o = -\nu_l^w RT \log(X_l^w) \approx RT \sum_i c_{l_i}^s, \tag{2.44}$$

where X_l^w is the molar fraction of water in the liquid phase and R the ideal gas constant. The summation index i runs over all solute species.

If the density of water is approximately constant, the gradient of osmotic potential is

$$\psi_o = -\nu_l^w RT \nabla \log(X_l^w) = -\nu_l^w RT \frac{1}{X_l^w} \nabla X_l^w \approx -\frac{RT}{X_l^w} \nabla c_l^w, \tag{2.45}$$

which is obviously a diffusion term. In analogy to the discussion of nonequimolar flux in the previous section, the interaction between solute transport and water transport seems to be important if the concentration of solutes is high and the mass of the solutes is different from the mass of water molecules. If a semipermeable membrane exists, e.g. in root water uptake, water vapor transport or soil freezing, the osmotic pressure (Equation 2.44) must be taken into account.

2.4.5 Fluid/Gas Properties

2.4.5.1 Gas Solubility

As gas solubility is low in water, each gas molecule can be assumed to be completely surrounded by water molecules at usual temperatures and pressures. The tendencies

of gas molecules to leave the solution is then proportional to their molar fraction and the solubility is described by Henry's law: (Moore 1990)

$$p_g^i = k_H^i X_l^i \tag{2.46}$$

with p_g^i: partial pressure of gas i [Pa]
k_H^i: Henry coefficient of gas i [Pa]
X_l^i: molar fraction of gas i in the liquid phase [–]

The temperature dependent Henry coefficients for oxygen and nitrogen are given in Weast (1995):

$$k_H^{O_2} = e^{-66.735+8747.5\text{K}/T+24.453*\log(T/100\text{K})} \text{ Pa} \tag{2.47}$$

$$k_H^{N_2} = e^{-67.388+8632.1\text{K}/T+24.798*\log(T/100\text{K})} \text{ Pa} \tag{2.48}$$

The Henry coefficient for air is calculated by $0.21 \cdot k_H^{O_2} + 0.79 \cdot k_H^{N_2}$.

2.4.5.2 Viscosity of Liquid and Gas Phase

Atkins (1990) gives the temperature dependency of the dynamic viscosity of water μ_l as:

$$\begin{aligned} \mu_w &= \mu_{w_{20}} \cdot 10^{-A} \\ A &= \frac{1.37023 \cdot (T - 293.15\text{K}) + 8.36 \cdot 10^{-4}\text{K}^{-1} \cdot (T - 293.15\text{K})^2}{-164.15\text{K} + T} \\ \mu_{w_{20}} &= 1.0019 \cdot 10^{-3}\,\text{Pa s}, \quad [T \text{ in K}] \end{aligned} \tag{2.49}$$

A constant liquid phase viscosity is used for temperatures below 0 °C. Changes of viscosity with composition are neglected.

The viscosity of air at 273 K and 293 K is given by Atkins, the gas phase viscosity is therefore linearly interpolated from:

$$\mu_g = 1.73 \cdot 10^{-5}\text{Pa s} + 4.5 \cdot 10^{-8}\,\text{Pa s/K} \cdot (T - 273\text{K}) \tag{2.50}$$

2.4.5.3 Densities

A polynomial of fourth degree can be fitted to the values given by Kuchling (1991) for the density of water for temperatures above 0 °C:

$$\begin{aligned} \rho_l^w &= -3.6247 \cdot 10^{-7}\,\text{kg/K}^4 \cdot T^4 + 4.6537 \cdot 10^{-4}\,\text{kg/K}^3 \cdot T^3 \\ &\quad -0.22767\,\text{kg/K}^2 \cdot T^2 + 49.823\,\text{kg/K} \cdot T - 3089.3\,\text{kg} \end{aligned} \tag{2.51}$$

For temperatures below 0 °C, the equation

$$\begin{aligned} \rho_l^w &= 999.8kg + 1.584 \cdot 10^{-2}\,\text{kg/K} \cdot \vartheta - 1.475 \cdot 10^{-2}\,\text{kg/K}^2 \cdot \vartheta^2 \tag{2.52} \\ \vartheta &= T - 273.15\,\text{K} \tag{2.53} \end{aligned}$$

is given by Hare and Sorensen (1987). Molar density of water is calculated using a molar mass of 0.018015 kg/mole.

The density of ice is assumed to be constant $\nu_i^w = 917$ kg/m^3, the density of air is calculated from the ideal gas law using $M_a = 0.026$ kg/mole.

2.4.6   Heat Conductivity

The heat conductivity of a porous medium depends not only on its composition, but also on the geometry of the pore space and the distribution of the phases. The problem is simplified by the strong dissipative nature of heat transport. Kersten (1949) derived an empirical conductivity function for frozen and unfrozen soils that was used, for example, in the SOIL model by Jansson (1998).

De Vries (1952) developed a method to estimate the composition dependence of heat conductivity[9]. In analogy to the description of polarization, heat conductivity can be estimated with the formula

$$\lambda = \frac{\sum_{i=0}^{N} k^i X^i \lambda^i}{\sum_{i=0}^{N} k^i X^i} \qquad (2.54)$$

with k^i: Ratio of the average temperature gradient in particles of type i
                to the average temperature gradient in the surrounding medium [–]
        X^i: volume fraction of component i [–]
        λ^i: heat conductivity of component i [Wm^{-1}K^{-1}]

The value of k^i depends on the ratio λ^i/λ_0,[10] and the size, form and position of the particles. If they are assumed to be ellipsoids with a distance large enough to be treated independently, k^i can be calculated:

$$k^i = \frac{1}{3} \sum_{a,b,c} \left[1 + \left(\frac{\lambda^i}{\lambda_0} - 1 \right) g_a \right]^{-1} \qquad (2.55)$$

g_a, g_b, g_c are dimensionless form factors, depending on the ratio of the axes a, b and c of the ellipsoid. Their sum is equal to one. If two axes are equal, their form factors are equal as well. For spherical particles $g_a = g_b = g_c = 1/3$. Both assumptions are clearly not valid for a natural porous medium, but according to de Vries theoretical reasons as well as measurements hint at an applicability of equation 2.55. My own research (Ippisch et al. 1998) showed a good agreement of this approximation with results obtained from simulations explicitly considering the structure of a soil sample.

---

[9]The heat conductivity is also temperature dependent. This dependence is not considered.
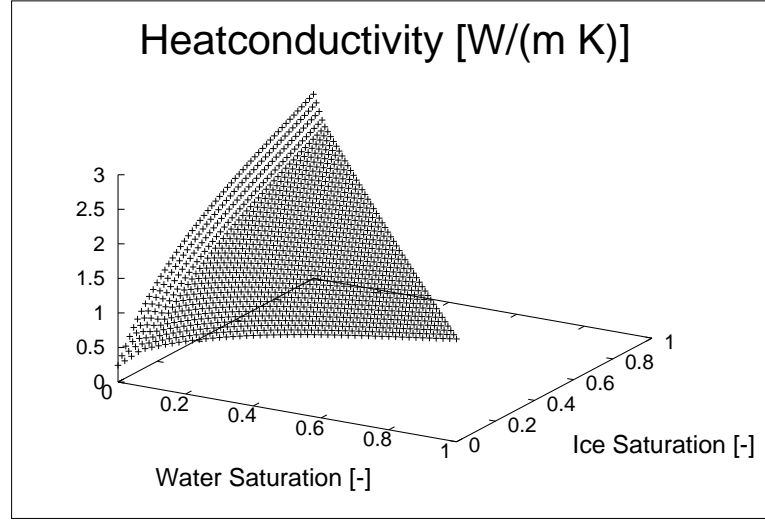[10]λ_0 is the heat capacity of the surrounding medium.

Figure 2.7: Example for the dependence of the heat conductivity of a porous medium on ice and water saturation calculated with the generalized de Vries model

The heat conductivity can only be calculated with equations 2.54 and 2.55 for fully saturated frozen or unfrozen porous media or completely dry soils. For water contents in between, the form factors g_a, g_b, g_c for air bubbles (or ice crystals) are necessary. De Vries (1963) gives in example 7.6.1 a method to estimate them. Additionally, the increase in heat conductivity of the gas phase due to water vapor transport must be considered (chapter 2.4.6.1). The de Vries model is widely used in models for frozen and unfrozen soils (Blom and Troelstra 1972, Huwe 1992, Flerchinger and Saxton 1989).

To calculate the heat conductivity of frozen soils the de Vries model was applied for unfrozen soils (only air and water), completely frozen soils (only air and ice) and completely saturated soils with an increasing ice content (only water and ice). For water contents in between, the heat conductivity was interpolated in a way which takes care of the change of phase continuities. An example for the resulting heat conductivity distribution can be seen in figure 2.7.

2.4.6.1 Water Vapor Transport

Philip and de Vries (1957) and de Vries (1958) wrote two fundamental papers on the peculiarities of water vapor transport. If local thermodynamic equilibrium is assumed, no separate equation for water vapor transport is necessary. According to Philip and de Vries (1957) the molar density of water vapor is given by

$$\nu_g^w(p_c, T) = \nu_{g_0}^w(T)\mathrm{rH} = \nu_{g_0}^w(T)\exp\left(\frac{-p_c\,M_w\,g}{R\,T}\right) \tag{2.56}$$

with $\nu_{g_0}^w$:   molar density of saturated water vapor [mole/m^3]

        rH: humidity [–]

        M_w: molar mass of water [kg/mole]

The molar density of water vapor above pure water at saturation is given by Weischet (1991):

$$\nu_{g_0}^{w\bullet}(T) = \frac{610.78\,Pa}{R\,T}\exp\left(\frac{17.08085\,(T - 273.15K)}{T - 38.975K}\right) \tag{2.57}$$

Vapor pressure above a solution is lower than above pure water, as a part of the interface between gas and liquid phase is covered by solute molecules, which reduces the tendency of water molecules to leave the liquid phase. For an ideal solution this effect can be calculated by Raoult's law (Moore 1990)

$$\nu_{g_0}^w(T) = X_l^w \nu_{g_0}^{w\bullet}(T). \tag{2.58}$$

X_l^w is the molar fraction of water in the solution.

The molar density gradient in Fick's law can be separated using equation 2.56

$$\nabla\nu_g^w = \mathrm{rH}\nabla\nu_{g_0}^w + \nu_{g_0}^w\nabla\mathrm{rH} \tag{2.59}$$

At constant capillary pressure the temperature dependency of humidity is small enough to set $\partial\mathrm{rH}/\partial T = 0$.

$$\Rightarrow \nabla\nu_g^w = \mathrm{rH}\frac{d\nu_{g_0}^w}{dT}\nabla T + \nu_{g_0}^w\frac{d\mathrm{rH}}{dp_c}\nabla p_c = \mathrm{rH}\frac{d\nu_{g_0}^w}{dT}\nabla T - \frac{\nu_g^w g}{RT}\nabla p_c \tag{2.60}$$

The flux law for water vapor diffusion is then

$$\vec{J}_{gD}^w = -D_{gT}^w\nabla T - D_{gp_c}^w\nabla p_c \tag{2.61}$$

For the derivation of D_{gT}^w it is useful to look at a single pore in a relatively dry porous medium (Figure 2.8). If there are neither temperature nor potential gradients, the curvature at A and B is equal.

Transport of gases across the liquid island is very limited, as solubility in water is small and the diffusion coefficients in solution are some orders of magnitude smaller than the diffusion coefficients in air.

If there is a vapor density gradient in the direction indicated by the arrow, water vapor condenses at side A, which decreases curvature whereas the curvature at B is increased by evaporation. In equilibrium water flux between A and B equals the water vapor flux in the gas phase. According to Philip and de Vries (1957) the equilibrium is reached quickly. This increases the cross section available for vapor flux markedly.
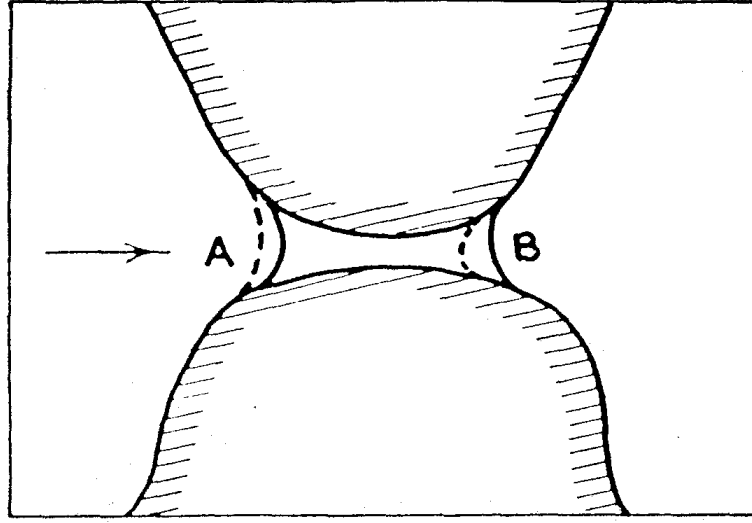
Figure 2.8: Water vapor transport through a liquid island. The arrow gives the direction of transport (from Philip and de Vries 1957)

A precise analysis of the small scale temperature and water vapor distribution would be quite complicated. The authors therefore further analyzed water vapor flux in a single pore. The flux density is:

$$- D_{g_{\mathrm{atm}}}^{w} \mathrm{rH} \frac{d\nu_{g_0}^{w}}{dT} (\nabla T)_g \tag{2.62}$$

$(\nabla T)_g$ is the average temperature gradient in the pore, $D_{g_{atm}}^{w}$ the diffusion coefficient for water vapor in free atmosphere. This equation is based on the assumption of similarity between the temperature field and the molar density distribution of water vapor in a pore. It is also valid for the average flux density in all air filled pores, if $(\nabla T)_g$ is interpreted as the average temperature gradient in these pores. If it is further assumed that the flux density in the liquid islands is equal to the average flux density in air filled pores, we get:

$$- (S_g + S_l)\Phi D_{g_{\mathrm{atm}}}^{w} \mathrm{rH} \frac{d\nu_{g_0}^{w}}{dT} (\nabla T)_g = -D_{g_T}^{w} \nabla T \tag{2.63}$$

Tortuosity is already included in $(\nabla T)_g$.

As a result of the different heat conductivities of the phases in a natural porous medium, the average temperature gradient is not the same for all phases. If a temperature gradient is applied to a one-dimensional system consisting of a layer of quartz, a water film on the surface of the quartz layer, an air gap and another water covered quartz block, the temperature gradients will be quite different (Figure 2.9). As a natural porous medium has a complicated three-dimensional structure, we get
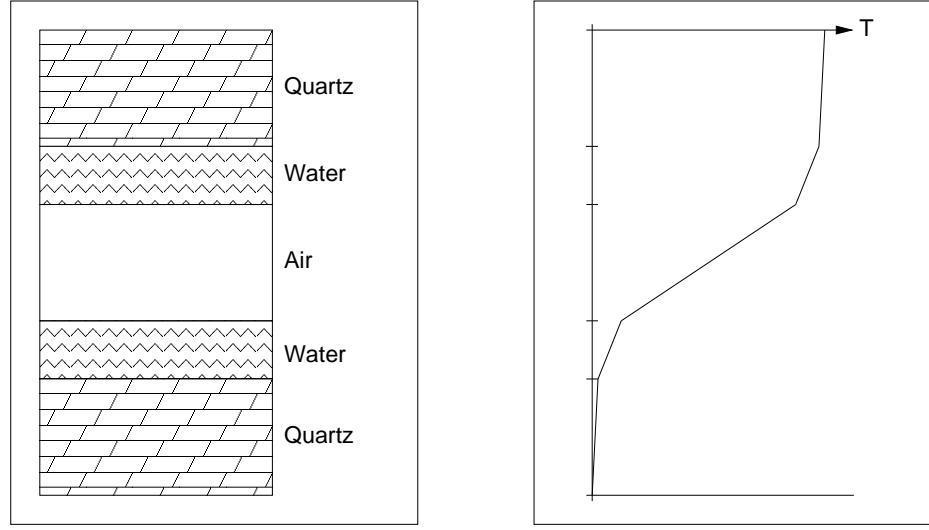
Figure 2.9: Temperature distribution (right) in a simple heterogeneous medium (left) if a vertical temperature gradient is applied

a complicated temperature distribution, resulting in different average temperature gradients.

At high water contents the water flux caused by water vapor transport will be reduced, as the capillary radii can not adjust fast enough and the liquid islands become scarce and more elongated. The saturation S_{l_k} at which the liquid phase conductivity is nearly zero, because of phase discontinuity, can be taken as limit for the process. In equation 2.63 $(S_g + S_l)$ is therefore replaced by a factor $(S_g + f(S_g) S_l)$:

$$D_{g_T}^w = (S_g + f(S_g) S_l) \Phi D_{g_{atm}}^w \mathrm{rH} \frac{d\nu_{g_0}^w}{dT} \frac{(\nabla T)_g}{\nabla T} \tag{2.64}$$

Philip and de Vries (1957) suggest a value of $f(S_g) = 1$ for $S_g \geq (1 - S_{l_k})$ and $f(S_g) = S_g/(1 - S_{l_k})$ for $S_g < (1 - S_{l_k})$.

The ratio between the average temperature gradient in the air filled pores and the average temperature gradient across the whole porous medium, can be estimated with de Vries' method for the estimation of heat conductivity given in the previous section (chapter 2.4.6).

Philip and de Vries (1957) argue that water flux across liquid islands is not relevant for isothermal water flux, as very small changes in the radius of curvature would be sufficient to reverse the direction of water flux. The diffusion coefficient is then given by:

$$D_{g_{P_c}}^w = \frac{D_{g_{atm}}^w \xi_g \nu_l^w g M_w}{RT} \tag{2.65}$$

where ξ_g is a tortuosity coefficient calculated as given in chapter 2.4.3.

In equation 2.14 heat conduction and transport of latent heat with water vapor are additive processes on the macro scale. As water vapor transport can increase the effective heat conductivity of the gas phase, this is only a first approximation. De Vries (1958) suggests therefore two alternative formulations of the heat conductivity λ of a porous medium.

$$\lambda_1 = \lambda_* \tag{2.66}$$
$$\lambda_2 = \lambda_{\text{eff}} - D_{g_T}^w \tag{2.67}$$

λ_* is the (hypothetical) heat conductivity of a porous medium without any water vapor transport. It can be calculated with the method given in section 2.4.6, if the heat conductivity of air filled pores is set to the heat conductivity of dry air. λ_{eff} is the effective heat conductivity, resulting from the interaction of water vapor transport and heat conduction. One approximation is the addition of $D_{g_T}^w$ to the heat conductivity of air in the de Vries model for heat conduction. The difference between λ_1 and λ_2 is small but not negligible according to de Vries. Depending on direction and size of isothermal diffusive and convective water vapor transport, the first or the second approximation is more correct.

As it is hard to separate the two cases and λ_{eff} depends strongly on temperature, λ_1 will be used in the current work.

2.4.7 Mechanical Interactions

In most existing models of transport in porous media, soils are assumed to be rigid bodies, with properties not changing with time. If this assumption was used for freezing soils, the equation system was not solvable. A strong redistribution of water occurs during freezing resulting in frost heave (Miller 1980). Two different types of frost heave occur: In coarse textured material, the water freezes just on the spot. As the density of ice is lower than the density of water, this leads to a volume increase. In fine textured media, water moves to the freezing front for some time, as the hydraulic conductivity remains high even for low unfrozen water contents. Ice lenses form, while the dessicated material is compressed.

A full mechanical model of a freezing porous media is out of the scope of this work. A simplified model is needed, to deal with the numerical difficulties.

At continuum scale deformation of a porous medium can be described by a visco-plastic model (Miller 1980). The envelope pressure σ (caused for example by the weight of the overburden), is balanced by two forces: the effective stress σ_e, caused by the resistance of intergranular contacts to compression, and the neutral stress σ_n resulting from the reaction of the phases in the pore space. If there is more than one phase in the pore space, the neutral stress can be calculated from the phase pressures and partition factors.

$$\sigma_n = \chi_l p_l + \chi_g p_g + \chi_i p_i \tag{2.68}$$

The partition factors χ_j add up to one and are equal to one for a phase if the soil is completely saturated with this phase or zero if the phase is completely absent. An ice lens can form if σ_e becomes zero or negative. This is the case if $\sigma \leq \chi_l p_l + \chi_g p_g + \chi_i p_i$.

It is assumed that ice pressure and gas phase pressure are equal. Equation 2.68 can then be rewritten as $\sigma_n = \chi_l \psi_l + (\chi_g + \chi_i) p_g$ or $\sigma_n = \chi_l \psi_l + (\chi_g + \chi_i) p_i$. As saturations are used as partition factors χ_l is equal to S_l and $\chi_g + \chi_i = (1 - S_l)$.

It is assumed that the porous medium reacts fully elastic. The porous medium expands proportional to the absolute value of effective stress, if effective stress is negative. Expansion is only allowed if ice is present. It is assumed that the volume expansion is only a consequence of ice accumulation.

This approach can be used in two ways: If Richards' equation is used for the liquid phase transport or in absence of a gas phase, the ice pressure can be calculated from the pore volume. If multiphase equations are used, the pore volume can be calculated from gas pressure.

3 Numerical Solution

3.1 Mathematical Formulation of the Equation System

Mathematically the model formulated in the previous chapter consists of a set of up to four partial differential equations (the balance equations 2.2-2.5 combined with the storage terms 2.6-2.9 and flux laws 2.10-2.14) and a set of algebraic relations (the effective parameters defined in section 2.4). To solve the equation system, a set of independent variables has to be chosen. The selection of temperature T for the energy balance equation and concentration c_l^s for the solute balance equation are quite natural. For the water and gas balance equation variables can be substituted by others using the algebraic relations, which makes more than one choice possible. Depending on the selection, different mathematical models can be derived, which have a strong impact on the numerical simulation. There are a lot of possibilities, including the creation of new artificial variables with favorable numerical properties. Bastian (1999) gives an overview of some commonly used formulations. In this work only the frequently used phase pressure/saturation formulation and a new partial pressure/phase pressure formulation will be discussed.

3.1.1 Phase Pressure/Saturation Formulation

In the phase pressure/saturation formulation either liquid phase pressure p_l and gas saturation S_g, or gas phase pressure p_g and liquid saturation S_l are chosen as the independent variables. Pressure and saturation of the other phase can be eliminated using the physical constraints (e.g. saturations add up to one $\Rightarrow S_l = 1 - S_g$). Depending on the choice of the phase for which pressure is calculated, the phase pressure/saturation formulation remains solvable either for complete water saturation ($S_g = 0$ is still defined) or complete gas saturation (with $S_l = 0$). As the capillary pressure p_c has to be calculated from inversion of the soil water characteristic, the Brooks-Corey parameterization can not be used in the phase pressure/saturation formulation without regularization. Another problem arises if the pressure/saturation formulation is used in strongly heterogeneous media, as the phase pressure is continuous across material discontinuities, whereas saturation is not.

3.1.2 Partial Pressure/Phase Pressure Formulation

The problem of a pressure/pressure formulation is the specification of the pressure of an absent phase, when the porous medium is saturated with the other phase. In natural porous media this is typically the gas phase pressure, as there are always some liquid water films on the solid surface, which can be related to a capillary pressure. This problem can be resolved, if dissolution of gases[1] in water is taken into account using Henry's law (section 2.4.5.1). The partial pressure of air p_g^a can be chosen as independent variable. The concentration of dissolved air is then given by $c_l^a = p_g^a/k_H^a \cdot \nu_l^w$ and the gas phase pressure is either equal to the partial pressure of air $p_g = p_g^a$, if water vapor transport is neglected or the sum of the partial pressures of air and water vapor[2] $p_g = p_g^a + p_g^w$. The partial pressure of air thus remains defined even in complete absence of an air phase (if there's not even dissolved air, it is just zero). As capillary pressure is defined as the difference between gas and liquid phase pressure, it is always well defined and liquid phase saturation can be calculated from the soil water characteristic. A gas phase emerges, if the capillary pressure is higher than the air entry pressure in the Brooks-Corey model or above zero if the van Genuchten model is used. Transition to Richards' equation is easy, as all effective parameters can be calculated in the same way for both Richards' equation and partial pressure/phase pressure formulation. To get Richards' equation, gas phase pressure must be set to atmospheric pressure and the balance equation for air and the calculation of gas phase fluxes have to be skipped. As there is an abrupt change in gas phase saturation at the entry pressure, when the Brooks-Corey model is used, numerical difficulties might arise. The partial pressure/phase pressure formulation should also be advantageous in heterogeneous media, as both pressures are continuous across material discontinuities.

The partial pressure/phase pressure formulation is used in this work, as it allows the use of the Brooks-Corey parameterization. It also makes the investigation of differences between water transport calculated with Richard's equation and with twophase equations easier.

---

[1]In the black oil model (Peaceman 1977) air solubility is also considered, as it is an important process at high pressures, but not with the objective to deal with numerical problems at saturation.

[2]The water vapor pressure can then no longer be expressed explicitly, as it depends on capillary pressure, but has to be calculated from the nonlinear equation
$\nu_g^w = \nu_{g_0}^w(T) \exp\left(\frac{-(p_g^a + \nu_g^w RT - p_l) M_w g}{RT}\right)$

3.2 Discretization

3.2.1 Spatial Discretization

There are numerous spatial discretization schemes. Besides various finite difference, finite element and finite volume methods there are methods of characteristics (MMOC, ELLAM...). They differ in their numerical properties (global or local mass conservation, resolution of steep fronts, monotonicity of the solution...) and their precision at large time steps. Helmig (1997) and Bastian (1999) give comparisons of various methods.

In this work a fully implicit, fully coupled, vertex centered finite volume scheme will be used. The advantages of this discretization are stability, consistency, robustness, local mass conservation, monotonicity of the solution and the ability to handle unstructured meshes, which makes it possible to deal with complex geometries. The model was realized using the numerical toolbox UG (Bastian et al. 1997), which provides routines for the management of unstructured grids, the solution of linear and nonlinear equation systems, time-stepping schemes, parallelization and visualization.

As an example, the discretization of Richards' equation will be demonstrated. If the discretization is done properly, calculations are possible in 2D as well as in 3D. Combination of equations 2.2, 2.6 and 2.10 yields:

$$\frac{\partial \left(\Phi \cdot S_l \cdot c_l^w \right)}{\partial t} - \nabla \cdot \left[\nu_l^w \boldsymbol{K}_l(S_l) \left(\nabla p_l - \rho_l g \right) \right] = q^w. \tag{3.1}$$

The equation is solved for liquid phase pressure p_l.

To discretize equation 3.1, the domain of interest Ω with boundary Γ is divided into k elements $e_1, \ldots, e_k$. With UG, triangular and quadrilateral elements can be used in 2D, tetrahedrals, pyramids, prisms and hexahedra can be used in 3D. Support for cylindrical coordinates using rectangular elements parallel to the coordinate axes was added by the author. Different element types can be mixed, as long as there are no gaps between elements and two elements share either a corner node (called vertex), an edge (the connection of two vertices, the side of an element in 2D) or a face (the side of an element in 3D). The N vertices $v_1, \ldots, v_N$ are located at positions $\mathbf{x}_1, \ldots, \mathbf{x}_N$. For the vertex centered finite volume method a control volume b_i is defined for every vertex v_i, which is constructed by connecting the barycenters of all elements containing v_i to edge midpoints (2D) or face barycenters (3D). In 3D face barycenters are also connected to edge midpoints (Figures 3.1 and 3.2). Interior vertices are approximately in the center of their associated control volume, while boundary vertices are at its boundary. Nodal basis functions ϕ_i are defined on each element e_i, with the usual property $\phi_i(\mathbf{x}_j) = \delta_{ij}$ so that the value of p_l at position $\mathbf{x}$ is $p_l(\mathbf{x}) = \sum_i p_{l_i} \phi(\mathbf{x})$ where p_{l_i} is the solution at vertex i.
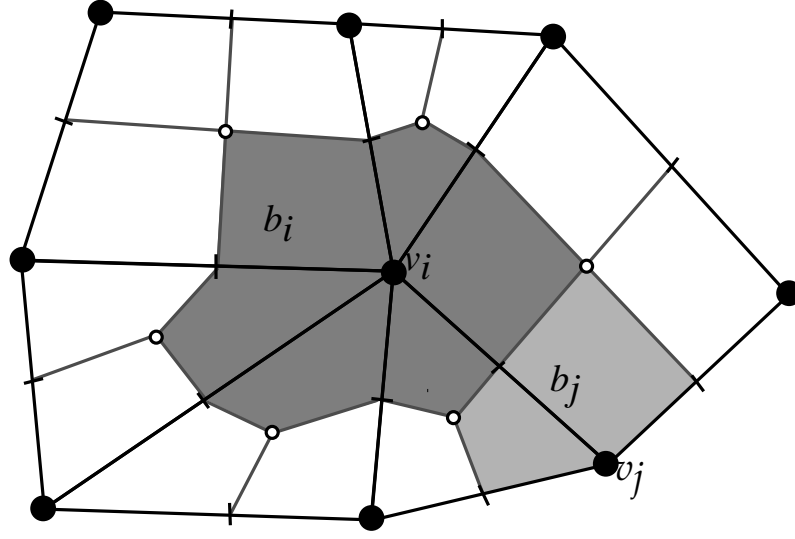
Figure 3.1: An element mesh with two vertices v_i and v_j and their control volumes b_i and b_j marked (from Bastian 1999)

Integration of equation 3.1 and application of Gauss' theorem yields:

$$\frac{\partial M(\mathbf{x})}{\partial t} - A(\mathbf{x}) = Q(\mathbf{x}) \tag{3.2}$$

$$M(\mathbf{x}) = \int_{\Omega} \left(\Phi \cdot S_l \cdot \nu_l^w \right) d\mathbf{x} \tag{3.3}$$

$$A(\mathbf{x}) = \int_{\Gamma} \left[\nu_l^w \boldsymbol{K}_l(S_l) \left(\nabla p_l - \rho_l g \right) \right] \cdot d\mathbf{n} \tag{3.4}$$

$$Q(\mathbf{x}) = \int_{\Omega} q^w d\mathbf{x} \tag{3.5}$$

M is the storage term, A is the flux term and Q the source term of the equation. In a weak formulation we demand only that equation 3.2 is valid for each control volume i (∂b_i is the boundary of the control volume).

$$\frac{\partial M_i(\mathbf{x})}{\partial t} - A_i(\mathbf{x}) = Q_i(\mathbf{x}) \tag{3.6}$$

$$M_i(\mathbf{x}) = \int_{b_i} \left(\Phi \cdot S_l \cdot \nu_l^w \right) d\mathbf{x} \tag{3.7}$$

$$A_i(\mathbf{x}) = \int_{\partial b_i} \left[\nu_l^w \boldsymbol{K}_l(S_l) \left(\nabla p_l - \rho_l g \right) \right] \cdot d\mathbf{n} \tag{3.8}$$

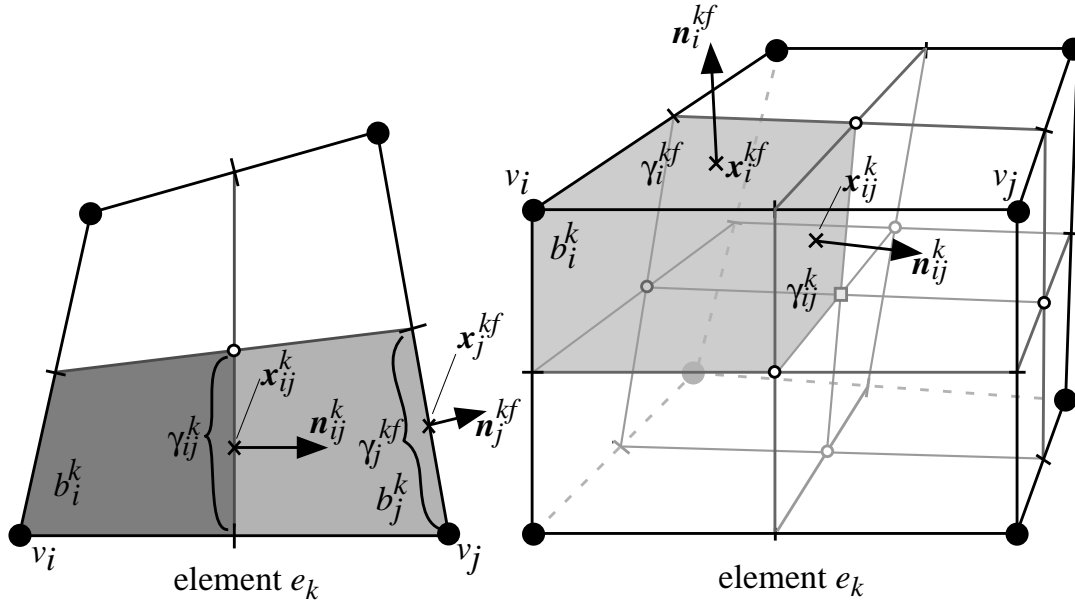$$Q_i(\mathbf{x}) = \int_{b_i} q^w d\mathbf{x} \tag{3.9}$$

Figure 3.2: 2D and 3D elements with their sub-control volumes and sub-control volume faces (from Bastian 1999)

Due to the nodal basis function, only the elements containing the vertex v_i are involved in the calculation of the integrals. As parameters like permeability can be different for each element, it is reasonable to split the integrals into a sum of integrals over sub-control volumes. A sub-control volume b_i^k is the intersection of a control volume and an element. Each sub-control volume has at least two sub-control volume faces γ_{ij}^k, which are the boundaries of b_i on element k and can be associated with the edge (v_i, v_j).

$$M_i(\mathbf{x}) = \sum_k \int_{b_i^k} (\Phi \cdot S_l \cdot \nu_l^w) \, d\mathbf{x} \tag{3.10}$$

$$A_i(\mathbf{x}) = \sum_k \sum_j \int_{\gamma_{ij}^k} \left[\nu_l^w \mathbf{K}_l(S_l) \left(\nabla p_l - \rho_l g \right) + D_g^w \nabla \nu_g^w \right] \cdot d\mathbf{n} \tag{3.11}$$

$$Q_i(\mathbf{x}) = \sum_k \int_{b_i^k} q^w d\mathbf{x} \tag{3.12}$$

The integrals are evaluated using the mid point rule, where the mid point of the control volume b_i (i.e. the position of the vertex v_i) is used for the volume integration and the barycenter $\mathbf{x}_{ij}^k$ of the sub-control volume face γ_{ij}^k is used for the surface integrals. If the outward directed normalized vector normal to γ_{ij}^k is called $\mathbf{n}_{ij}^k$, the

volume of the sub-control volume is designated V_i^k and the area of the sub-control volume face is termed F_{ij}^k, we get:

$$M_i(\mathbf{x}) = \sum_k \Phi^k \cdot S_l^k(p_{l_i}) \cdot \nu_l^w(\mathbf{x}_i) \cdot V_i^k \tag{3.13}$$

$$A_i(\mathbf{x}) = \sum_k \sum_j \left[\nu_l^w(\mathbf{x}_{ij}^k) \boldsymbol{K}_l^k(\mathbf{x}_{ij}^k) \left(\nabla p_l(\mathbf{x}_{ij}^k) - \rho_l(\mathbf{x}_{ij}^k) g \right) \right] \cdot F_{ij}^k \tag{3.14}$$

$$Q_i(\mathbf{x}) = \sum_k \left[q^w \right]^k (\mathbf{x}_i) \cdot V_i^k \tag{3.15}$$

Weakly nonlinear functions (e.g. ν_l^w) are interpolated from the values at the vertices using the nodal basis functions. Highly nonlinear functions (e.g. S_l^k) are calculated from the values of the interpolated primary variables at the barycenters of the sub-control volume faces. Gradients are evaluated using the nodal basis functions. Upwinding is done for the relative hydraulic conductivity using

$$[k_{r_l}]_{ij}^k = \begin{cases} [k_{r_l}]_i & J_l(\mathbf{x}_{ij}^k) \cdot \mathbf{n}_{ij}^k \geq 0 \\ [k_{r_l}]_j & \text{else} \end{cases} \tag{3.16}$$

Upwind stabilization leads to monotone solutions but also to numerical smoothing of sharp fronts and a higher sensitivity to grid orientation, as it is only first order accurate. Centered differences are second order accurate but yield oscillatory numerical approximations if the solution is not smooth enough.

3.2.1.1 Heterogeneity

As it must be possible to evaluate the effective parameter functions at the sub-control volume faces, only one set of effective parameter functions is allowed for every element. Different elements may have different sets of effective parameters. In the model this is done by giving each element a property called material, which is linked to a set of parameter functions. The function which determines the material is evaluated at the barycenter of the element.

3.2.1.2 Boundary Conditions

The sides of a sub-control volume at the boundary of the domain are called boundary faces. The type of the boundary condition for a boundary face is evaluated at the barycenter of the boundary face.

Dirichlet boundary conditions can be given for any vertex of the grid. The trivial equation $p_{l_i} = p_{l_{D_i}}$ is solved for a Dirichlet node instead of equation 3.6, where $p_{l_{D_i}}$ is the Dirichlet value set for the vertex υ_i. If the flux over the boundary is to be computed for a Dirichlet node, the flux across the sub-control volume faces between a Dirichlet boundary node and non-Dirichlet nodes must be calculated. If a Dirichlet

boundary condition is given for one boundary face of a sub-control volume, it is used for all boundary faces of the sub-control volumes belonging to the vertex.

If no Dirichlet boundary condition is given for a vertex, Neumann boundary conditions are evaluated. The normal flux at the barycenter of the boundary face j_N^k (N is an index running over all Neumann boundary faces of a sub-control volume) has to be given and is integrated by multiplication with the area of the boundary face. The flux can be different for each boundary face of a sub-control volume. As Neumann boundary fluxes are an input of mass into the system they are included in the source term Q_i^k:

$$Q_i(\mathbf{x}) = \sum_k q^w(\mathbf{x}_i^k) \cdot V_i^k + \sum_k \sum_N j_N^k \cdot F_N^k \tag{3.17}$$

3.2.2 Time Discretization

The equation is now discretized in space and proper boundary conditions have been specified. Now the time derivation in equation 3.6 must be taken care of. The time interval $(0, T)$ is divided into M time steps $t^0, \ldots, t^n, \ldots, t^M$. The duration of a single time step is $\Delta t^n = t^{n+1} - t^n$. An approximation for the differential quotient $\partial M_i / \partial t$ and a method to average the flux and source term $A_i + Q_i$ over a time step must be chosen. The differential quotient can be replaced by a difference quotient

$$\frac{\partial M_i}{\partial t} \approx \frac{\sum_{q=-r}^{1} a^{n+q} M^{n+q}}{\Delta t^n} \tag{3.18}$$

and the flux and source terms can be calculated from the values at the last time step and at the new time step

$$A_i + Q_i \approx \alpha \cdot (A_i^n + Q_i^n) + (1 - \alpha) \cdot (A_i^{n+1} + Q_i^{n+1}). \tag{3.19}$$

Values at time t^n are marked by the superscript n. If we select $r = 0$, $a^n = -1$ and $a^{n+1} = 1$ we get one-step methods, if $r > 0$ we get higher order schemes. Selection of $\alpha = 0$ yields explicit methods (the explicit Euler scheme for $r = 0$), $\alpha = 1$ fully implicit methods (the implicit Euler scheme for $r = 0$), and for $r = 0$ and $\alpha = 1/2$ we get the Crank-Nicolson scheme, which is second order accurate, but has a tendency to produce oscillatory solutions. Explicit and implicit Euler schemes are both first order accurate. UG provides explicit and implicit Euler schemes, a Crank-Nicolson scheme and BDF(2), a second order implicit scheme.

Only the implicit Euler scheme was used in this work. It provides a stable and non-oscillatory solution and global mass conservation is granted in combination with the spatial discretization described above. BDF(2) is only global mass conservative if the time step is constant, which is not desirable.

3.3   Solution of the Nonlinear Equation System

Discretization in space and time results in a system of nonlinear equations, which must be solved for every time step. The nonlinear equations are solved by an inexact Newton method. If we write the nonlinear equation system as

$$u_i(\mathbf{p}_l) = M_i^{n+1} - M_i^n - \Delta t^n \cdot (A_i^{n+1} + Q_i^{n+1}) = 0 \quad (i = 0, \dots, N), \tag{3.20}$$

an improved approximation can be calculated from a initial guess $\mathbf{p}_l^\nu$ by

$$u_i(\mathbf{p}_l^\nu) + \sum_{j=1}^N \frac{\partial\, u_i(\mathbf{p}_l^\nu)}{\partial\, p_{l_j}} \cdot (p_{l_j}^{\nu+1} - p_{l_j}^\nu) = 0. \tag{3.21}$$

A linear equation system

$$\boldsymbol{J}(\mathbf{p}_l^\nu) \cdot (\mathbf{p}_l^{\nu+1} - \mathbf{p}_l^\nu) = \mathbf{u}(\mathbf{p}_l^\nu) \tag{3.22}$$

must be solved for every Newton step, where $\boldsymbol{J}(\mathbf{p}_l^\nu)$ is the Jacobi matrix

$$\boldsymbol{J}(\mathbf{p}_l^\nu) = \begin{pmatrix} \frac{\partial\, u_1(\mathbf{p}_l^\nu)}{\partial\, p_{l_1}} & \cdots & \frac{\partial\, u_1(\mathbf{p}_l^\nu)}{\partial\, p_{l_N}} \\ \vdots & \ddots & \vdots \\ \frac{\partial\, u_N(\mathbf{p}_l^\nu)}{\partial\, p_{l_1}} & \cdots & \frac{\partial\, u_N(\mathbf{p}_l^\nu)}{\partial\, p_{l_N}} \end{pmatrix}. \tag{3.23}$$

The components of $\boldsymbol{J}(\mathbf{p}_l^\nu)$ are evaluated numerically:

$$\frac{\partial\, u_i(\mathbf{p}_l^\nu)}{\partial\, p_{l_j}} = \frac{u_i(\mathbf{p}_l^\nu + \Delta p_{l_j} \mathbf{e}_j) - u_j(\mathbf{p}_l^\nu)}{\Delta p_{l_j}}. \tag{3.24}$$

$\mathbf{e}_j$ is the j-th unity vector and $\Delta p_{l_j} = \epsilon \cdot (1 + |p_{l_j}^\nu|)$ with $\epsilon \in [10^{-10}, 10^{-6}]$ chosen as interval. The value of the previous time step is used as initial guess. The linear equation system is not solved exactly in every Newton step to save computation time. With increasing convergence, the precision with which the linear equation is solved is increased to secure the quadratic convergence of the Newton method. If a Newton step doesn't lead to convergence, a line search is done with an appropriate damping strategy (Bastian 1999).

3.4   Solution of the Linear Equation System

Direct resolution of the linear equation system in each Newton step using Gauss elimination would require $O(N^3)$ arithmetical operations for a grid with N nodes, which could be reduced to $O(N^{1.5})$ or $O(N^2)$ for two-dimensional and three-dimensional problems, respectively, if the sparsity structure of the matrix is taken into account. If multigrid methods are used, the convergence rate in each iteration step can be

shown to be independent of the mesh size for specific problems, the computational complexity is therefore $O(N)$ and thus optimal (Bastian 1999).

In this work the linear equation system in each Newton step is solved using a "Krylov subspace" method (BiCGSTAB) in combination with a multigrid method as preconditioner. An incomplete factorization is used as smoother in the multigrid scheme. A 'V' cycle is performed in the multigrid scheme with 2 presmoothing and 2 postsmoothing steps at each level. The coarse grid matrices are constructed from the discretized equations. If the system heterogeneities can not be represented on the coarse grid, the multigrid method will converge slower. In this case other solvers could be more advantageous. The PDE toolbox UG permits a parallel solution on various computer architectures, which is necessary especially for 3D simulations. For details see Bastian (1999).

3.5   Process Coupling

Various combinations of transport processes must be simulated to study the coupling between transport processes. Water transport is always calculated. It can be combined with any or all of the following: Energy transport, gas transport and solute transport. This means that between one and four equations per vertex must be solved. A fully coupled solution is wanted, so the coupling must be resolved by the Newton method. Technically this is achieved by using Macros and '`#ifdef`' statements in the program code and a flexible formulation of the numerical derivation of the Newton method. By a number of '`#define`' statements in a central include file the processes to be simulated can be chosen at compile time. Possible processes are gas transport, energy transport, water vapor transport, solute transport and osmotic transport[3]. The selection of the processes at compile time results in an optimal computation speed at high flexibility but requires some work at coding and makes the code a bit less readable. On the other hand, it enables the investigation of the effect of process coupling with essentially the same source code just by recompiling, which excludes many potential sources of error.

3.6   Variable Substitution

The liquid phase pressure p_l is no longer an independent variable (cf. section 2.4.1.3) and becomes a function of temperature T, when water starts to freeze in a porous medium. On this account the target variable of the solution processes has to be changed at the freezing point to ice saturation S_i. When the ice phase vanishes, the solution variable has to be switched back to p_l. In other models of freezing

---

[3]The diffusive transport of water resulting from the coupling of water and solute transport (section 2.4.4)

soils, approximations have been used to decouple the energy and water transport equations and avoid the variable switching.

Variable substitution is done at the end of a time step, when the Newton method converged. At every node it is checked if a change of the variable state/phase state is necessary. If variables have to be switched at a node, new initial guesses are calculated. For the other nodes the result of the last iteration is used as initial guess. The time step is then recalculated and the variable check is performed again. This is repeated until either no additional changes of variable state occur or a maximum number of iterations is reached. If the number of iterations is exceeded without convergence, the time step is reduced. Variable substitution after each Newton iteration was tested as well, but the convergence was bad and computational costs increased.

The variable state is changed if the freezing pressure calculated from temperature using the Clausius-Clapeyron equation (2.29) is larger than the capillary pressure p_c, or if the ice saturation S_i is negative[4] at a node. As there is no direct relation between ice content and capillary pressure, the new values for water pressure or ice content cannot be calculated directly from the old values. An initial estimate has to be made and the values have to be calculated by solving the nonlinear equation system for the time step again.

If water starts to freeze, temperature is buffered and will remain near to the freezing point until a huge amount of the water is frozen. If the variable state is changed to frozen, the temperature is approximated by the temperature for which the freezing pressure corresponds to the capillary pressure calculated for the node. The ice saturation is set to zero.

If the ice saturation becomes negative in thawing, the temperature calculated by the model is still very near to the temperature at which the ice phase vanished, but the liquid water content is too high. The temperature is therefore kept unchanged. An estimate for the capillary pressure is calculated from the total water saturation by inversion of the soil water characteristic. If the total water saturation is negative, the variable substitution process is interrupted and the time step is reduced. The volume weighted average of the capillary pressure in each sub-control volume is used for the node, to take heterogeneity into account.

3.7   Time Stepping

An adaptive time stepping is used. The time step is automatically reduced if no convergence is reached. If the time step reaches a lower limit, the simulation is

---

[4]A hysteresis for the switching is not used. In general the scheme converges. The attempt to insert a hysteresis resulted in patchy freezing with a wild pattern of frozen regions with huge ice accumulation and unfrozen regions.

terminated. The time step is increased, if the convergence rate in the first Newton iteration is better than a given limit, until a maximal time step is reached.

3.8   Testing and Verification

With increasing complexity of a computer model the probability of wrong results or numerical artifacts increases as well. The value of a model depends highly on the carefulness with which it has been tested. There are different possibilities to test a computer model:

- Calculation of mass balances.

- Plausibility checks on the results.

- Comparison with results calculated with other models.

- Comparison with analytical solutions.

3.8.1   Mass Balances

In the development of a computer model the calculation of mass balances serves two purposes. On the one hand mass and energy balance are an excellent indicator for program errors. On the other hand they are a good tool to control the quality of results calculated by iterative solution of nonlinear equation systems, as the finite volume scheme used for space discretization in combination with an implicit Euler scheme for time discretization is locally and globally mass conservative, if the equations are solved exactly.

Global mass balances for all components are computed in the model as well as a global energy balance. This is done by calculation of fluxes across Neumann and Dirichlet boundaries and the global storage, which is the sum of the storage at all non-Dirichlet vertices. The mass balance defect was in the order of computer precision for all calculations.

3.8.2   Comparison with Analytical Solutions

Analytical solutions are the best tool to check the accuracy of a numerical model. As they exist only for a small number of special problems, this method is limited by their availability.

For a complex model only single transport processes can be tested separately. There are no analytical solutions available for coupled transport in porous media.

3.8.2.1   Water Transport

The infiltration of water into an initially dry homogeneous soil with constant water content is described by the quasianalytical solution of Richards' equation by Philip (Kutilek and Nielsen 1994). The water content ($\theta_w = \Phi S_l$) profile is given by an infinite sum:

$$z(\theta_w, t) = \sum_{i=1}^{\infty} \eta_i(\theta_w) \cdot t^{i/2} \tag{3.25}$$

The functions $\eta_i(\theta_w)$ can be calculated from the diffusivity of the soil $D(\theta_w)$, the hydraulic conductivity $K_l(\theta_w)$ and from $\eta_{i-1}(\theta_w)$. The quasianalytical solution gives for the cumulative infiltration $I(t)$ and the infiltration rate $J_w(t)$:

$$
\begin{aligned}
I(t) &= \int_{\theta_{w_i}}^{\varepsilon} z \, d\theta \\
&= S \cdot t^{1/2} + (A_2 + K_l(\theta_{w_i})) \cdot t + A_3 \cdot t^{3/2} + \ldots + A_n \cdot t^{n/2} \tag{3.26} \\
J_w(t) &= \frac{1}{2} S \cdot t^{-1/2} + (A_2 + K_l(\theta_{w_i})) + \frac{3}{2} A_3 \cdot t^{1/2} + \ldots + \frac{n}{2} A_n \cdot t^{n/2-1} \tag{3.27}
\end{aligned}
$$

with

$$A_n = \int_{\theta_{w_i}}^{\varepsilon} \eta_n(\theta) \, d\theta; \qquad S = A_1$$

The coefficient S is called sorptivity.

Haverkamp et al. (1977) tested several water transport models and used Philip's quasianalytical solution. They give profiles of water content as well as parameters $A_1, \ldots, A_4$ for a clay soil (Yolo Light Clay) and a sandy soil.

The infiltration in both soils was simulated with the model. The hydraulic parameters given by Haverkamp et al. (1977) are shown in appendix A.

Initial and boundary conditions given as matrix head h_m by Haverkamp et al. (1977) for the Yolo Light Clay:

$$
\begin{array}{llll}
h_m = & -599.97 \text{ cm} & \text{if} \quad t < 0 & z \geq 0 \\
h_m = & 0.0 \text{ cm} & \text{if} \quad t \geq 0 & z = 0 \\
h_m = & -599.97 \text{ cm} & \text{if} \quad t \geq 0 & z = 300 \text{ cm}
\end{array}
$$

and for the sand:

$$
\begin{array}{llll}
h_m = & -61.5 \text{ cm} & \text{if} \quad t < 0 & z \geq 0 \\
h_m = & -20.73 \text{ cm} & \text{if} \quad t \geq 0 & z = 0 \\
h_m = & -61.5 \text{ cm} & \text{if} \quad t \geq 0 & z = 100 \text{ cm}
\end{array}
$$

Conversion to liquid phase pressure was done by $p_l = p_{atm} + \rho_l^w \cdot g \cdot h_m$. Spatial discretization width was 1 cm. A rectangular grid with four nodes in horizontal direction was used, yielding a total number of 404 nodes for the sand and of 1204 nodes for the Yolo Light Clay. For the sand a time step was $\Delta t = 5$ s, for the Yolo Light Clay the time step was adjusted automatically between $\Delta t = 40$ s and $\Delta t = 640$ s.
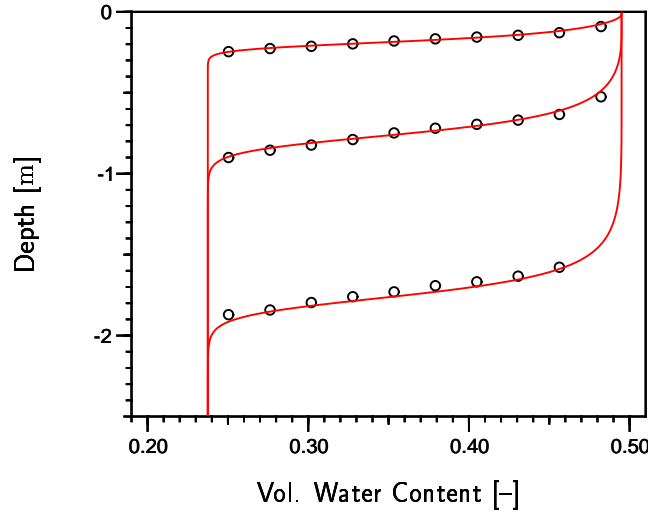
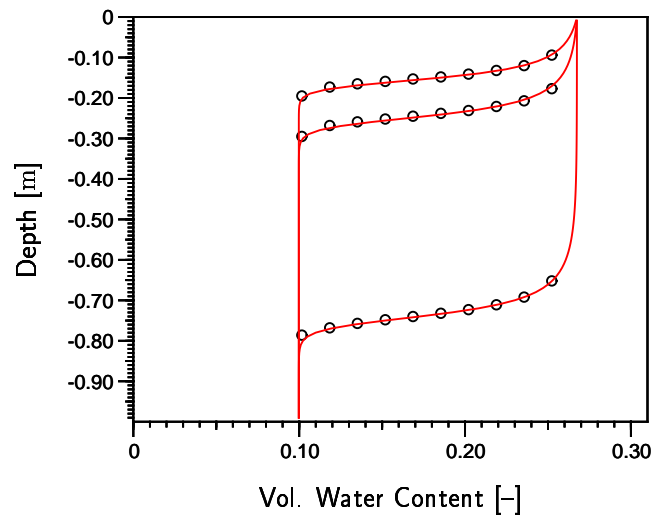Figure 3.3: Comparison of profiles calculated with the model (red) and with Philip's quasianalytical solution (black) for the Yolo Light Clay after 10^5 s, 10^6 s and $3 \cdot 10^6$ s

The relative mass balance error of $-3 \cdot 10^{-9}$ for the sand and $-9 \cdot 10^{-17}$ for the Yolo Light Clay at the end of the calculation was in the range of iteration precision. 18.5 minutes were needed to solve the system for the Yolo Light Clay and 40 seconds for the sand on a Athlon 1200 MHz system running Linux.

Water content profiles are shown in figure 3.3 and 3.5 together with values calculated using Philip's quasianalytical solution by Haverkamp et al. (1977). Figures 3.4 and 3.6 show the cumulative infiltration and the infiltration rates.

The agreement between values calculated from the quasianalytical solution and the modeled values was quite satisfactory. The models tested by Haverkamp et al. (1977) also showed small differences in the steepness of the infiltration front. With a limited amount of terms, Philip's quasianalytical solution is only valid for a limited time range. With 4 terms this time range is $t < 600$ h for the Yolo Light Clay and $t < 0.29$ h for the sand.

3.8.2.2 Heat-/Solute-/Gas Transport

Transport of a solute in a homogeneous, saturated porous medium is described by the convection-dispersion equation. For constant pore water velocity $v_l = \frac{J_l}{\Phi S_l}$ and the initial and boundary conditions

$$c_l^s = c_{l_i}^s \quad \text{if} \quad t < 0 \quad z \geq 0$$

$$c_l^s = c_{l_0}^s \quad \text{if} \quad t \geq 0 \quad z = 0$$

$$\lim_{z \to \infty} \frac{\partial c_l^s}{\partial z} = 0$$
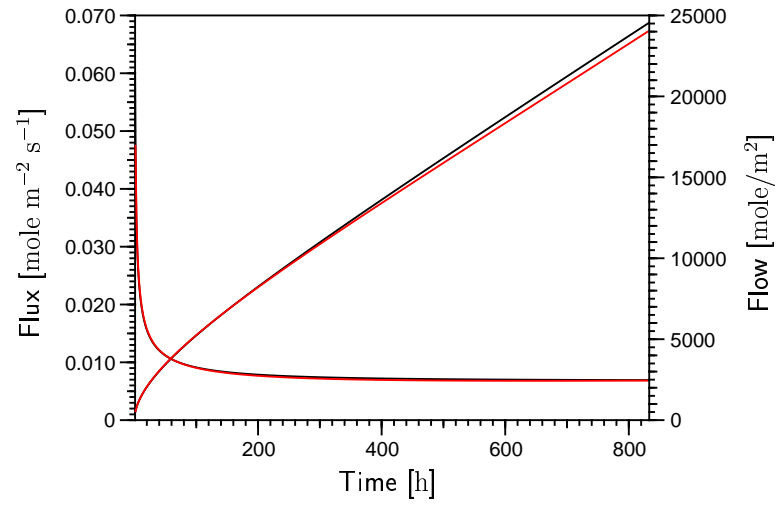
Figure 3.4: Comparison of infiltration rates and cumulative infiltration calculated with the model (red) and with Philip's quasianalytical solution (black) for the Yolo Light Clay

Figure 3.5: Comparison of profiles calculated with the model (red) and with Philip's quasianalytical solution (black) for the sand after 360 s, 720 s and 2880 s
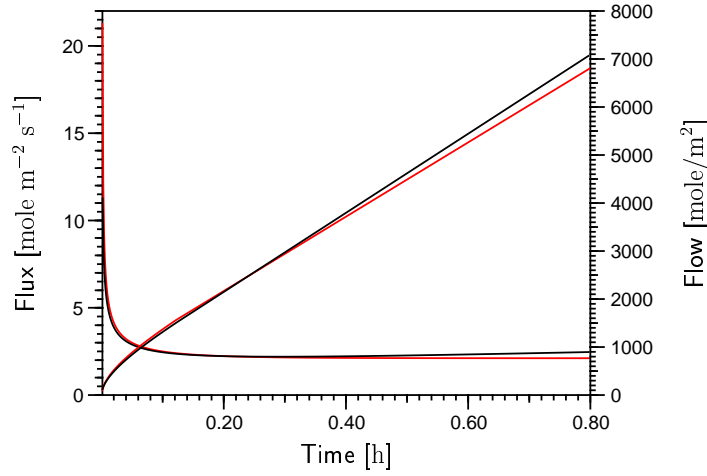
Figure 3.6: Comparison of infiltration rates and cumulative infiltration calculated with the model (red) and with Philip's quasianalytical solution (black) for the sand

the concentration is given by:

$$c_l^s(z,t) = c_{l_i}^s + (c_{l_0}^s - c_{l_i}^s) \cdot A(z,t) \tag{3.28}$$

with

$$A(z,t) = \frac{1}{2}\mathrm{erfc}\left[\frac{z - v_l t}{\sqrt{4D_l^s t}}\right] + \frac{1}{2}\exp\left(\frac{v_l z}{D_l^s}\right)\mathrm{erfc}\left[\frac{z + v_l t}{\sqrt{4D_l^s t}}\right] \tag{3.29}$$

The same equation can be used for the transport of dissolved air if the partial pressure p^a instead of c_l^s and apropriate effective parameters are used. The equation can also be adjusted for heat conduction and convective transport of heat, if T_i and T_0 are defined analogue to $c_{l_i}^s$ and $c_{l_0}^s$:

$$T(z,t) = T_i + (T_0 - T_i) \cdot B(z,t) \tag{3.30}$$

with

$$
\begin{aligned}
B(z,T) \;=\; & \frac{1}{2}\mathrm{erfc}\left\{ \frac{[(1-\Phi)\,C_s + \Phi C_l^w]\,z - C_l^w J_l t}{\sqrt{4\,[(1-\Phi)\,C_s + \Phi C_l^w]\,\lambda t}} \right\} \\
& + \frac{1}{2}\exp\left(\frac{C_l^w J_l z}{\lambda}\right)\mathrm{erfc}\left\{ \frac{[(1-\Phi)\,C_s + \Phi C_l^w]\,z + C_l^w J_l t}{\sqrt{4\,[(1-\Phi)\,C_s + \Phi C_l^w]\,\lambda t}} \right\}
\end{aligned}
\tag{3.31}
$$

Table 3.1: Parameters used for the calculation of heat, solute and gas transport

parameter	value	unit
Φ	0.43	–
S_l	1.0	–
λ	2.0	W m^{-1} K^{-1}
C_s	$1.9 \cdot 10^6$	J m^{-3} K^{-1}
C_l^w	$4.198 \cdot 10^6$	J m^{-3} K^{-1}
$D_l^a = D_l^s$	$2 \cdot 10^{-7}$	m^2/s
T_i	293.15	K
T_0	298.15	K
p_i^a	0.0	Pa
p_0^a	101300	Pa
$c_{l_i}^s$	0.0	mole/l
$c_{l_0}^s$	$1.0 \cdot 10^{-3}$	mole/l
Δz	1.0	cm
column length	5.0	m
Δt	1/256	h
simulation time	12	h

To get something similar to a semi-infinite column, a domain with a length of 5 m was used (with 4 nodes in horizontal directions this yields a grid with 2004 nodes). Simulation parameters are given in table 3.1. $T = T_i$ was used as lower boundary condition. The solution for $t = 0.25$ d and $t = 0.5$ d was calculated using Maple V Release 5. Two scenarios have been simulated: For scenario 1 pore water velocity was set to $v_l = 5$ cm/h corresponding to a flux density of $J_l = 0.331$ mole m^{-2} s^{-1}; for scenario 2 pore water velocity was set to zero, yielding pure diffusion. Transport of water, the solute, dissolved air and heat were simulated simultaneously. The diffusion coefficient for the solute and dissolved air were multiplied by 100 to get diffusion and heat conduction into the same time scale.

Computing time was 36 minutes for scenario 1 and 33 minutes for scenario 2. Absolute mass balance was zero for the solute in both scenarios and $-4 \cdot 10^{-9}$ and zero for the gas, for the water the relative mass balance error was $2 \cdot 10^{-14}$ in both scenarios and the energy balance error was $-1 \cdot 10^{-9}$ in both scenarios. The analytical solution and the numerical solution are shown in figures 3.7, 3.8, 3.9 and 3.10. The agreement between modeled and simulated data is quite satisfactory. Some numerical diffusion can be seen for the dissolved gas and solute transport in scenario 1, which is to be expected for the discretization scheme used.
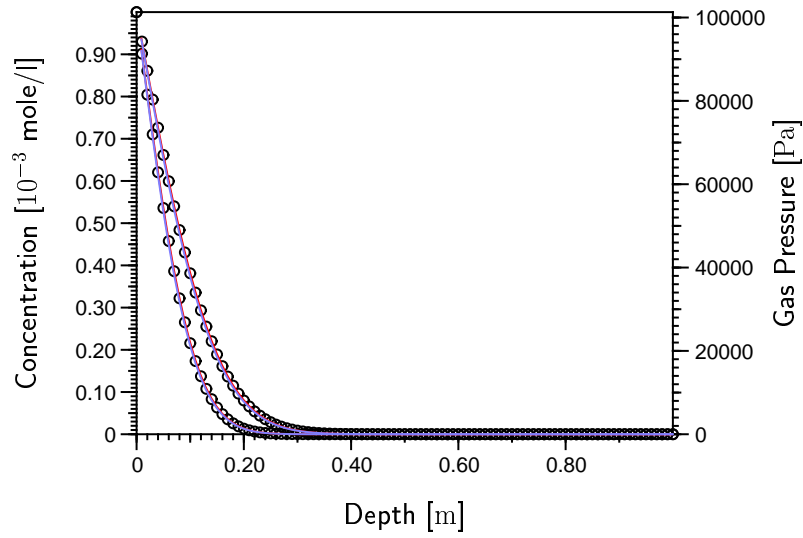
Figure 3.7: Comparison of the simulated partial pressure of air (blue) and solute concentration (red) profiles and the analytical solution (black circles) with pure diffusion
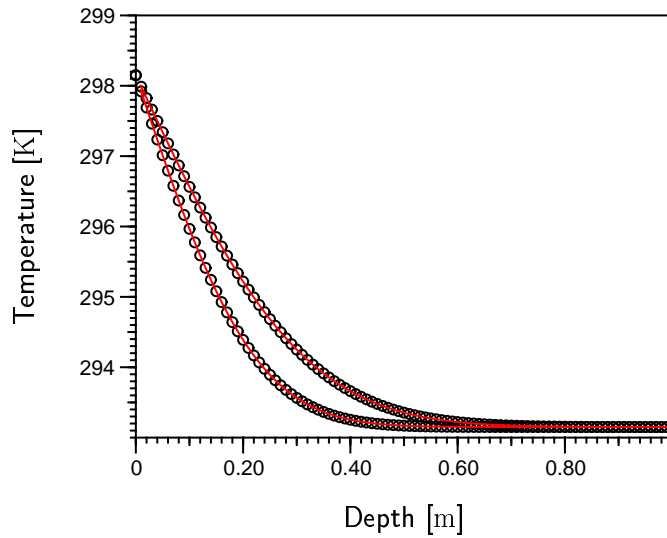

Figure 3.8: Comparison of the simulated temperature profile (red) and the analytical solution (black circles) with pure heat conduction
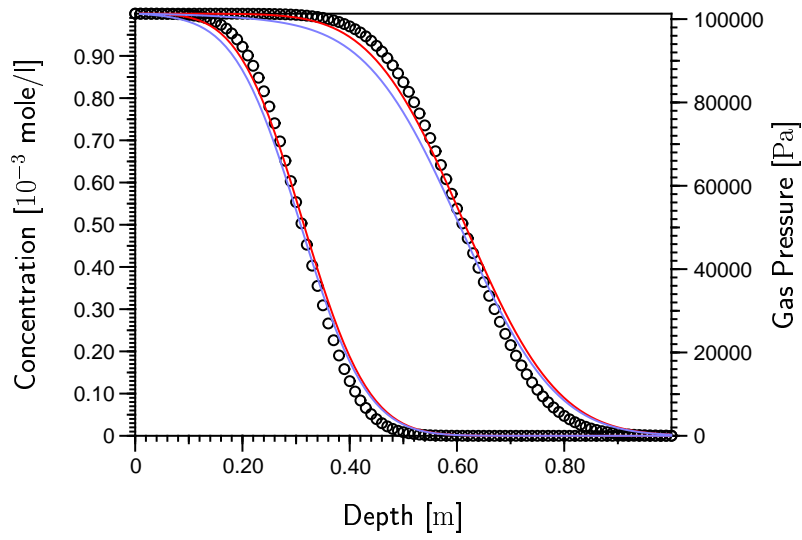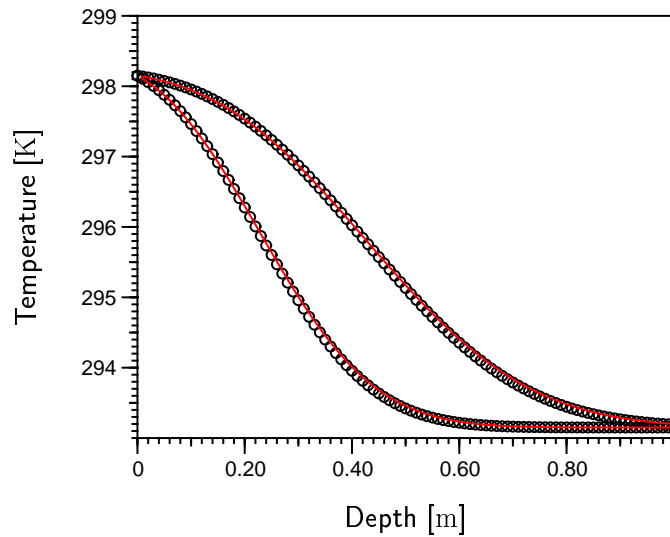
Figure 3.9: Comparison of the simulated partial pressure of air (blue) and solute concentration profiles (red) and the analytical solution (black circles) with convection

Figure 3.10: Comparison of the simulated temperature profile (red) and the analytical solution (black circles) with convection

4 Application: Simulation of a Permafrost Soil

Freezing soils are especially interesting systems, as water, heat and solute transport are strongly coupled in freezing soils. Soil freezing is hard to explore in temperate climate, because of the short time scale of freezing and the shallow penetration depth. Permafrost soils with their strong yearly dynamic are a much better object to study the freezing of soils. After a brief discussion of the processes in permafrost soils, measurement results from a field site in Spitsbergen are compared with model calculations.

4.1 Dynamics of Permafrost Soils

The dynamic of the active layer at a permafrost site can be subdivided into four periods: During fall freeze-back an expanded isothermal region with temperatures very near to 0 °C (the so called "zero curtain") develops, which vanishes when the soil is completely frozen. In spring the soil warms up again, snow melts and meltwater may infiltrate into the soil. Finally the soil thaws again gradually.

Several transport processes may be involved in heat transfer. While heat conduction is undoubtedly the most important process, other mechanisms are discussed as well. Migration of liquid water may contribute to heat transport during freezing and thawing. Hinkel and Outcalt (1993) showed that infiltration of precipitation can be important in the summer. Ray et al. (1983) and Krantz (1990) even argued that density driven convection of water in the thaw period initiates the formation of sorted circles, which is shown to be unlikely by Putkonen (1998). Infiltrating and refreezing snowmelt water may also be responsible for the rapid warming of soil in spring, when the relevance of non-conductive heat transfer processes is supported by many authors (e.g. Putkonen 1998, Hinkel and Outcalt 1994). The transport of latent heat with liquid water may also stabilize the "zero curtain", developing in fall due to the buffering effect of latent heat released by freezing water. Hinkel and Outcalt (1993) and Hinkel and Outcalt (1994) suggest that water vapor transport driven by osmotic gradients may be involved in the heat transfer across this nearly isothermal zone, but Romanovsky and Osterkamp (2000) demonstrated that

soil temperatures during freeze-back can be predicted by including conductive heat transfer and the effects of unfrozen water without vapor transport. Roth and Boike (2001) argue that water vapor transport may be important throughout the whole year. Water vapor transport is definitely important in the summer, when evaporation from the surface consumes between 25 and 65 percent of total energy, as measured by Boike et al. (1998) in Siberia and Kane et al. (1990) in Alaska.

The importance of the different heat transfer processes is rarely quantified. Ice and vapor content of soils can at the moment hardly be measured with the necessary resolution in space and time, neither in the laboratory nor in the field. Modeling of heat transfer in frozen, unsaturated soils is complicated by the strong coupling of a number of components (ice, liquid water, vapor, air, solutes, soil matrix).

4.2   Field Experiment

In the Bayelva catchment about 3 km from Ny-Ålesund, Svalbard ($78°55'$ N $11°50'$ E) a measurement site was instrumented at the end of August 1998, together with Paul Overduin and Dr. Julia Boike from the Alfred-Wegener Institute, Potsdam, who organized and headed the installation. The field site is located on top of a small hill, called Leirhaugen in the northern forefield of the East Brøggerbreen glacier. A nearly horizontal plateau of about a hundred square meters on top of the hill, approximately 25 m above sea level, is covered with unsorted circles (Figure 4.1). Each circle consists of a mound of bare soil with a maximum height of about 15 cm and a diameter of about 1 m and a surrounding ring of mosses, low vascular plants and lichens (Figure 4.2).

The coastal areas in the region are underlain by continuous permafrost with a depth of about 100 m, which can increase up to 500 m in mountainous regions (Liestøl 1977). As a consequence of the North Atlantic Current, the climate is quite warm for the high latitude and rain on snow events can happen even in mid winter. Average air temperatures are 5 °C and −13 °C in July and January, respectively, and annual precipitation is 400 mm mainly deposited as snow between September and May.

4.2.1   Instrumentation

A 2 m wide and 1.4 m deep profile was dug across one of the unsorted circles (Figure 4.3). The soil material was separated according to depth and the surface was cut carefully, to improve the restoration of the profile and the surface after the instrumentation. The unfrozen layer was 1.2 m deep. The whole profile was quite heterogeneous. The texture was mainly silty clay with a stone content below 10 percent, and an average organic carbon content of one percent in the upper part of the soil. The stone content rises up to 50 percent in a slightly inclined layer in
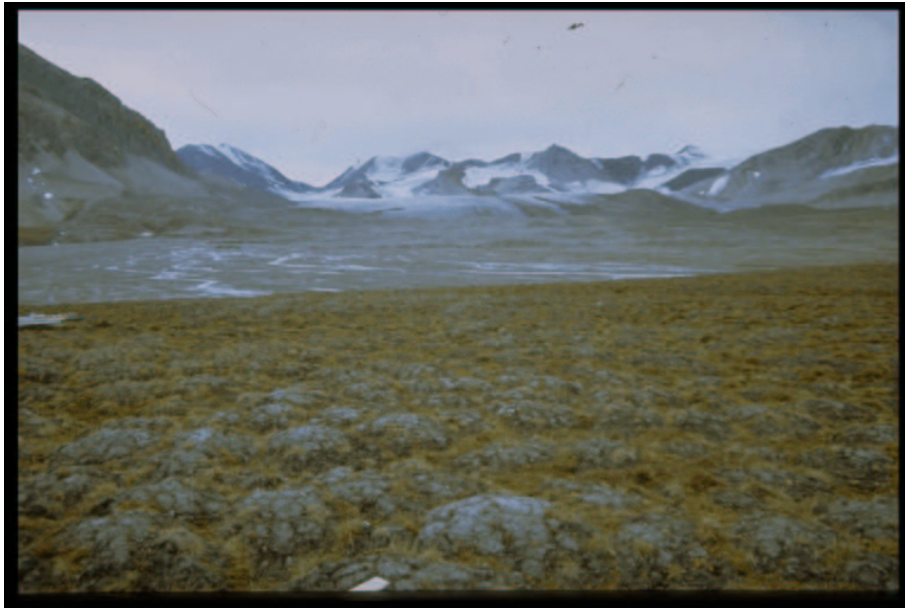
Figure 4.1: View from Leirhaugen hill southward over the Bayelva catchment toward
         the East Brøggerbreen glacier (Photo: J. Boike)

50 cm depth, approximately 20 cm thick. The stones are quite massive (> 6 cm
diameter). At the bottom of the profile (> 85 cm) the soil is coal rich with massive
coal lenses. The stones in the profile are not oriented.

Soil samples were taken for texture and density analysis. Measured clay content
increases from 20 percent near the surface to over 60 percent in depths below 0.8 m
with a corresponding decrease of silt and sand content. Plots of the texture and
nitrogen, sulfur and organic carbon content can be found in appendix B. The
average bulk soil density obtained from 6 samples is $1.70 \cdot 10^3$ kg/m^3, porosity varies
between 0.36 and 0.5 (Roth and Boike 2001).

The profile was instrumented with an array of 32 thermistors and 32 horizontal
TDR[1]-probes of 24.3 cm and 50 cm length, two heat flux plates, another TDR-probe
with 1 m length installed vertically and a well to measure ground water table. The
thermistors were calibrated at 0 °C with a precision of ±0.000024 °C and an absolute
error of less than ±0.02 °C over a temperature range ±30 °C. The TDR-probes were
used to measure dielectric constant (to derive unfrozen water content) and bulk soil
conductivity. Calibration was done in pure water, air and NaCl-solutions of varying
conductivity.

A climate station was installed within 5 m of the instrumented profile measuring
net radiation, solar radiation, air and snow temperature in different heights, precip-
itation, wind speed and direction and snow depth above the profile. The rain gauge

---

[1]Time Domain Reflectometry

Figure 4.2: Surface of the selected unsorted circle before instrumentation
(Photo: J. Boike)
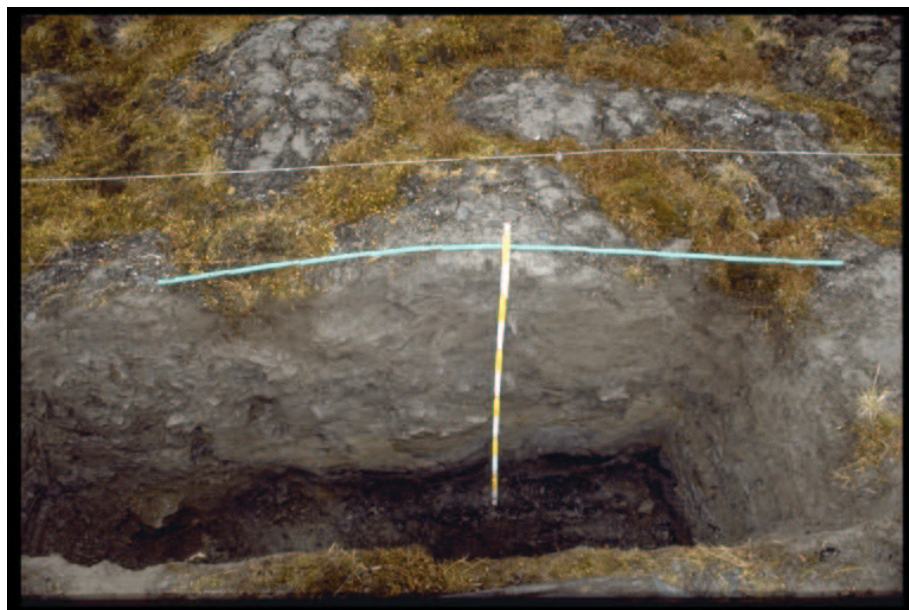
Figure 4.3: Soil profile of the unsorted circle. The dark color at the bottom is partly
a result of reduction processes and partly caused by the presence of coal
lenses (Photo: J. Boike)
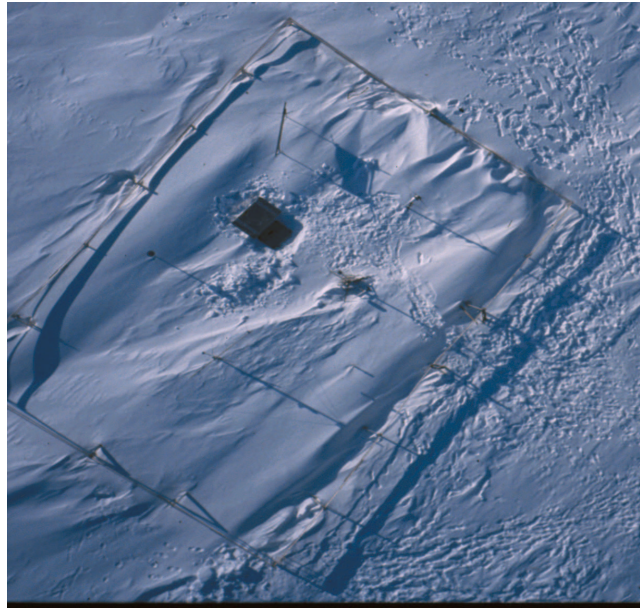
Figure 4.4: Aerial view of the field site in April 2000 showing the influence of the fence on snow accumulation (Photo: J. Boike)

is not heated. Comparison with data measured at Ny Ålesund showed reasonable agreement for the measured liquid precipitation. The whole measurement system is powered by a solar panel and a wind generator.

To protect the instruments against wild reindeer a fence had to be erected. The fence increased the snow accumulation markedly (Figure 4.4).

Data collection started on September 15, 1998. Snow depth and TDR waveforms were measured daily until the 17th of March 1999, after which they were measured every 12 hours. TDR measurements evaluated with the built-in algorithm of the data logger are done every hour between waveform measurements. All other data are measured hourly. Major data gaps exist between 14th November and 9th December 1998 and 24th May and 1th July 2001 due to a failure of power supply and data storage, respectively. Precipitation data are not available before August 1999, the humidity sensor was installed in April 2000. Data are stored on memory cards and collected every two months by the station manager of the Alfred-Wegener-Institute's Koldewey-Station in Ny Ålesund.

4.2.2 Data Preparation

To handle the huge amount of data, programs for the semi-automatic insertion of the collected data into a PostgreSQL database and automatic data evaluation have been written. The database is available to the cooperating scientists over the internet.

Special attention has been given to the derivation of the relative permittivity
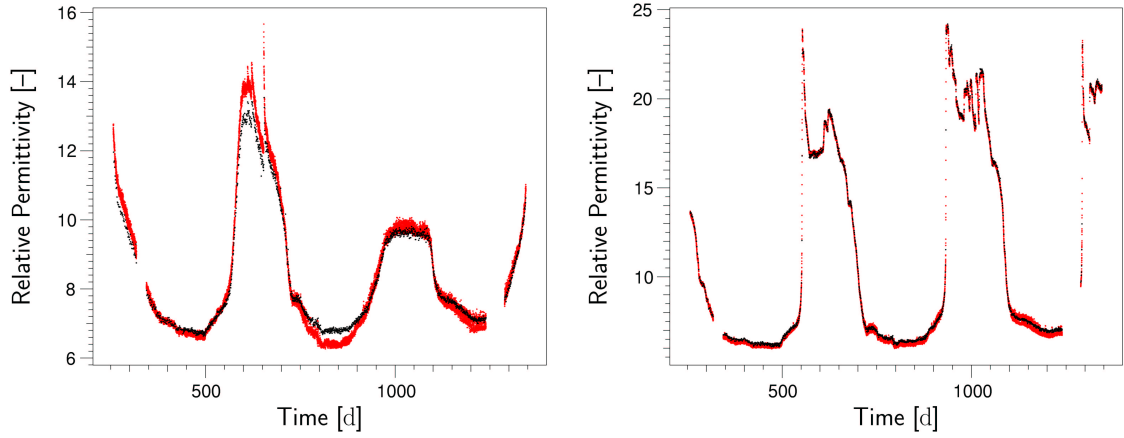
Figure 4.5: Comparison of relative permittivity determined by the datalogger algorithm (red) and the modified Heimovaara algorithm (black) for two selected probes

from the TDR-waveforms. In TDR, the travel time of a signal pulse along a wave guide is measured. The travel time depends on the relative permittivity of the material between the probes and in its immediate vicinity. The reflection signal is measured using a Tektronix 1502C cabletester. To get the travel time, the reflection points at the probe start and end have to be determined. The Campbell CR10X datalogger used has a built-in routine to do this. The reliability of this algorithm in frozen soils was not clear. An existing algorithm published by Heimovaara (1993) was modified for better stability. The modified algorithm is described in appendix C. The results obtained with the two algorithms (Figure 4.5) show a similar trend, but a small offset of varying size and direction. The signal determined by the datalogger's algorithm is also a bit noisier. Because of the higher temporal resolution, we decided to use the values determined by the datalogger and filter the signal for runaway values.

To filter the measured data, the following procedure was applied: Impossible values (e.g. relative permittivities above 80 or below zero) were removed first. For data which are continuous in time (e.g. temperature, relative permittivity) the standard deviation and the average of 10 values before and 10 values behind each data value was calculated. If a time gap longer than 7 days was detected the time series before and behind were treated separately. A value was rejected if the difference between the value and the average was larger then three times the standard deviation. Finally some obvious runaway values were removed manually. Missing values were interpolated afterwards and a five point moving average was applied to the measured dielectric permittivities to remove noise generated by the measurement. Figure 4.6 shows the relative permittivity measured at a probe before and after filtering. From
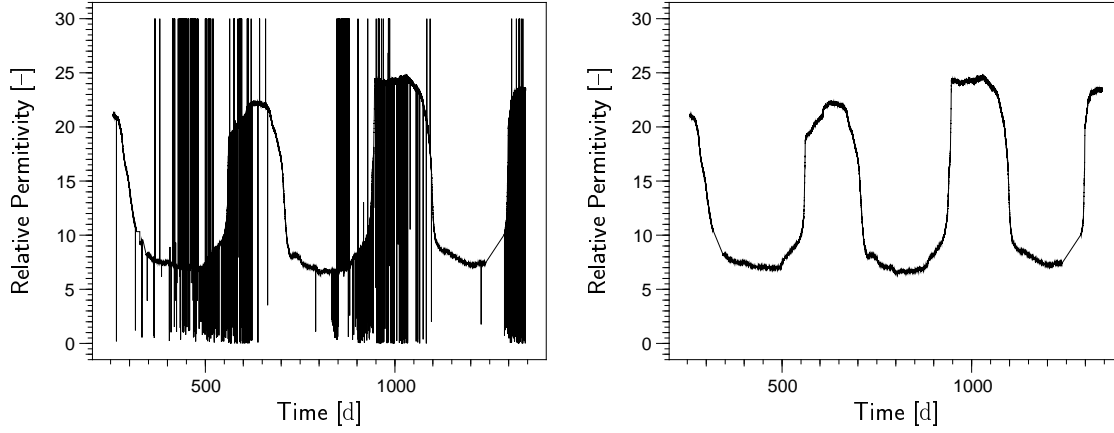
Figure 4.6: Data measured at a TDR-probe before (left) and after (right) filtering (8.6 % of the values were rejected), interpolation and smoothing

the interpolated data daily average values were calculated as well.

4.2.3   Climate

Figures 4.7 to 4.9 show the weather parameters measured at the field site (no smoothing or interpolation was done for these values). Time is given in julian days starting at the first of January 1998. Air temperature and solar radiation show the characteristic annual cycle of an arctic site. The snow cover is usually shallow at the beginning of winter and reaches a thickness of around 1 m in spring. Precipitation shows rain on snow events characteristic for Spitsbergen (around days 680, 800, 1000). The air temperature varies between −30 °C and 15 °C, the humidity is always quite high.
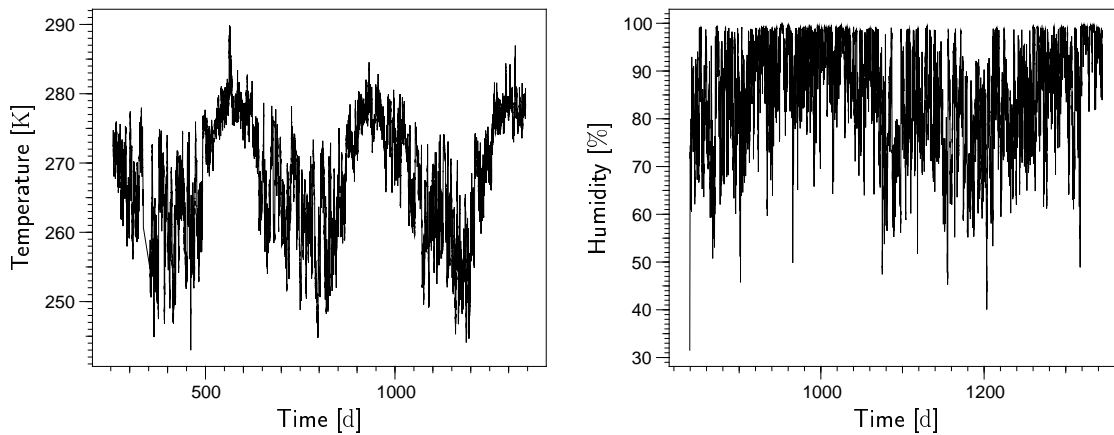
Figure 4.7: Air temperature and humidity at 2 m height at the Bayelva site
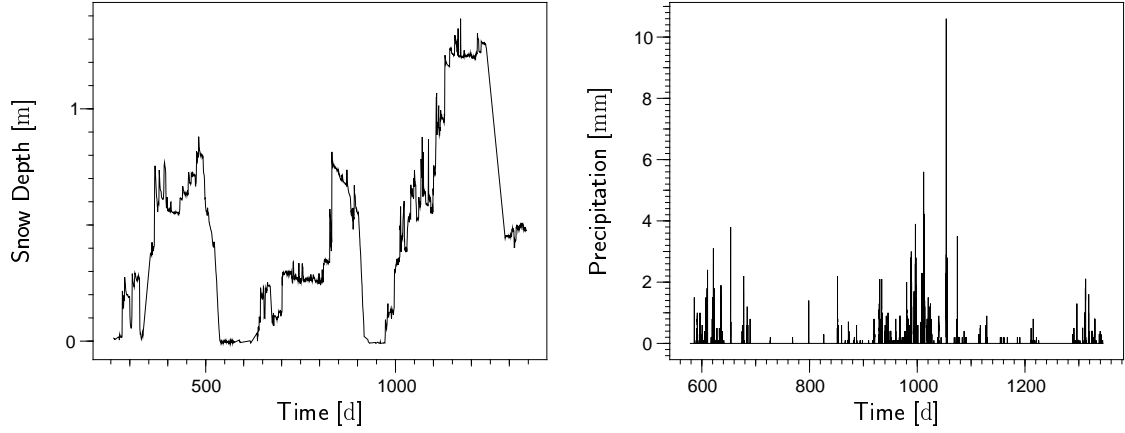
Figure 4.8: Snow depth and precipitation at the Bayelva site
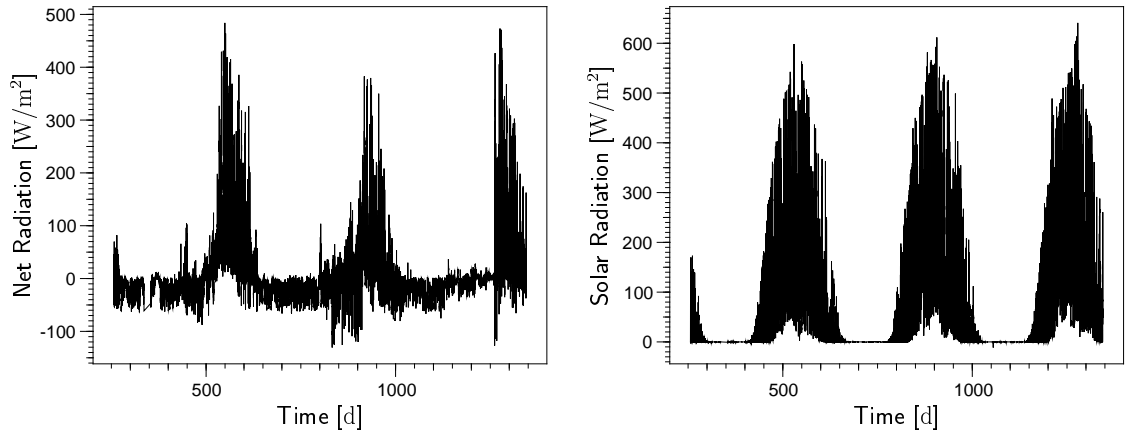
Figure 4.9: Solar and net radiation at the Bayelva site

4.2.4   Model Parameters

4.2.4.1   Transport Parameters

Unfortunately the undisturbed soil cores were destroyed after the measurement of bulk density. As a consequence it was not possible to measure the soil hydraulic parameters independently. Besides texture information from disturbed samples, the temperature and relative permittivities measured in the field, are the most valuable information about hydraulic parameters.

The volumetric liquid water content $\theta_l = S_l \cdot \Phi$ of a soil can be derived from the measured relative permittivity ϵ_m using a mixing model, dielectric permittivities of

the soil matrix ϵ_s and air ϵ_a and the temperature dependent relative permittivity of liquid water $\epsilon_w(T)$ (Roth et al. 1990):

$$\theta_l = \frac{\epsilon_a^\alpha - (1-\Phi)\epsilon_s^\alpha - \Phi \cdot [S_i\epsilon_i^\alpha + (1-S_i)\epsilon_a^\alpha]}{\epsilon_w^\alpha(T) - \epsilon_a^\alpha} \tag{4.1}$$

$$\epsilon_w(T) = 78.54 \left[1 - 4.579 \cdot 10^{-3}T^* + 1.19 \cdot 10^{-5}T^{*2} - 2.8 \cdot 10^{-8}T^{*3}\right]$$
$$\text{with } T^* = T/K - 298.15 \tag{4.2}$$

For this study a value of 0.5 was used for the exponent α. In frozen soils also ice saturation and relative permittivity of ice ϵ_i must be known. As there is no easy method to measure the ice content independently and the available methods to measure the total water content (γ-ray attenuation, neutron probes) can not be used in automated field stations in the arctic, this problem can only be resolved through additional assumptions. If the total water saturation S_{tot}^w (ice plus liquid water) is assumed to be constant, the ice saturation is given by $S_i = S_{\text{tot}}^w - S_l$ and the volumetric liquid water content can be calculated from:

$$\theta_l = \frac{\sqrt{\epsilon_m} - (1-\Phi)\sqrt{\epsilon_s} - \Phi\left[(1-S_{w_{tot}})\sqrt{\epsilon_a} - S_{\text{tot}}^w\sqrt{\epsilon_i}\right]}{\sqrt{\epsilon_w(T)} - \sqrt{\epsilon_i}} \tag{4.3}$$

This assumption is not true in freezing soil, since water moves toward the freezing front, but it seems more reasonable then to assume an ice content of zero. The error caused by the estimation of the ice content is reduced by the ratio of $\sqrt{\epsilon_w}$ and $\sqrt{\epsilon_i}$, which is approximately 9:2.

After filtering of the data as described above, all volumetric water content data corresponding to below zero temperatures were plotted against temperature. The plots are shown in appendix D together with freezing curves derived from hydraulic parameter sets for a silt and a loam given by Roth (1996). All plots show a clear relation between liquid water content and temperature, some of them display signs of hysteresis and some variation between different winters. Maybe movement of the probes due to upfreezing or changes due to mechanical forces may be responsible for these variations. The minimal unfrozen water content varies between zero and ten percent. Three general types of curves can be distinguished (Figure 4.10). Most curves are very similar to the loam and silt curve in curvature and minimal unfrozen water content. Deviating freezing characteristics can be found below the vegetation at the surface, where the curve is much steeper and the liquid water content decreases nearly to zero at low temperatures, and in a layer approximately 60 to 100 cm deep, where the water content decreases markedly slower. This layer corresponds well with a region of increased clay content.

As most of the probes correspond quite well with the silt as well as the loam curve, both hydraulic parameter sets (Table 4.1) were used to study the influence of hydraulic parameters on the model result in homogeneous simulations.
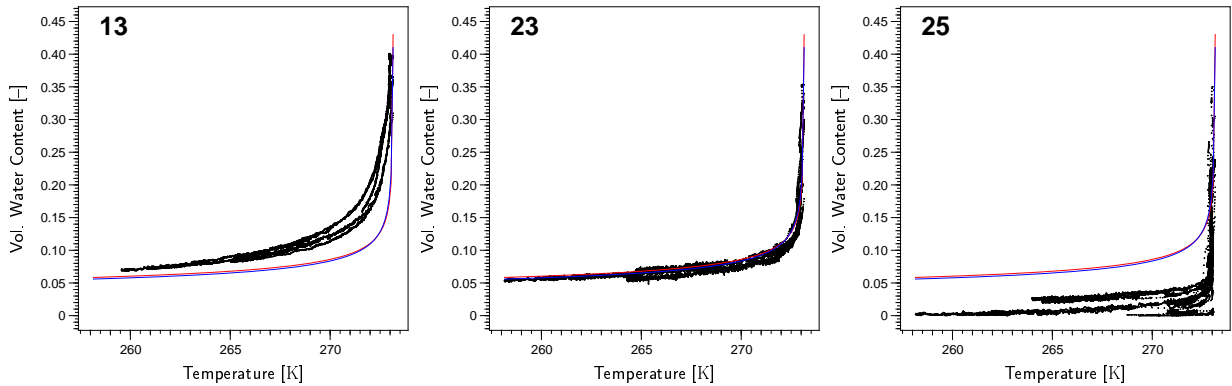
Figure 4.10: Freezing characteristic for a probe indicating higher clay content (left), a probe typical for most of the profile (middle), and a probe indicating higher sand content (right). The lines were derived from hydraulic parameters for the loam (red) and the silt (blue) used in the simulations.

The thermal conductivity was calculated using the de Vries model. It was assumed that the sand fraction plus half of the silt fraction was composed of quartz and half the silt fraction plus the clay fraction were composed of other soil minerals, for which de Vries (1963) gives conductivities of 8.54 W/m K and 2.0 W/m K respectively. The change of thermal conductivity with temperature was neglected. The average organic matter content measured from disturbed samples was 2.0 percent. A conductivity of 0.25 W/m K was used for the organic matter. For the calculation of volumetric fractions from the weight fractions, a density of 2.65 g/cm^3 was used for quartz and the minerals and 1.0 g/cm^3 for the organic matter, which yields volumetric fractions of 0.29, 0.66 and 0.05 for quartz, other minerals and organic matter, respectively. Volumetric heat capacity of $1.93 \cdot 10^6$ J m^{-3} K^{-1} was used for quartz and other minerals and $2.51 \cdot 10^6$ J m^{-3} K^{-1} for the organic material (de Vries 1963). Molar heat capacities of 75.8 J mole^{-1} K^{-1} for water, 37.1 J mole^{-1} K^{-1} and 28.98 J mole^{-1} K^{-1} for the gas phase were derived from values given by de Vries (1963).

4.2.4.2   Pseudo-Mechanical Submodel

As discussed in section 2.4.7, a simplified mechanical model is needed for the simulation of frozen conditions. The basic assumption is a fully elastic expansion of the soil, if the pores are completely filled with ice and water. In reality this would lead to an expansion in volume and an increase in porosity. As the structural change of the soil is not simulated, it was convenient to keep the volume and the porosity constant in the program thus securing the conservation of mass for the soil matrix and to allow the total saturation to rise above one. This is only allowed if ice is present in the soil.

The effect of soil expansion on the liquid phase conductivity is not considered, which leads to an overestimation of liquid water flux. As the saturations are used for the calculation of the energy storage, energy conservation is granted. For the calculation of the heat conductivity and diffusion coefficients, saturations are normalized to one. This leads to an overestimation of heat conductivity, but as the expansion is also not considered in the calculation of temperature gradients this is partly compensated. As the mechanical approximation as a whole is quite crude, it does not seem reasonable to make further improvements in parameter calculations.

If the soil is frozen, the total saturation is given by the sum of ice and liquid water saturation, which is only a function of temperature. It is assumed that an ice pressure builds up proportional to the excess saturation, with a proportionality constant called *soil rigidity*, as long as the effective stress is smaller than an assumed *soil stability* plus the weight of the overburden, which is calculated from the depth and an assumed soil density of 1500 kg/m^3. If the effective stress exceeds this limit it is assumed, that the additional increase of ice pressure is only proportional to the weight of the overburden. The values used for *soil rigidity* and *soil stability* can be used to study the influence of soil rigidity. A *soil rigidity* of 100'000 Pa and a *soil stability* of zero was used in the calculations.

The whole method is only a very crude tool and is only valid if the amount of excess ice is small, but as long as soil mechanics are not simulated explicitly it seems a reasonable solution.

4.2.4.3 Boundary Conditions

In winter the snow cover serves as a good insulation between the soil and the atmosphere and in spring the snow melt provides much melt water, which infiltrates partially into the soil. As visual ice layers develop at the bottom of the snow pack (Boike et al. 2001) an appreciable amount of water will run off at the surface. Temperature and water pressure or ice content derived from the relative permittivity at

Table 4.1: Hydraulic parameters used in the model calculations

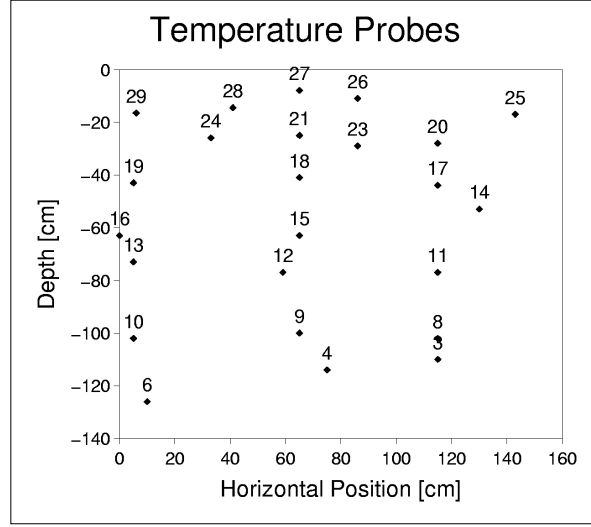| parameter	loam	silt	unit
Φ	0.43	0.41	–
α	1.6	0.7	m^{-1}
n	1.25	1.3	–
m	$1 - \frac{1}{n}$	$1 - \frac{1}{n}$	–
S_{r_l}	0.0	0.02	–
τ	0.0	0.0	–
K	$3.06 \cdot 10^{-13}$	$1.03 \cdot 10^{-12}$	m^2

Figure 4.11: Position of the probes used in the simulation

the uppermost layer of probes[2] was used as upper boundary condition to avoid modeling of the snow pack and atmosphere/surface interactions. Daily averaged data were used and values were linearly interpolated in space and time between probes and measurement times. Lower boundary conditions were derived in the same way from the measured values at the lowest horizontally installed probes[3]. The boundary conditions are retrieved from the database at runtime using the PostgreSQL database access library. As the plot was nearly horizontal, no-flux boundary conditions were used at the sides of the profile.

A three-dimensional simulation was also done. As temperatures are only measured along a line, some assumptions were necessary to get a two-dimensional field of temperature and relative permittivity. A cylindrical domain was used for the three-dimensional simulation. For each point (x,y) the horizontal distance $r = \sqrt{(x - x_0)^2 + (y - y_0)^2}$ from the center of the domain was calculated. The temperatures T_1 and T_2 are the temperatures for the points $(x_1,0)$ and $(x_2,0)$ with the same distance from the center along the measured transect. They are derived using linear interpolation in space and time as in the two-dimensional case. The temperature

$$T = T_1 + \frac{x - x_1}{x_2 - x_1} \cdot (T_2 - T_1). \tag{4.4}$$

is then used as boundary condition at the point (x,y). The same approach is used

---

[2]Probes 25, 26, 27, 28 and 29 were used for the upper boundary condition. As probe 25 and 29 were located outside the simulated region, the simulated and measured values are not identical.

[3]Probes 3,4 and 6
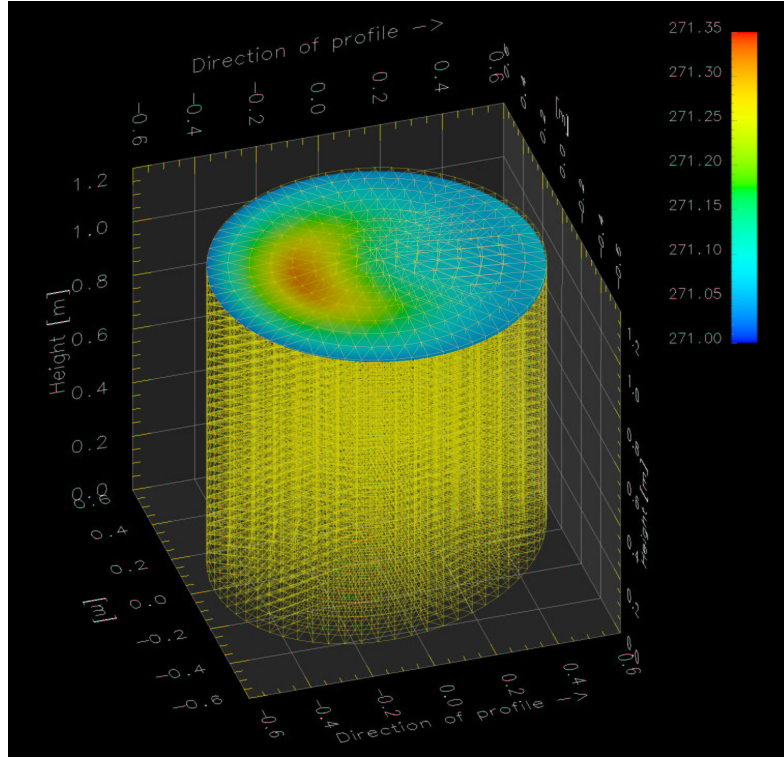
Figure 4.12: Plot of 3D domain with a cross section showing temperature

to calculate the permittivity and height of a surface point. A typical result is shown in figure 4.12

To avoid the assumption of constant total water saturation used in the calculation of liquid water content above, the evaluation of relative permittivity for the boundary conditions is done at runtime. When the soil is unfrozen, liquid water content is calculated using 4.1 and capillary pressure is derived from the inversion of the soil water characteristic used in the model at the particular position. To avoid numerical problems, maximum liquid phase saturation was limited to 0.95, which is acceptable given the precision of the TDR probes. When the soil is frozen, liquid phase pressure can be calculated from temperature and volumetric liquid water content can be derived from the soil water characteristic. Ice content θ_i is then calculated by:

$$\theta_i = \frac{\sqrt{\epsilon} - (1 - \Phi)\sqrt{\epsilon_s} - \theta_l\sqrt{\epsilon_w(T)} - (\Phi - \theta_l)\sqrt{\epsilon_a}}{\sqrt{\epsilon_i} - \sqrt{\epsilon_a}} \tag{4.5}$$

With a given set of hydraulic parameters it may not always be possible to reproduce the measured relative permittivity at the boundary with the model, as the liquid water content is given by temperature and soil water characteristic, and even if the remaining pore volume is completely filled with ice this may not be sufficient for the difference.

These boundary conditions are quite strong as probes near the boundary are influenced primarily by the boundary conditions and will be near to the measured values for all sets of model parameters. Probes in the middle of the profile are therefore much more interesting.

4.2.4.4   Initial Conditions

Measured values were also used as initial condition. A linear interpolation was used in the region between the probes. The initial conditions were also retrieved from the database at runtime, which prevents errors resulting from file handling and makes the change of starting time quite easy.

For the three-dimensional simulation the same scheme used for the boundary conditions is used to compute initial values for temperature and permittivity. Interpolation is done between values at the same height with the same distance from the center. If there is only one value with the same distance from the center, which is possible in the lowest part of the profile where the left side of the profile is deeper, this value is used unchanged.

4.3   Simulation Results

Several scenarios have been simulated for a time span of 982 days beginning at the 13th of September 1998 and ending at the 23rd of March 2001. A grid with 16 elements in horizontal and 32 elements in vertical direction was used, corresponding to a spatial resolution of 6.5 cm in horizontal and 3.7 cm in vertical direction. Hydraulic parameters for a loam and a silt were used to study the model's sensitivity. To analyze the numerical behavior, simulations with a reduced grid spacing, a different starting time, varied boundary conditions and a three-dimensional simulation have been performed. Simulations with changed parameters for the water vapor transport and with inclusion of solute transport have been conducted.

The fully coupled equation system for water, heat and vapor transport could be solved with the approach described in the last chapter. Variable substitution could be done in a definite way, i.e. repeated switching of the same variable in one time step did not occur, except when solute transport was included. Mass and energy balances were excellent.

Plots comparing measured and modeled values of temperature and the square root of relative permittivity at 24 probes for each of the different scenarios are shown in appendix E. The square root of the relative permittivity is used, because it is proportional to the measured travel time along the TDR rods and also to the liquid water content. The relative permittivity was calculated by the program with the mixing model described above. If an oversaturation of ice occurred, the volume fractions of soil matrix, ice, liquid water and air were normalized to one.

4.3.1 Homogeneous Simulations

Figures 4.13 and 4.14 show profiles of temperature and relative permittivity during freezing and thawing for different scenarios. Although the freezing curves are quite similar for the silt and the loam parameterization (Figure 4.10), the differences in simulation results are quite pronounced. Due to the higher permeability and the more gradual decrease of relative permeability with falling temperature, infiltration in the silt is much faster, leading also to a quicker warming of the soil toward 0 °C, but the infiltration leads also to a huge accumulation of ice in the lower part of the profile, as infiltrating water refreezes. The differences are still quite big, if the parameters of the soil water characteristic for the silt and the permeability of the loam are used (scenario 'silt with reduced permeability' in the appendix).

The simulation without freezing is not able to reproduce the behavior of the system. A detailed comparison of the time series at the probes shows, that there is a good agreement between temperatures between the unfrozen scenario and the measured values if the profile is completely frozen or completely thawed, but agreement during freeze and thaw is quite bad. The simulated permittivity is only acceptable when the profile is completely thawed. The very high permittivities in the lower part of the profile are not matched by the unfrozen scenario. This means they are not just a result of infiltrating snow melt water.

The agreement between the loam and silt scenarios and the measured values is qualitatively quite good. The buffering of the temperatures due to freezing, which leads to the "zero-curtain-effect", is clearly visible. The strong difference between permittivity in winter and summer is reproduced (although not the exact temporal behavior). This change is not a consequence of infiltrating water, since the maximal amount of water infiltrated in the loam scenario was below 45 mm (Figure 4.15). As some water left the profile over the lower boundary at the end of the first summer, when the profile was deeply thawed, the total water balance is even slightly negative (This is completely different for the silt, where a huge amount of water infiltrated the profile and left it again over the lower boundary). The difference between winter and summer is therefore a local phenomenon depending on the energy state of the soil and the material parameters. During thaw water is ponding on the still frozen regions in the loam scenario as well as in the measured data. This effect is completely absent in the unfrozen scenario. The comparison of the time series at the probes with the measured values shows that the thawing depth is not reproduced by both the silt and the loam scenario. Temperature at deeper positions remains therefore close to zero even in the summer. Both simulation and measured data show that the profile freezes from below as well as from above, but that freezing from above is dominant. As the simulated temperature is too low in the lower part of the profile, the simulated permittivity is much too low. In the silt this is partly compensated by infiltrating water, partly made worse by a huge accumulation of ice, which leads to a decrease in permittivity (as the liquid water content is lowered when saturations
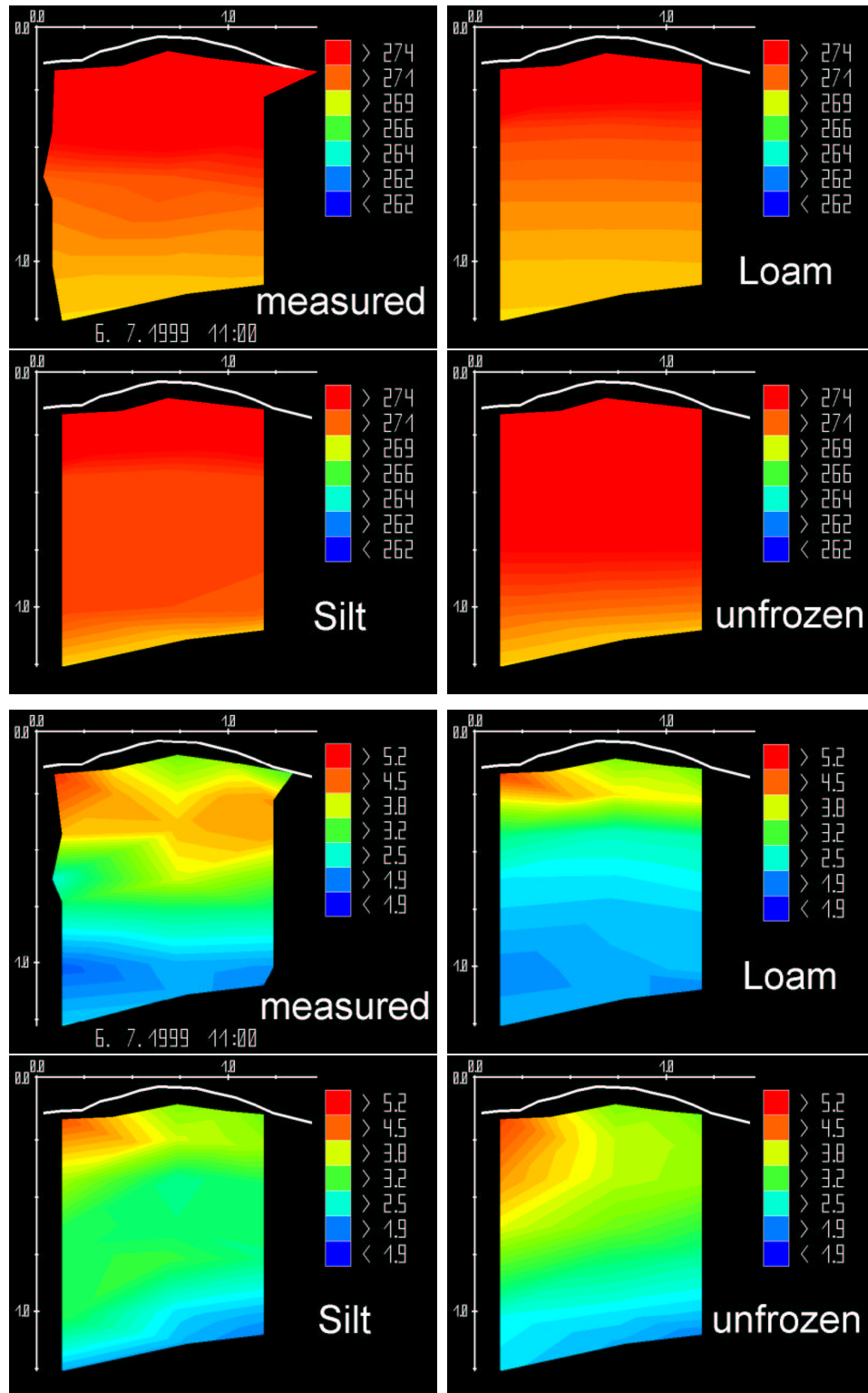
Figure 4.13: Profiles made from measured data and simulation results for the loam, silt and unfrozen scenario showing temperature (above) and relative permittivity (below) at July 6, 1999 during thawing
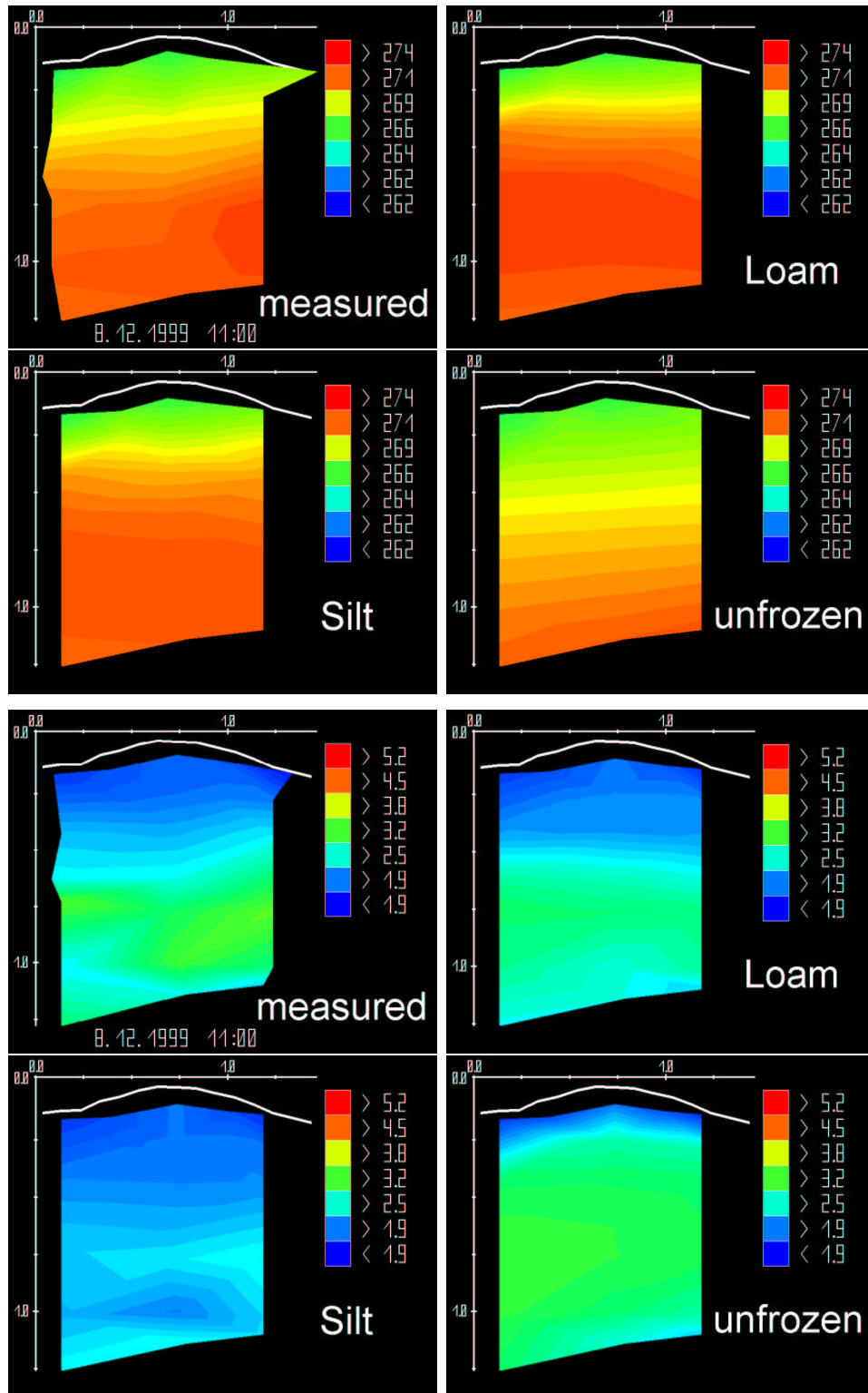
Figure 4.14: Profiles made from measured data and simulation results for the loam, silt and unfrozen scenario showing temperature (above) and relative permittivity (below) at December 8, 1999 during freezing
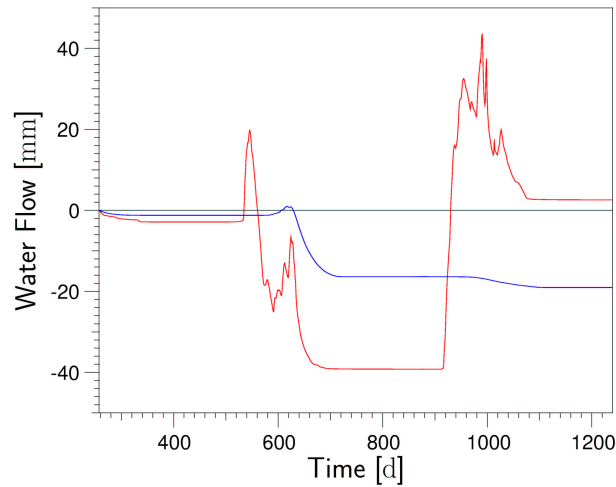
Figure 4.15: Simulated cumulative flow of water through the upper (red) and lower (blue) boundary in the loam scenario

are normalized). This is also the reason for the very low permittivity in the silt profile in figure 4.14. The calculated heat flux is similar for silt and loam and within reasonable bounds (Figure 4.16). The very quick rising of the permittivity during thawing can be reproduced and even outstripped by the silt scenario without any macropores.

4.3.1.1   Numerical Tests

The effect of initial condition, spatial resolution, boundary conditions and dimensionality on the result was checked with additional scenarios. For these simulations the hydraulic parameters for the loam were used. Doubling the spatial resolution yielded only marginally different results. When the simulation was started one year later at September 13, 1999, the temperatures remained nearly unchanged. The simulated permittivities in the summer 2000 were markedly higher in the lower part of the profile. This may be a consequence of a different total water content. At September 13, 1998 the profile was already partly frozen, whereas it was still thawed a year later. If the profile is frozen, the ice content is estimated from permittivity and used as initial condition. This is very unprecise and seems to lead to an overestimation in 1998. If there is less water in the profile it leads to the paradoxical effect that the permittivity will rise higher as thawing can reach deeper regions of the soil.

To analyze the effect of boundary conditions, one scenario was simulated, in which Dirichlet boundary conditions derived from measured data were used also at the side boundaries. If lateral flow would have been the reason for the deviation of measured and modeled values, this would be visible in this scenario, but fluxes were always directed either inward or outward on both side boundaries, indicating
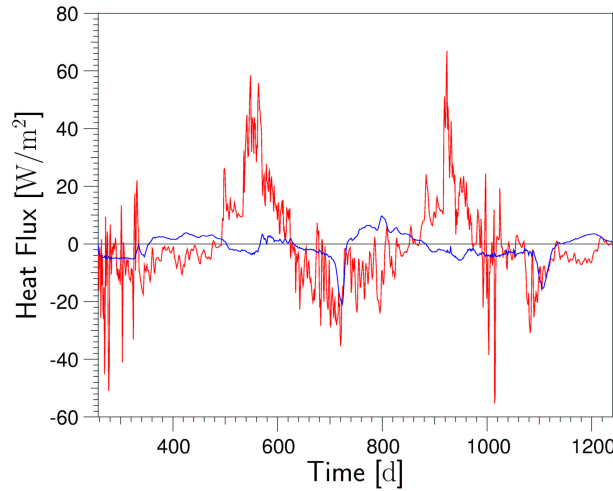
Figure 4.16: Simulated heat flux over the upper (red) and lower (blue) boundary in the loam scenario

a mismatch of the used material parameters.

To check the influence of the strong boundary conditions, a 2 m deep profile was simulated. Temperature at the lower boundary was kept constant at -4 °C and a no-flux boundary condition was used for water flow. As the lowest probes are already in permafrost, the same temperature was used as initial condition for the region below the lowest probes and it was assumed that the pore space is completely filled with ice. This simulation clearly shows too high temperatures in winter and too low temperatures in summer in the lower part of the profile, leading to quite small permittivities in the summer. The damping effect on temperature with depth is obviously too high.

The differences between two-dimensional and three-dimensional simulation are quite small. This is not really surprising. The real two-dimensional distribution of temperature and permittivity at the boundaries is not known and the method used to create the boundary conditions produces quite a smooth field. The no-flux boundaries at the sides also force a vertical dynamic, for which dimensionality is less important.

4.3.1.2   Relevance of Different Heat Transport Processes

Additionally to the normal loam scenario, in which water vapor diffusion was simulated like diffusion of a normal gas using the tortuosity formula 2.43, one scenario without any water vapor transport and one scenario with water vapor transport simulated according to the ideas of Philip and de Vries (1957) were computed. The simulated time series are not distinguishable, which means that water vapor transport is not an important heat transport process in the soil. This can also be
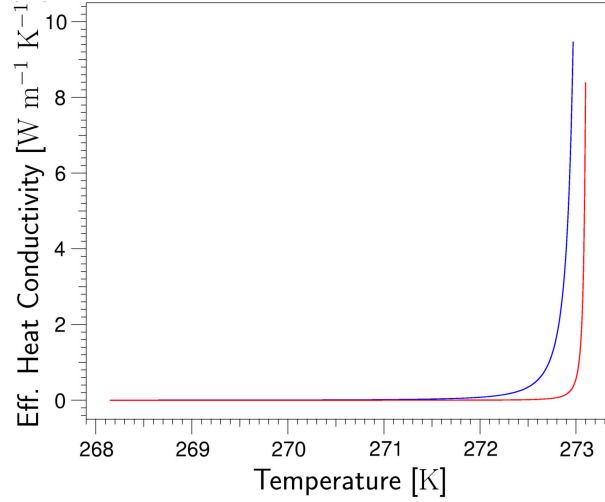
Figure 4.17: Effective heat transport due to liquid water flux for the loam (red) and the silt (blue)

demonstrated by the following estimation:

Water vapor diffusion is calculated from $D_g^w \nabla \nu_g^w$. The molar density of water vapor ν_g^w is a function of temperature and capillary pressure (Equation 2.56), which is also a function of temperature in frozen soils. The density gradient can be expressed as $\nabla \nu_g^w = \partial \nu_g^w / \partial T \cdot \nabla T$. For a given temperature gradient, the amount of water transported by water vapor can then be estimated. If $D_g^w \cdot \partial \nu_g^w / \partial T$ is multiplied with the latent heat of sublimation, the result is an effective heat conductivity. It decreases exponentially with temperature. At 0 °C the effective heat conductivity is 0.026 W/m K, which is nearly negligible compared to the heat conductivity of soil, which is approximately 2 W/m K. The diffusivity for mass flux due to a temperature gradient is $9.3 \cdot 10^{-9}$ kg/m s K.

A similar derivation can also be made for the transport of liquid water, for which the pressure gradient is also a function of temperature. The effective heat conductivity due to the transport of liquid water can then be calculated from

$$\lambda_{\text{eff}} = \Delta H_{il}^w \cdot \nu_l^w(T) \cdot K \cdot \frac{k_{r_l}(S_l(T))}{\mu_l(T)} \frac{\partial p_l}{\partial T}. \tag{4.6}$$

Figure 4.17 shows the result for the silt and the loam. If the temperature is near 0 °C, the effective heat conductivity can be quite large, which means that the transport of liquid water would be an important heat transfer process. Depending on the hydraulic parameters, this effective heat conductivity can drop quite rapidly, when temperature decreases. The importance of this process can also be seen in the model results. Figure 4.18 shows some state variables and fluxes calculated for the loam during thaw at July 6, 1999, the day for which the plots shown in figure 4.13 were made. Two zones of high conductive heat fluxes (red) can be seen, separated

Temperature	Water Pressure	Phase State	Water Flux	Water Flux

Ice Saturation	Water Saturation	Rel. Permittivity	Heat Flux	Heat Flux

295
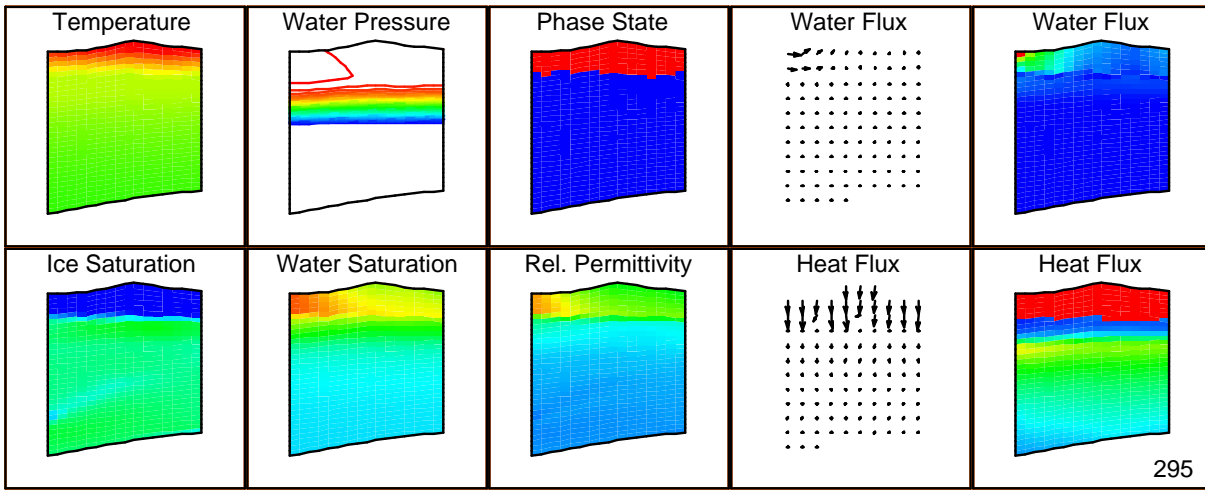
Figure 4.18: Profiles of temperature [262:278], ice saturation [0:2], liquid phase pressure $[-1{\cdot}10^{-6}{:}9{\cdot}10^{-4}]$, water saturation [0:1], phase state (blue=frozen), relative permittivity [3.6:27], water flux and heat flux at July 6, 1999. Values in brackets are the maximum and minimum values used in scaling

by a zone of nearly no heat flux. Below infiltrating water ponding on the still frozen zone, a small band with nearly no water flux can be seen and further below a second zone with higher water transport, which is identical to the zone of low heat fluxes. Analysis of the divergence of heat fluxes confirms that water melts at the thawing front, is transported downward in the liquid phase and refreezes releasing the heat. During freezing this effect is not so clearly visible, but liquid water transport contributes to the stabilization of the "zero curtain", by transporting energy to the freezing front.

4.3.1.3   Solute Transport

One scenario was calculated, which included solute transport. As only the bulk electrical conductivity of the soil was measured, no good estimates for boundary and initial conditions were available. The initial concentration was therefore assumed to be 1 mmole/l, which is a typical value for soils. If the soil was already initially frozen, the initial concentration was increased, so that the total amount of solutes corresponded to the total water content, as if solutes had been completely excluded from the ice phase at that spot. At the upper and lower boundary Dirichlet boundary conditions were calculated in the same way. When solute transport was included, problems with the variable substitution appeared. Switching loops occurred, where the state was switched from frozen to unfrozen and backward in the same time step. In this case the variable state was left unfrozen. After 372 days of simulation

the solver broke down. For the time simulated, the curves with and without solute transport were indistinguishable. This can be explained by calculation of the freezing point depression resulting from a solute concentration of 1 mmole/l, which is only 0.002 °C.

4.4   Heterogeneous Simulation

In all simulations, the thaw depth was too shallow and the permittivity and temperature were too low in the lower part of the profile. This can be explained by the soil's heterogeneity. The soil has an appreciable stone content with a stone layer in 50 cm depth. This leads not only to an increased heat conductivity, but also to a smaller amount of water in the profile and less buffering of energy. In a first approximation this can be taken into account by lowering the porosity and the permeability proportional to the stone content. As porosity and saturation were separated in the parameterizations of water characteristic and relative permeabilities, this was a fast way of estimating the influence of stone content. A stone content of 10 percent in the whole profile and of 50 percent in a 20 cm thick band slightly falling from left to right was used. As the stones were rather large and the TDR probes are inserted in stone free material, the porosity was not reduced in the calculation of permittivity. Simulation results show an increased thawing depth and a much higher permittivity in summer in the lower part of the profile. This effect would be even larger in reality, as the large stones have a higher effect on heat conductivity and permeability, which would possibly lead to an ice accumulation in the stone band and a further increased heat conductivity.

4.5   Discussion

The model works and is capable of solving the fully coupled equation system for freezing soils. The major phenomena seen in the measured data and in other studies are reproduced. This includes the "zero-curtain", ponding of water on the frozen soil and the strong difference between permittivity in winter and summer. The quantitative correspondence of measured and modeled data is not too good. The thawing depth is underestimated. The strong heterogeneity of the profile with variation in texture as well as in stone content seems to be responsible for this deviation, as simulation results depended very strongly on the hydraulic parameters used. Including the stone content even in a rather crude way led to a change in the right direction. Water vapor transport and solute transport are not relevant for the heat and water dynamics of the soil, but the transport of latent heat with liquid water is an important heat transfer process near the freezing point. In the scenario without freezing, agreement between simulated and measured temperatures was quite good

in times when the profile was completely thawed or completely frozen, and in very cold times also for nearly all other scenarios. Heat transport seems to be purely conductive during these periods. Mechanical interactions might be important, but no phenomena have been observed which could only be explained by inclusion of mechanic. Even the fast infiltration in the spring can be explained by matrix conductivity alone. No density driven convection was observed in the simulations.

5 Application: Multiphase Transport

Especially close to liquid phase saturation, water and gas transport are strongly coupled in a porous medium. Research is often concentrated on either liquid or gas phase transport and not on the interactions between both. In this chapter single and multiphase simulations of multistep outflow experiments are compared and the differences are analyzed.

5.1 Multistep Outflow Experiments

Soil hydraulic parameters are difficult to measure. Direct methods are tedious and time consuming. Multistep outflow experiments are a widely used alternative. A soil core is placed on a ceramic plate and saturated with water. The pressure at the lower boundary is then lowered either continuously or, in steps. At some lower limit, the procedure is reversed and the soil sample is saturated again. The liquid phase pressure at one or more positions in the sample is measured with tensiometers, the water content in the sample is also periodically measured with TDR. The volume of water emanating from the soil column is recorded with high temporal resolution. A parameterization of soil water characteristic and hydraulic conductivity function is fitted to the measured values by inversion of Richards' equation (Zachmann et al. 1982, Hornung and Messing 1982, Zurmühl 1994, Schultze 1998). The parameterization is crucial for the result of the optimization. The van Genuchten parameterization is used most frequently, and spline approximations have also been applied (Chavent et al. 1980, Durner et al. 2001). An entry pressure as included in the Brooks-Corey parameterization is rarely considered. Multiphase models usually are not used in this inversion process.

The effect of the model used in the forward simulation (singlephase/multiphase, van Genuchten/Brooks-Corey parameterization) on the result is analyzed in the following section and compared qualitatively with the result of laboratory measurements with an artificial porous medium.
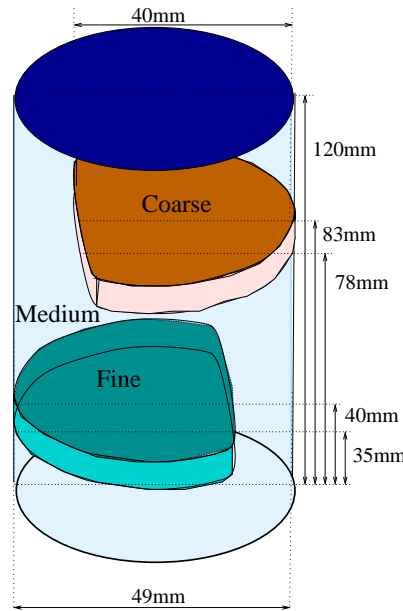
Figure 5.1: Heterogeneous test column composed of sintered glass with fine, medium and coarse pores (Graf et al. 2001)

5.2   Laboratory Experiments

Columns made of sintered glass were proposed by Graf et al. (2001) as a static porous material, which is similar to natural porous media. The columns are available with different pore sizes. Homogeneous columns in the three pore size classes fine (10-16 μm), medium (40-100 μm), coarse (250-500 μm) and a heterogeneous column were (Figure 5.1) studied.

5.3   Model Parameters

5.3.1   Transport Parameters

Multistep outflow experiments with the different columns were simulated. The transport parameters used for the simulations were estimated by H. Graf from a multistep outflow experiment with the homogeneous column with coarse pores using an inverse model based on Richards' equation.

The parameters of the soil water characteristic were transferred to the medium and fine soil using the assumption of Miller similarity. The concept of Miller similarity (Miller and Miller 1956) implies that at a different location the geometry of the pore space is exactly the same and only the size of the elements which compose the pore space is different. If we can associate a scaling parameter with a typical scale

of the pore space (e.g. average or maximal pore diameter), the hydraulic parameters measured at a certain scale χ^* can be used at a different scale χ, if capillary pressure and permeability are scaled by the relation:

$$S_l(\psi_l) = S_l^* \left(\frac{\psi_l \cdot \chi}{\chi^*} \right) \tag{5.1}$$

$$K = K^* \cdot \left[\frac{\chi}{\chi^*} \right]^2 \tag{5.2}$$

By definition, porosity is constant in Miller similar media. Scaling parameters of 0.2 and 0.032 have been used for the medium and the fine material respectively corresponding to maximal pore sizes of 500μm, 100μm and 16μ m for the coarse, medium and fine material. The resulting water characteristics are shown in figure 5.2.

As the estimation error for the permeability of the coarse medium was huge, permeabilities were not taken from the Miller scaling, but derived from measured saturated hydraulic conductivity. Values of $6.5 \cdot 10^{-13}$ m^2 for the fine, and $3.3 \cdot 10^{-12}$ m^2 for the medium material were used. The measured saturated hydraulic conductivity for the coarse medium seemed too large, therefore a permeability of 10^{-11} m^2 was assumed. Equivalent Brooks-Corey parameters were derived from the van Genuchten parameters by $\psi_{entry} = \alpha^{-1}$ and $\lambda = mn$. The parameters for the coarse material are shown in table 5.1. For the diffusion of air in water a diffusion coefficient of $2 \cdot 10^{-9}$ m^2/s was used.

It was assumed, that a ceramic plate with a thickness of 1 cm, an entry pressure of 2 m and the permeability of the medium material was at the lower end of the column. Brooks-Corey parameters were always used for the ceramic plate, to prevent the development of a gas phase. The choice of the parameter lambda is arbitrary for this material, as it remains always saturated.

5.3.2 Initial and Boundary Conditions

At the upper boundary a no-flux boundary condition was used for water, and the air pressure was kept constant at standard pressure. A typical multistep outflow scheme was applied at the lower boundary. As the underpressure is generated by a vacuum pump, the same pressure was used for air and water. No-flux boundary conditions were used at the sides. Initially the column was fully water saturated and it was assumed that the dissolved air was in equilibrium with the atmosphere.

5.4 Simulation Results

A multistep outflow experiment with a duration of 22 hours was simulated for the heterogeneous column and homogeneous columns composed of coarse, medium and
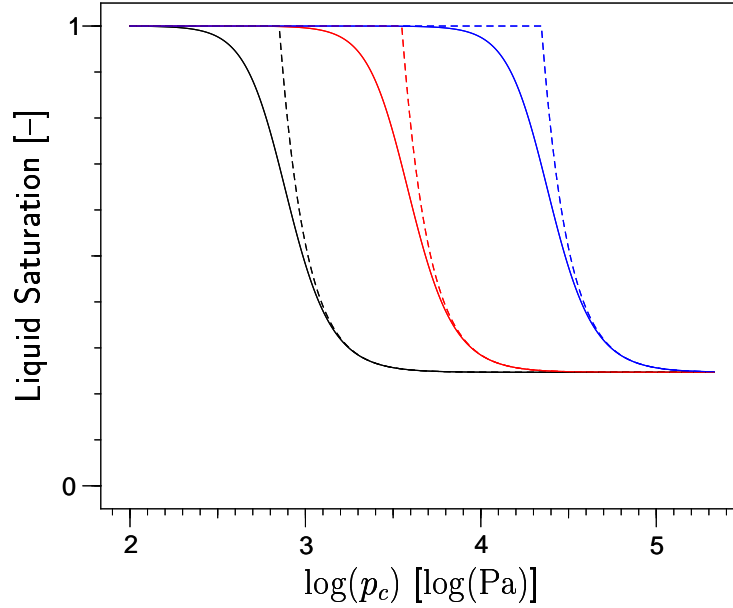
Figure 5.2: Soil water characteristic for the coarse (black), medium (red) and fine (blue) material using the van Genuchten (solid line) and Brooks-Corey (dashed line) parameterization

fine material. For each material the outflow of water was computed using either the van Genuchten or Brooks-Corey parameterization in combination with either the Richards' equation, or a twophase model, based on the phase pressure/partial pressure formulation. A two-dimensional grid with 48 elements in vertical and 16 elements in horizontal direction was used, corresponding to a horizontal resolution of 0.25 cm and 0.31 cm in vertical direction. As the derivative of the Brooks-Corey parameterization is not continuous, convergence problems occurred with the Newton method when the Brooks-Corey parameterization was used in combination with the twophase model. It was, however, possible to demonstrate the usefulness of the new phase pressure/partial pressure formulation.

5.4.1 Homogeneous Medium

No outflow occurred from homogeneous columns of fine material in the simulations using the Brooks-Corey parameterization with both Richards' equation and the twophase model, a small outflow was calculated with the van Genuchten parameterization. For the coarse and the fine material, identical outflow curves were obtained with both Richards' equation and the twophase model with the Brooks-Corey and the van Genuchten parameterization. The simulated outflow curves for the medium material are shown in figures 5.3 and 5.4 together with the pressure applied at the lower boundary. Apart from minute differences in the first drainage and the last

Table 5.1: Van Genuchten and Brooks-Corey Parameters for the coarse material

parameter	value	unit
Φ	0.45	–
α	13.82	m^{-1}
n	3.8789	–
m	$1 - \frac{1}{n}$	–
λ	2.8789	–
p_e	708.6	Pa
S_{r_l}	0.247	–
S_{r_l}	0.0	–
τ	2.0	–

imbibation step, the outflow computed with the van Genuchten parameterization was identical. When the Brooks-Corey parameterization was used the results of the Richards' equation model and the twophase model showed marked differences. Drainage calculated by the multiphase model was slower in the first pressure steps and hysteresis occurred during imbibation. This is in excellent agreement with observations made in the experiments. When gas phase continuity was reached, the results obtained with Richards equation and the twophase model were identical for all simulations.

5.4.2   Heterogeneous Medium

The lower boundary condition and the outflow computed for the heterogeneous soil column for the first drainage steps is shown in figures 5.5 and 5.6. In both simulations using the van Genuchten parameterization and in the simulation with Richards' equation and the Brooks-Corey parameterization, the lens of coarse material is nearly completely drained in the first pressure step. In the twophase simulation with the Brooks-Corey parameterization, only a minute amount of water emanates from the column when an air phase forms in the coarse medium from dissolved air. After 5 hours, the material above the coarse lens is drained, as the entry pressure of the medium material is reached. As soon as the coarse lens is connected to the gas phase, it is completely emptied. Unfortunately convergence problems of the Newton solver led to a simulation breakdown after 6.5 hours simulated time for the twophase simulation with Brooks-Corey parameters. Figure 5.8 shows the water and gas pressure, saturations and fluxes calculated by the model after 5 and 6 hours simulated time. In the plot made at 5 hours simulated time, a gas phase can be seen in the coarse lens, which emerged from dissolved air and led to a corresponding pressure drop in the gas phase. The medium material starts to drain at the upper boundary.
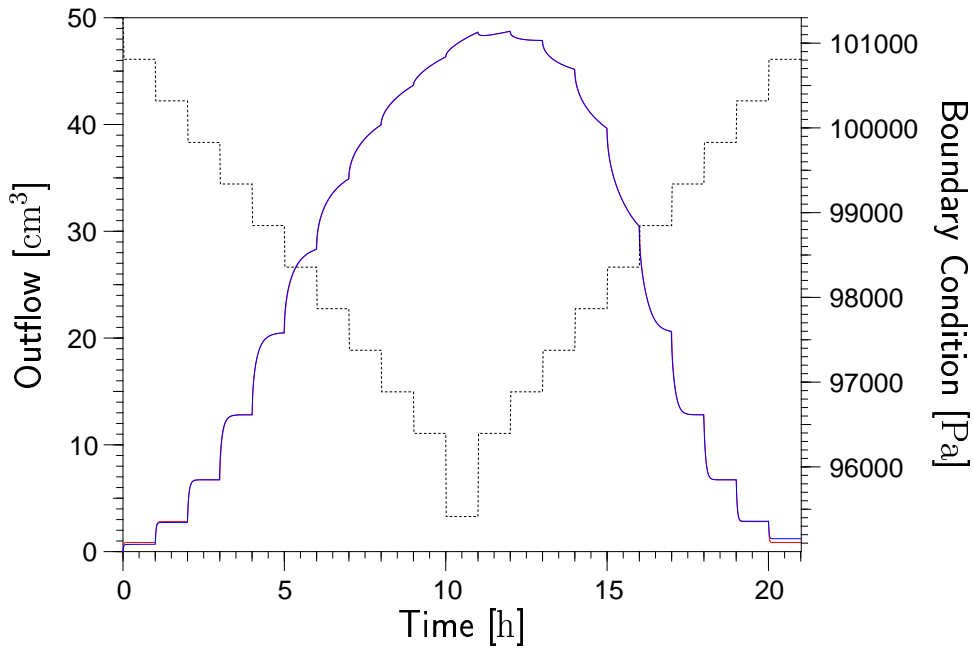
Figure 5.3: Outflow of water calculated with Richards' equation (red) and the twophase model (blue) obtained with the van Genuchten parameterization for the homogeneous column made of medium material and lower boundary condition (black dashed)
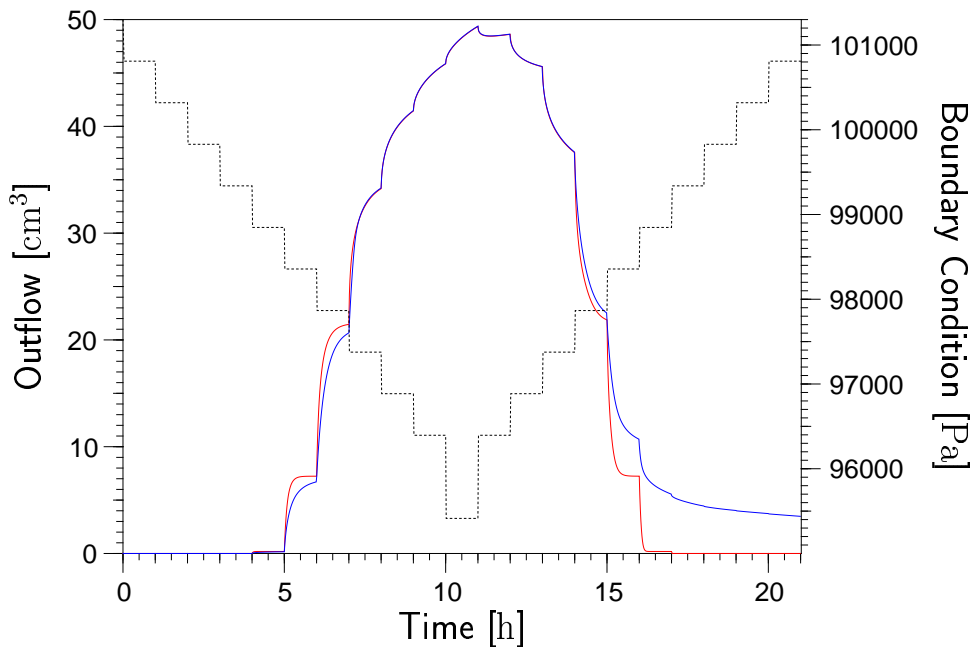
Figure 5.4: Outflow of water calculated with Richards' equation (red) and the twophase model (blue) obtained with the Brooks-Corey parameterization for the homogeneous column made of medium material and lower boundary condition (black dashed)
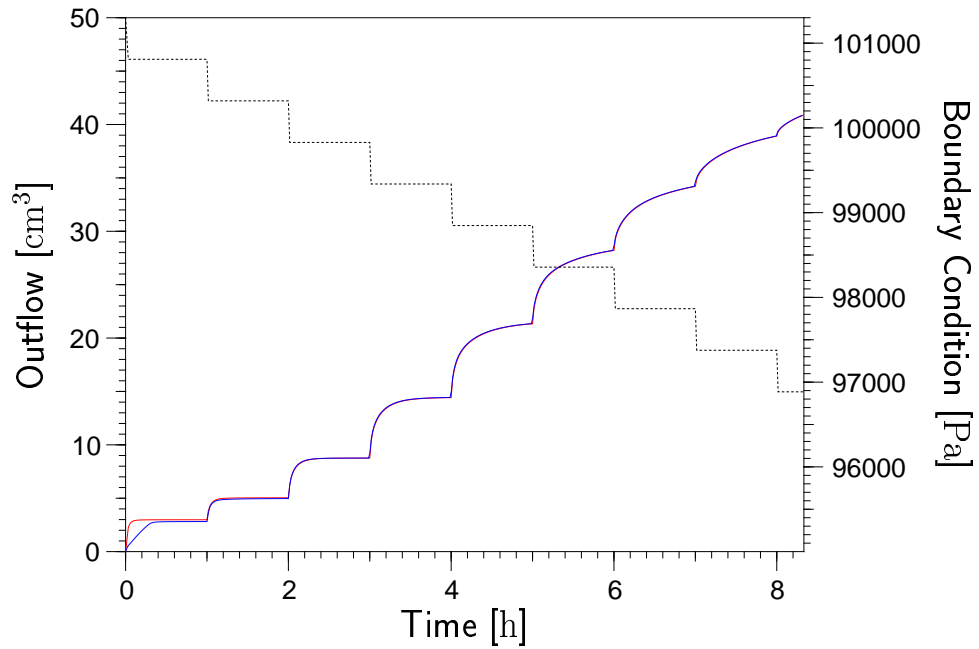
Figure 5.5: Outflow of water calculated with Richards' equation (red) and the twophase model (blue) obtained with the van Genuchten parameterization for the heterogeneous column and lower boundary condition (black dashed)
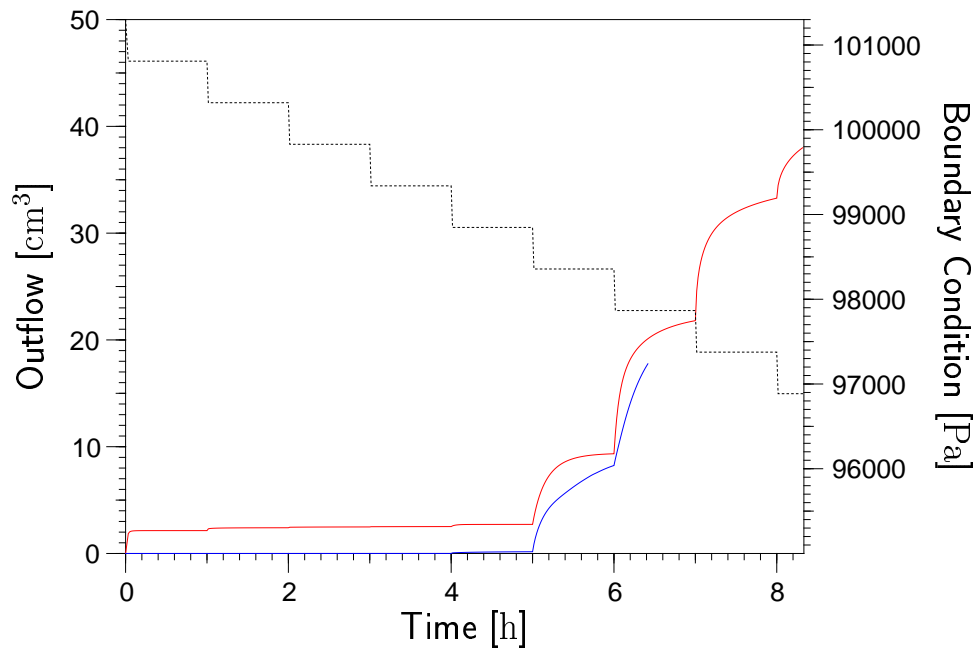
Figure 5.6: Outflow of water calculated with Richards' equation (red) and the twophase model (blue) obtained with the Brooks-Corey parameterization for the heterogeneous column and lower boundary condition (black dashed)

The gas saturation is still very low. After 6 hours, drainage has reached the coarse lens. The gas phase pressure is again at atmospheric pressure. Below the coarse lens, water originating from the coarse lens can be seen. It is not in contact with a continuous gas phase and the partial pressure of air is still lower. Liquid phase conductivity is now very low in the dry coarse lens and final drainage is efficiently obstructed, resulting in an increased liquid phase pressure in the coarse lens. Water in the medium material is ponding on the coarse lens.

5.5 Discussion

Richards' equation and the twophase model deliver identical results if the gas phase is continuous. When the van Genuchten parameterization was used, the results obtained for water flow with the twophase model and Richards' equation were hardly distinguishable for all saturations.

Characteristic differences occurred between the Richards' equation and the twophase model if Brooks-Corey parameterization was used. At high water saturations, the water flux out of the column was slower and hysteresis was visible during imbibation. These observations are in agreement with measurements. They can be explained by two factors: the existence of an air entry pressure, resulting from the limited maximal pore diameter, and the difference in permeabilities between the two parameterizations. As gas is transported primarily in the largest pores and the maximal pore size is not limited in the van Genuchten parameterization, the relative permeability for the gas phase is always higher and the relative permeability for the liquid phase is always lower at a given saturation than in the Brooks-Corey parameterization (Figure 5.9).

The new phase pressure/partial pressure formulation makes solution of a twophase model in combination with the Brooks-Corey parameterization possible. It therefore gives a better description of the measurements. The Newton method, however, is not optimal for the solution of the resulting nonlinear and discontinuous equation system.
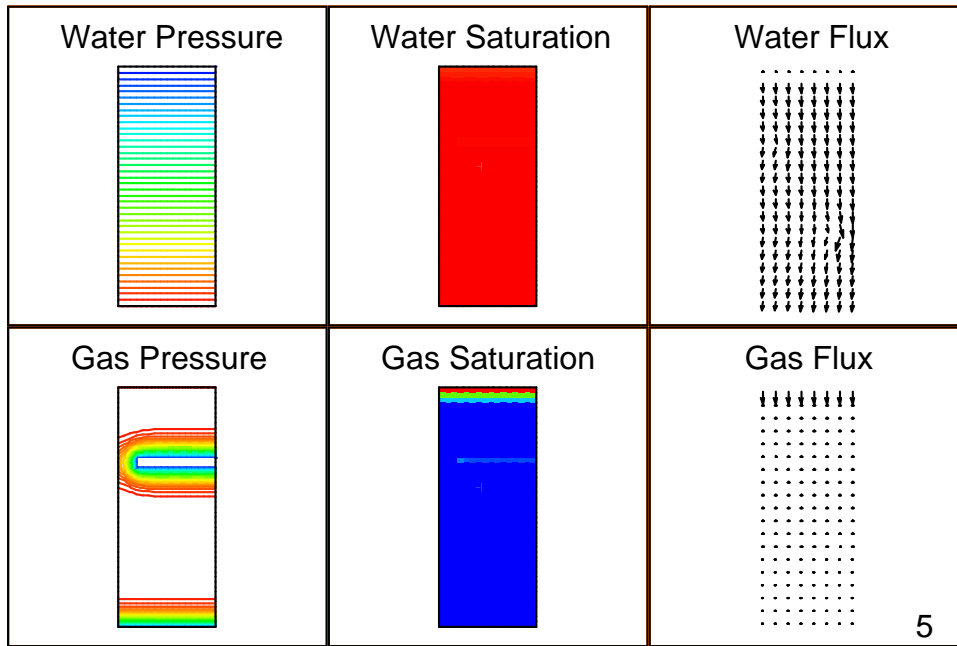
Figure 5.7: Distribution of liquid phase pressure [97'700:98'800], gas pressure [98'700:101'000], water saturation [0:1], gas saturation [0:0.04] and fluxes in the heterogeneous column after 5 hours. Values in brackets are the maximum and minimum value used in scaling
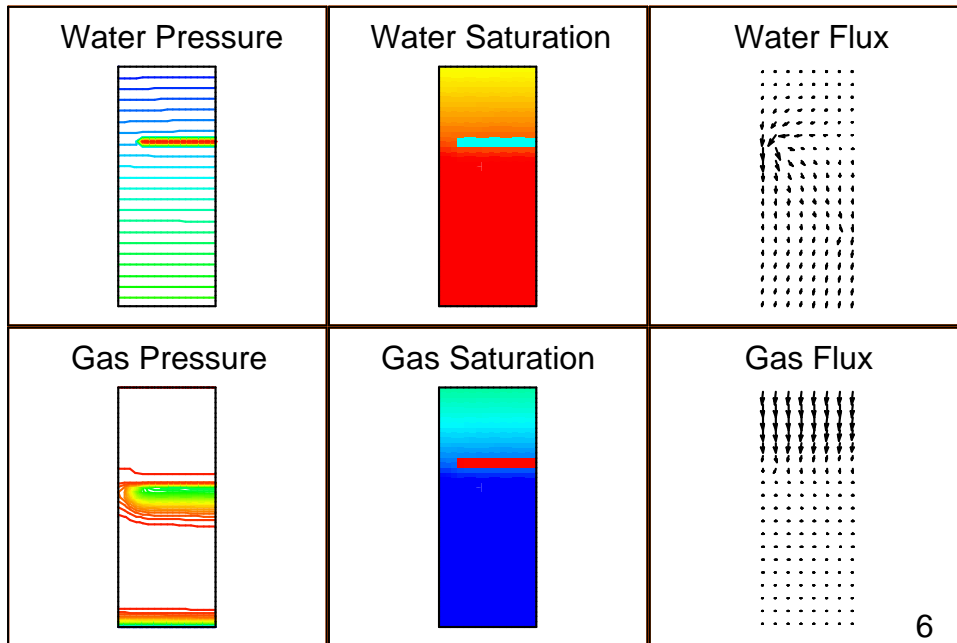
Figure 5.8: Distribution of liquid phase pressure [97'200:99'300], gas pressure [98'400:101'000], water saturation [0:1], gas saturation [0:0.74] and fluxes in the heterogeneous column after 6 hours. Values in brackets are the maximum and minimum value used in scaling
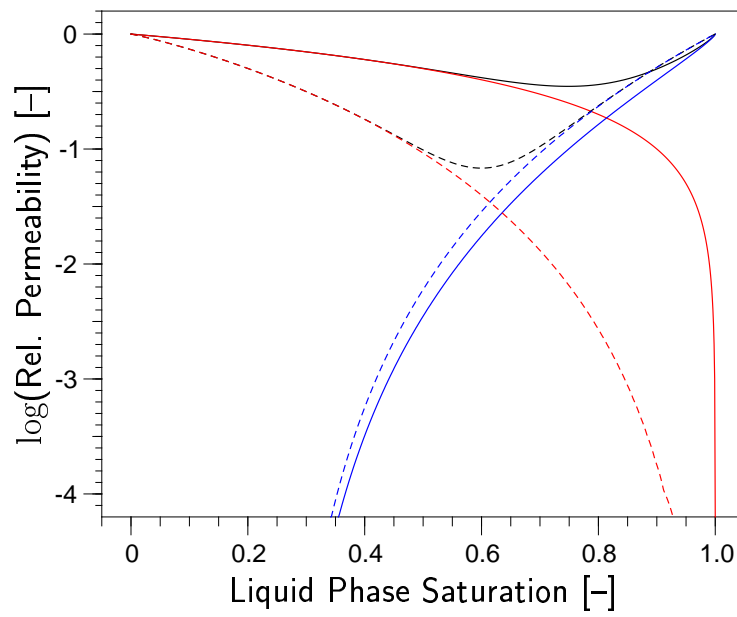
Figure 5.9: Relative permeabilities obtained with the van Genuchten (solid lines) and Brooks-Corey parameterization (dashed lines) for gas phase (red), liquid phase (blue) and sum of both (black) for the medium material

6 Conclusions

Coupled transport of water, air, solutes and heat in porous media was studied in this work. An equation system with appropriate parameter functions has been formulated. A computer model based on this equation system was developed with special emphasize on robustness, consistency, stability and flexibility in the choice of processes taken into account in the modeling. The model was tested successfully and was applied to a permafrost soil and to multiphase transport. The model proved to be a valuable tool for the study of process coupling.

Comparison between model results and data measured at a permafrost site near Ny Ålesund showed a good qualitative agreement. The main features of the water and energy dynamic were reproduced. However, small differences in the water transport parameters lead to large differences in the modeled results. Unlike transport of liquid water during freezing and thawing, water vapor transport proved to be unimportant. Inclusion of solute transport had no effect on the simulation result. The rapid infiltration in spring could be reproduced without macropores. The deviations between measured and modeled temperatures and relative permittivities are most probably a result of the heterogeneity of the profile combined with the sensitivity of the system. Even a rather simplistic consideration of the stone content in the profile led to an improvement in correspondence. A simulation with a more detailed consideration of the heterogeneity would be desirable.

The coupling of atmosphere and soil was not treated in this work, as it is complicated by the dynamic of the snow cover. It should be taken into account in a future version of the model. No clear phenomena were detected in the measured data which could only be explained by mechanical processes. Yet the pseudo-mechanical model used to overcome the numerical difficulties is not satisfactory and the integration of a mechanical model would be of great importance for the understanding of the system behavior.

A new phase pressure/partial pressure formulation for the solution of coupled liquid and gas phase transport was developed. It was used to simulate multiphase outflow experiments. Results of the twophase model and a model based on Richards' equation combined with either the van Genuchten or the Brooks-Corey parameterization of the soil water characteristic were compared. The new formulation made the Brooks-Corey parameterization available for multiphase formulation without regularization. Richards' equation was equivalent to the twophase model as soon

as the gas phase became continuous. Even close to water saturation only minute differences could be observed between Richards equation and the multiphase model when the van Genuchten parameterization was used. In contrast, marked differences could be observed with the Brooks-Corey parameterization. The retarded drainage of water and the hysteresis between drainage and imbibation are in agreement with experimental results.

The Newton method was not stable and robust in the solution of the nonlinear equations describing twophase transport in heterogeneous systems when the Brooks-Corey parameterization was used. A better nonlinear solution method is necessary.

Bibliography

Anisimov, O., and F. Nelson. 1996. Permafrost distribution in the northern hemisphere under scenarios of climatic change. Glob. Planet. Change 14:59–72.

Anisimov, O., and F. Nelson. 1997. Permafrost zonation and climate change: results from transient general circulation models. Clim. Change 35:241–258.

Anisimov, O., N. Shiklomanov, and F. Nelson. 1997. Effects of global warming on permafrost and active-layer thickness: results from transient general circulation models. Glob. Planet. Change 61:61–77.

Atkins, P. W. 1990. Physikalische Chemie. 1. Auflage. VCH Verlagsgesellschaft mbH.

Baehr, A. L., and R. J. Baker. 1995. Use of a reactive gas transport model to determine rates of hydrocarbon biodegradation in unsaturated porous media. Water Resour. Res. 31:2877–2882.

Bastian, P. 1999. Numerical Computation of Multiphase Flows in Porous Media. Habilitationsschrift. Christian-Ablrechts-Universität, Kiel.

Bastian, P., K. Birken, S. Lang, K. Johannsen, N. Neuß, H. Rentz-Reichert, and C. Wieners. 1997. UG: A flexible software toolbox for solving partial differential equations. Computing and Visualization in Science 1:27–40.

Bear, J. 1972. Dynamics of Fluids in Porous Media. Elsevier, New York.

Bear, J., and Y. Bachmat. 1991. Introduction to Modeling of Transport Phenomena in Porous Media. Kluwer Academic Publishers.

Blom, T. J. M., and S. R. Troelstra. 1972. A simulation model of the combined transport of water and heat produced by a thermal gradient in porous media. Report 6. Dept. of Theoretical Production Ecology, Agricultural University Wageningen.

Boike, J., K. Roth, and O. Ippisch. 2001. Seasonal snow cover on frozen ground: Energy balance calculations of a permafrost site near Ny-Ålesund, Svalbard. submitted toJ. Geophys. Res.

81

Boike, J., K. Roth, and P. P. Overduin. 1998. Thermal and hydrologic dynamics of the active layer at a continuous permafrost site (Taymyr Peninsula, Siberia). Water Resour. Res. 34:355–363.

Brooks, R. H., and A. T. Corey. 1966. Properties of porous media affecting fluid flow. J. Irrigation and Drainage Div., Proc. Am. Soc. Civil Eng. (IR2) 92:61–88.

Buckingham, E. 1907. Studies on the movement of soil moisture. Bulletin 38. U.S. Department of Agriculture, Bureau of Soils. Washington, DC.

Chavent, G., G. Cohen, and M. Espy. 1980. Determination of relative permeabilities and capillary pressures by an automatic adjustment method. Paper SPE 9237 presented at the 1980 SPE Annual Technical Conference and Exhibition, Dallas, Sept. 21-24.

Cunningham, R. E., and R. J. J. Williams. 1980. Diffusion in Gases and Porous Media. Plenum Press, New York.

Darcy, H. 1856. Les Fontaines de la Ville de Dijon. Dalmont, Paris.

de Vries, D. A. 1952. The thermal conductivity of granular materials. Annexe Bul. Inst. Intern. du Froid. 1992:115–131.

de Vries, D. A. 1958. Simulataneous transfer of heat and moisture in porous media. Trans. Amer. Geophys. Union 39:909–916.

de Vries, D. A. 1963. Thermal properties of soils. p. 210–235. *In* W. R. van Wijk (ed.) Physics of Plant Environment. North Holland, Amsterdam.

Döll, P. 1996. Modeling of moisture movement under the influence of temperature gradients: Desiccation of mineral liners below landfills. Bodenökologie und Bodengenese, Heft 20, Fachgebiet Bodenkunde, TU Berlin.

Durner, W., S. Bitterlich, and P. Knabner. 2001. Bestimmung parameterfreier bodenhydrologischer Eigenschaften aus instationären Fließexperimenten durch inverse Simulation. Mitteilungen Deutsche Bodenkundliche Gesellschaft.

Dury, O., U. Fischer, and R. Schulin. 1999. A comparison of relative nonwetting-phase permeability models. Water Resour. Res. 35:1481–1493.

Einstein, A., and L. Infeld. 1966. The Evolution of Physics. Simon & Schuster Books.

Encyclopaedia Britannica 2001. Online ressource: http://www.britannica.com.

Findikakis, A. N., and J. O. Leckie. 1979. Numerical simulation of gas flow in sanitary landfills. Journal of the Environmental Engineering Division 105:927–945.

Flerchinger, G. N., and K. E. Saxton. 1989. Simultaneous heat and water model of a freezing snow-residue-soil system I. Theory and development. Trans. ASAE 32:565–571.

Fowler, A. C., and W. B. Krantz. 1994. Generalized secondary frost heave model. SIAM J. Appl. Math. 54:1650–1675.

Freijer, J. I., and P. A. Leffelaar. 1996. Adapted Fick's law applied to soil respiration. Water Resour. Res. 32:791–800.

Goulden, M., S. Wofsy, J. Harden, S. Trumbore, P. Crill, S. Gower, T. Fries, B. Daube, S. Fan, D. Sutton, A. Bazzaz, and J. Munger. 1998. Sensitivity of boreal forest carbon balance to soil thaw. Science 279:214–217.

Graf, H., V. Schulz, H. J. Vogel, and K. Roth. 2001. Experimenteller Ansatz zur Untersuchung von Mehrphasenfluss in porösen Medien. Mitteilungen Deutsche Bodenkundliche Gesellschaft.

Hare, D. E., and C. M. Sorensen. 1987. The density of supercooled water. II. Bulk samples cooled to the homogeneous nucleation limit. J. Chem. Phys. 87:4840–4845.

Haverkamp, R., M. Vauclin, J. Touma, P. J. Wierenga, and G. Vachaud. 1977. A comparison of numerical simulation models for one-dimensional infiltration. Soil Sci. Soc. Am. J. 41:285– 294.

Heimovaara, T. J. 1993. Time domain reflectometry in soil science: Theoretical backgrounds, measurements and models. PhD thesis. Unisersiteit van Amsterdam.

Helmig, R. 1997. Multiphase Flow and Transport Processes in the Subsurface - A Contribution to the Modeling of Hydrosystems. Springer-Verlag.

Hinkel, K. M., and S. I. Outcalt. 1993. Detection of nonconductive heat transport in soils using spectral analysis. Water Resour. Res. 29:1017–1023.

Hinkel, K. M., and S. I. Outcalt. 1994. Identification of heat-transfer processes during soil cooling, freezing, and thaw in central alaska. Permafrost and Periglacial Processes 5:217–235.

Hornung, U., and W. Messing. 1982. Identification of soil parameters from an input-output experiment. *In* P. Deuflhard, and E. Hairer. (ed.) Workshop on Numerical Treatment of Inverse Problems in Differential and Integral Equations. Birkhauser. Boston. p. 227–237.

Huwe, B. 1992. WHNSIM Version 2 - Ein Modell zur Simulation des Wasser-, Wärme- und Stickstoffhaushalts von Standorten mit unterschiedlicher Nutzung. Abteilung Bodenphysik. Bayreuth.

Ippisch, O., I. Cousin, and K. Roth. 1998. Wärmeleitung in porösen Medien - Auswirkungen der Bodenstruktur auf Wärmeleitung und Temperaturverteilung. Mitt. Dtsch. Bodenkundl. Ges. 87:405–408.

Jansson, P.-E. 1998. Simulation Model for Soil Water and Heat Conditions - Description of the SOIL model. Department of Soil Sciences. Uppsala, Sweden.

Jasper, J. J. 1972. The surface tension of pure liquid compounds. J. Phys. Chem. Ref. Data 1:841–1009.

Jin, Y., and W. A. Jury. 1996. Characterizing the dependence of gas diffusion coefficient on soil properties. Soil Sci. Soc. Am. J. 60:66–71.

Kane, D. L., R. E. Gieck, and L. D. Hinzman. 1990. Evapotranspiration from a small alaskan arctic watersheed. Nordic Hydrol. 21:253–272.

Kersten, M. S. 1949. Thermal properties of soils. Eng. Exp. Sation, Bull. 28. Inst. of Technology. Univ. Minnesota.

Krantz, W. 1990. Self-organization as patterned ground in recurrently frozen soils. Earth Science Revies 29:117–130.

Kuchling, H. 1991. Taschenbuch der Physik. 13. Auflage. Thun, Frankfurt/Main.

Kutilek, M., and D. R. Nielsen. 1994. Soil Hydrology. Catena-Verlag, Cremlingen-Destedt.

Li, N., B. Chen, F. Chen, and X. Xu. 2000. The coupled heat-moisture-mechanic model of the frozen soil. Cold Regions Science and Technology 31:199–205.

Liestøl, O. 1977. Pingos, springs and permafrost in Spitsbergen. Årbok 1975. Norsk Polarinstitutt.

Lindgren, M., and A. Rasmuson. 1994. Evaluation of water and gas transport in layered soil covers for coal ash deposits: 2D-calculations and impact of a weak zone. Water, Air, and Soil Pollut. 77:97–114.

Mason, E. A., A. P. Malinauskas, and R. B. Evans III. 1967. Flow and diffusion of gases in porous media. J. Chem. Phys. 46:3199–3216.

Miller, E. E., and R. D. Miller. 1956. Physical theory for capillary flow phenomena. J. Appl. Phys. 27:324–332.

Miller, R. D. 1980. Freezing phenomena in soils. p. 254–299. *In* D. Hillel (ed.) Applications of Soil Physics. Academic Press, New York.

Moore, W. J. 1990. Physical Chemistry. Fifth edition. Longman Scientific & Technical.

Mualem, Y. 1976. A new model for predicting the hydraulic conductivity of unsaturated porous media. Water Resour. Res. 12:593–622.

Nakano, Y., and J. Brown. 1972. Mathematical modeling and validation of the thermal regimes in tundra soils, barrow, alaska. Arctic and Alpine Research 4:19–38.

National Research Council of Canada 1988. Glossary of permafrost and related ground ice terms. Technical Memorandum 142. Permafrost Subcommittee, Associate Committee on Geotechnical Research, National Research Council of Canada (NRCC 27952). Ottawa, Ontario.

O' Neill, K., and R. D. Miller. 1982. Numerical solutions for a rigid-ice model of secondary frost heave. CRREL Report 82-13. Cold Regions Research & Engineering Laboratory.

Ott, J. 1996. Parameter des Gastransports in natürlichen und künstlichen Böden. Diplomarbeit. Universität Bayreuth.

Padilla, F., and J.-P. Villeneuve. 1992. Modeling and experimental studies of frost heave including solute effects. Cold Regions Science and Technology 20:183–194.

Peaceman, D. W. 1977. Fundamentals of Numerical Reservoir Simulation. Elsevier.

Philip, J. R., and D. A. de Vries. 1957. Moisture movement in porous materials under temperature gradients. Trans. Amer. Geophys. Union 38:222–232.

Putkonen, J. 1998. Soil thermal properties and heat transfer processes near Ny-Ålesund, northwestern Spitsbergen, Svalbard. Pol. Res. 17:165–179.

Ray, R. J., W. B. Krantz, T. N. Caine, and R. D. Gunn. 1983. A model for sorted patterned-ground regularity. J. Glaciol. 29:317–337.

Richards, L. A. 1931. Capillary conduction of liquids through porous mediums. Physics 1:318–333.

Romanovsky, V. E., and T. E. Osterkamp. 2000. Effects of unfrozen water on heat and mass transport processes in the active layer and permafrost. Permafrost and Periglacial Processes 11:219–239.

Roth, K. 1996. Lecture Notes in Soil Physics. Institute of Soil Science, University of Hohenheim, D-70593 Stuttgart.

Roth, K., and J. Boike. 2001. Quantifying the thermal dynamics of a permafrost site near Ny-Ålesund, Svalbard. accepted byWater Resour. Res.

Roth, K., R. Schulin, H. Flühler, and W. Attinger. 1990. Calibration of time domain reflectometry for water content measurement using a composite dielectric approach. Water Resour. Res. 26:2267–2273.

Schultze, B. 1998. Optimierung der Messung bodenhydraulischer Eigenschaften durch inverse Simulation von Ausfluß- und Rückflußexperimenten an Bodensäulen. PhD thesis. Universität Bayreuth.

Schulz, J. 1995. Aufbau von Säulenversuchen zur Untersuchung der Pyritoxidation in Braunkohlentagebausedimenten. Diplomarbeit. Ruhr-Universität Bochum, Universität/GH Essen.

Selvadurai, A. P. S., J. Hu, and I. Konuk. 1999. Computational modelling of frost heave induced soil-pipeline interaction: I. modelling of frost heave. Cold Regions Science and Technology 29:215–228.

Shoop, S. A., and S. R. Bigl. 1997. Moisture migration during freeze and thaw of unsaturated soils: modeling and large scale experiments. Cold Regions Science and Technology 25:33–45.

Spaans, E. J. A., and J. M. Baker. 1996. The soil freezing characteristic: Its measurement and similarity to the soil moisture characteristic. Soil Sci. Soc. Am. J. 60:13–19.

Stähli, M., P.-E. Jansson, and L.-C. Lundin. 1999. Soil moisture redistribution and infiltration in frozen soils. Water Resour. Res. 35:95–103.

Thorstenson, D. C., and D. W. Pollock. 1989a. Gas transport in unsaturated porous media: The adequacy of Fick's law. Reviews Geophysics 27:61–78.

Thorstenson, D. C., and D. W. Pollock. 1989b. Gas transport in unsaturated zones: Multicomponent systems and the adequacy of Fick's laws. Water Resour. Res. 25:477–507.

van Genuchten, M. T. 1980. A closed-form equation for predicting the hydraulic conductivity of unsaturated soils. Soil Sci. Soc. Am. J. 44:892–898.

Weast, R. C. (ed.) 1995. CRC Handbook of Chemistry and Physics. 76th. CRC Press, Boca Raton, FL.

Weischet, W. 1991. Einführung in die Allgemeine Klimatologie. 5. Auflage. Teubner Studienbücher.

Zachmann, D. W., P. C. Duchateau, and A. Klute. 1982. Simultaneous approximation of water capacity and soil hydraulic conductivity by parameter identification. Soil Sci. 134:157–163.

Zhang, T., R. Barry, K. Knowles, J. Heginbottom, and J. Brown. 1999. Statistics and characteristics of permafrost and ground ice distribution in the northern hemisphere. Polar Geogr. 23:147–169.

Zhao, L., D. M. Gray, and D. H. Male. 1997. Numerical analysis of simultaneous heat and mass transfer during infiltration into frozen ground. Journal of Hydrology 200:345–363.

Zurmühl, T. 1994. Validierung konvektiv-dispersiver Modelle zur Berechnung des instationären Stofftransports in ungestörten Bodensäulen. Vol. 36 of Bayreuther Bodenkundliche Berichte. Lehrstuhl für Bodenkunde und Bodengeographie der Universität Bayreuth, Bayreuth.

Appendix

A. Hydraulic Parameters for the Test Calculations

A.1. Yolo Light Clay

$$K_w = K_s \cdot \frac{A}{A + |h_m|^\beta}; \quad K_s = 4.428 \cdot 10^{-2} cm/h, \quad A = 124.6, \quad \beta = 1.77 \quad \text{(A.1)}$$

$$\theta_w = \frac{\alpha(\theta_s - \theta_r)}{\alpha + (\ln|h_m|)^\beta} + \theta_r; \quad \left. \begin{array}{ll} \theta_s = 0.495, & \theta_r = 0.124, \\ \alpha = 739, & \beta = 4 \end{array} \right\} \quad \text{if } h_m < -1 \ cm$$

$$\theta = \theta_s \qquad\qquad\qquad\qquad\qquad\qquad\qquad \text{if } h_m \geq -1 \ cm$$

A.2. Sand

$$K_w = K_s \cdot \frac{A}{A + |h_m|^\beta}; \quad K_s = 34 cm/h, \quad A = 1.175 \cdot 10^6, \quad \beta = 4.74 \quad \text{(A.2)}$$

$$\theta_w = \frac{\alpha(\theta_s - \theta_r)}{\alpha + |h_m|^\beta} + \theta_r; \quad \theta_s = 0.287, \quad \theta_r = 0.0.075, \quad \begin{array}{l} \alpha = 1.611 \cdot 10^6 \\ \beta = 3.96 \end{array}$$

B. Texture and Composition of the Bayelva Profile

The texture and composition of disturbed soil samples were measured at the Alfred-Wegener-Institute, Potsdam. Wet soil was passed through a sieve with a mesh size of 63 μm to measure the sand content. Silt and clay were separated by sedimentation in an Atterberg cylinder after destruction of limestone and organic carbon. Linear interpolation was used between the 25 sampling points.
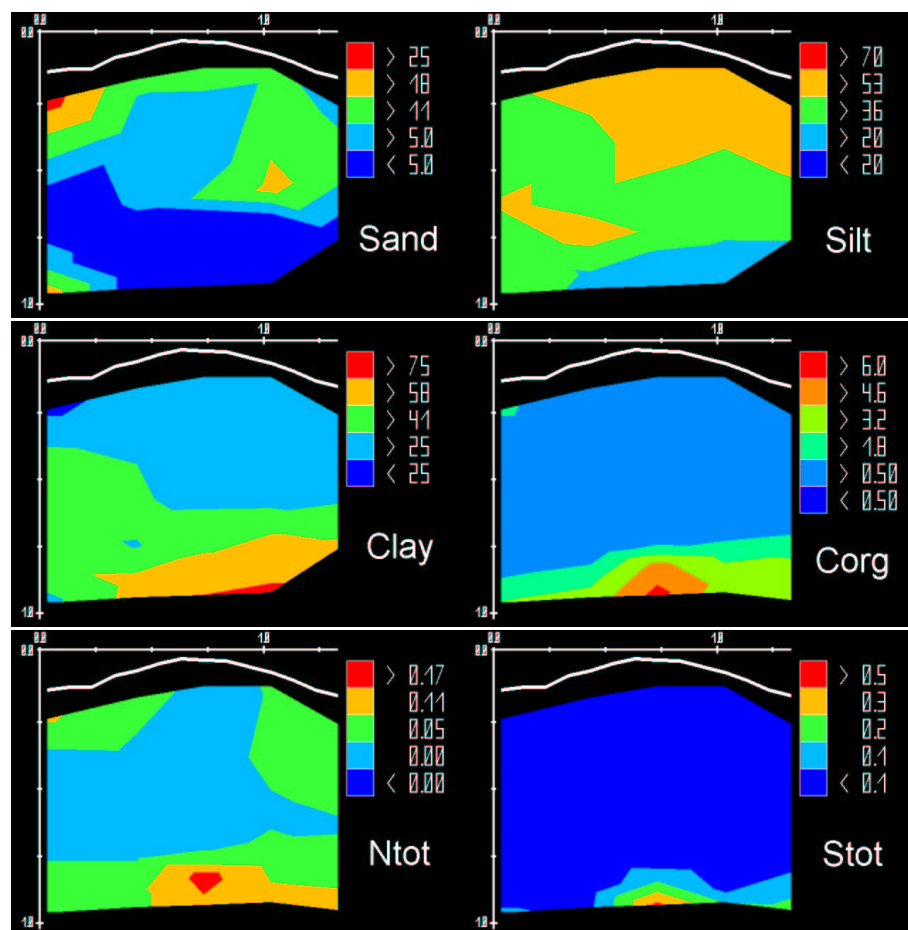
C. Algorithm for the Evaluation of TDR-traces

Heimovaara (1993) developed an algorithm for the automatic evaluation of TDR waveforms. Only a rough description is given here to demonstrate the modification which was made to the algorithm. For details the reader is referred to the original source.

The travel time of a guided electromagnetic wave in soil (Δt_s) is calculated from

$$\Delta t_s = \Delta t_p - \Delta t_0. \tag{C.1}$$

Δt_p is the difference in time between the reflections at the beginning and the end of the TDR probe and Δt_0 is a correction for the travel time between the reflection at the beginning of the probe and the point where the signal enters the soil. The position of the first reflection depends on the cable length and changes with temperature while the distance between both reflections depends on the square root of the relative permittivity of the material between and around the rods of the probe. The signal of a probe immersed in water is shown in figure C.1.
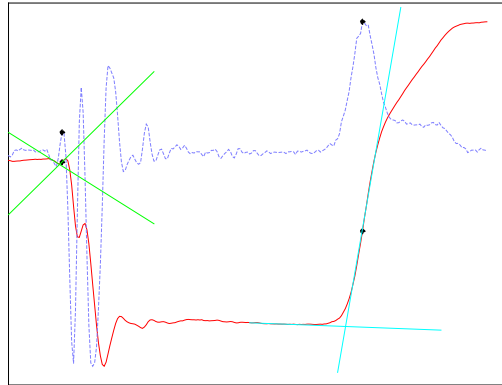
Figure C.1.: TDR waveform for a probe immersed in water (reflection coefficient versus travel time, red), its first derivative (blue dashed) and the regression lines for the determination of the first (green) and second (turquoise) reflection. Inflection points are marked by black rhombs.

The intersection points of straight lines fitted to the measured signal are calculated to determine the reflection points. The lines fitted to the rising section are drawn through the inflection point (the maximum of the first derivative). In the practical application of the algorithm, the global maximum of the first derivative was always found to be related to the second reflection point. A unique determination of the inflection point corresponding to the first reflection is not always possible as there is more than one inflection near the first reflection as can also be seen in figure C.1. This situation is exacerbated if the signal is noisy. In Heimovaara's original algorithm smoothing of the signal was used to cope with this problem which led to a reduced precision and was not robust enough. In the modified algorithm the search for the first inflection is limited to a given interval around the position of the first reflection determined in the laboratory. Smoothing of the signal is no longer necessary. The modified algorithm was applied to more than 200'000 TDR waveforms measured at a site in Ny Ålesund and the rate of failure was below 0.1 percent.

The modified algorithm was incorporated in a program library for the measurement and evaluation of TDR waveforms, which is available as open source under the GNU Publication License.

D. Freezing Curves

The freezing curves were derived from temperature and relative permittivity measured between September 13th 1998 and September 5th 2001. Volumetric water content is plotted versus temperature. Filtering of the raw data is described in section 4.2.2, the calculation of volumetric water content from relative permittivity in section 4.2.4.1. The positions of the probes are shown in the next chapter. All values below 0 °C were plotted as dots. The lines were derived from hydraulic parameters for the loam (solid) and the silt (dashed) used in the simulations.
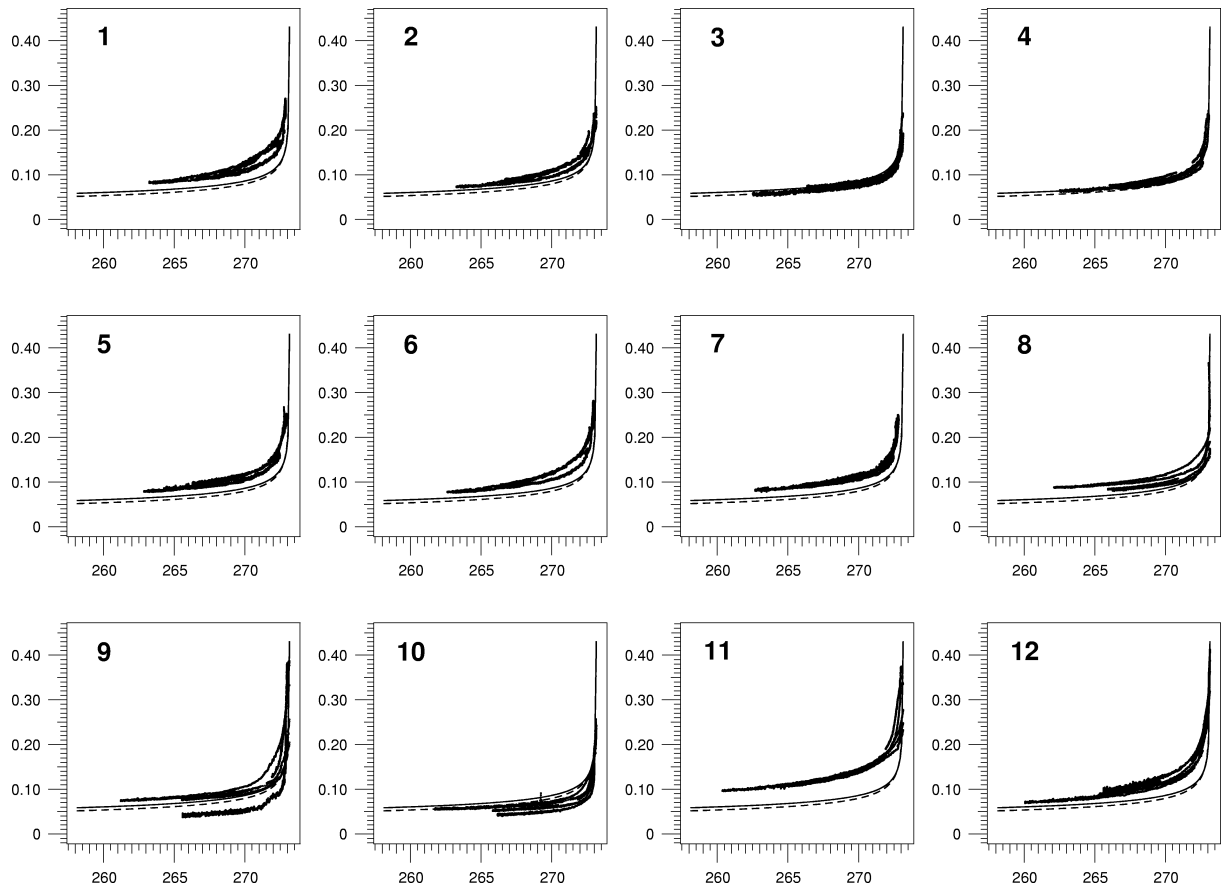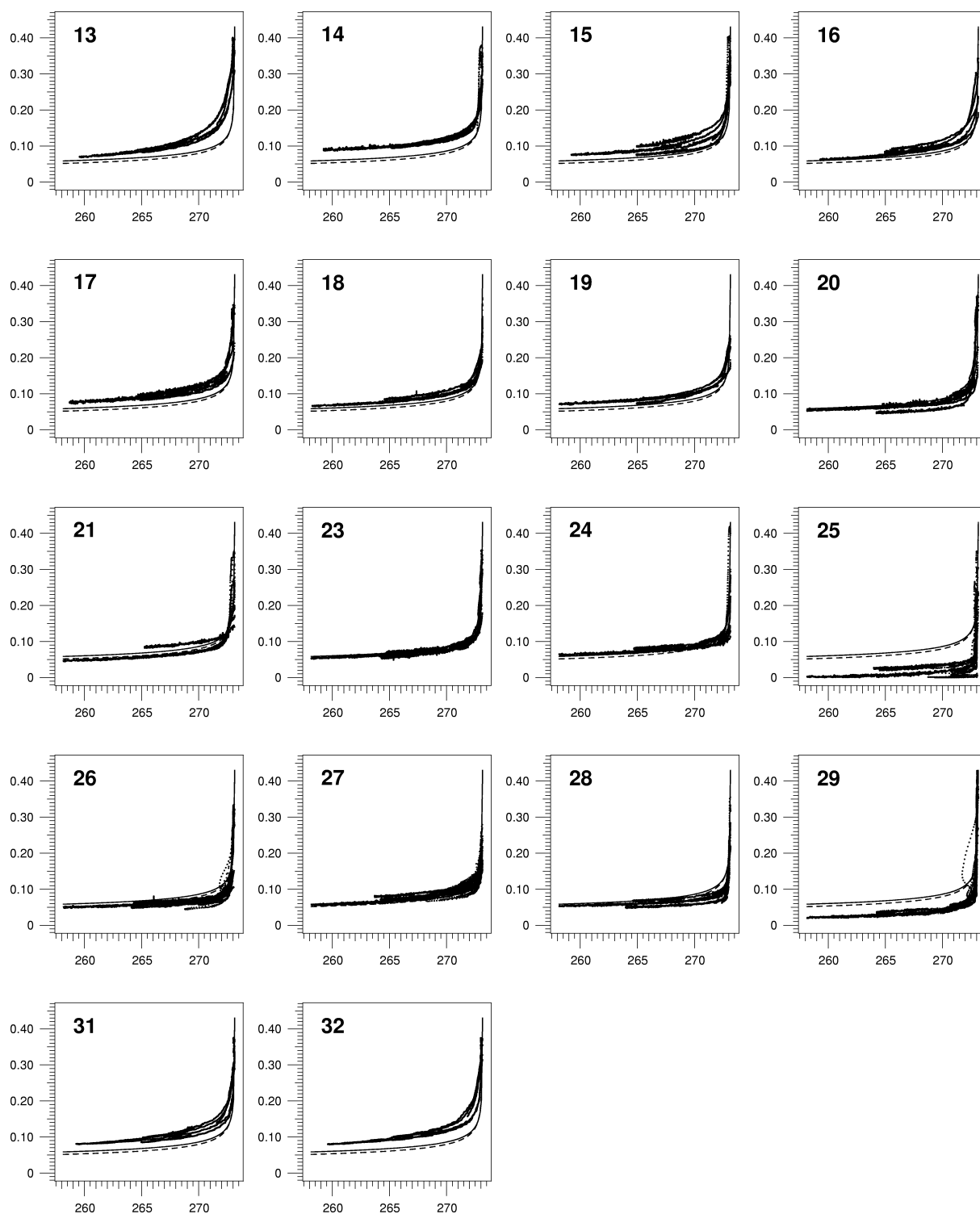
E. Simulation Results

Plots of temperature and square root of relative permittivity versus time at 24 probes are shown for each scenario on the next pages. The probe number is shown in the right upper corner of each plot. Time is given in julian days starting at January 1th 1998. Probe positions are shown below. The square root of the relative permittivity is used, as it is proportional to the really measured travel time along the TDR rods and also to the liquid water content. The black line in each plot shows measured values, the result from the simulation with the hydraulic parameters for the loam is always represented by the red line. The blue line shows the results of the particular scenario.
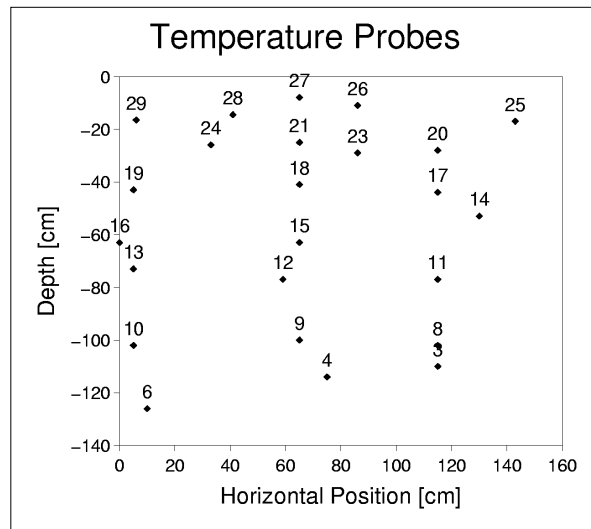
Figure E.1.: Position of the probes used in the simulation

E.1.   Measured Data

Temperature
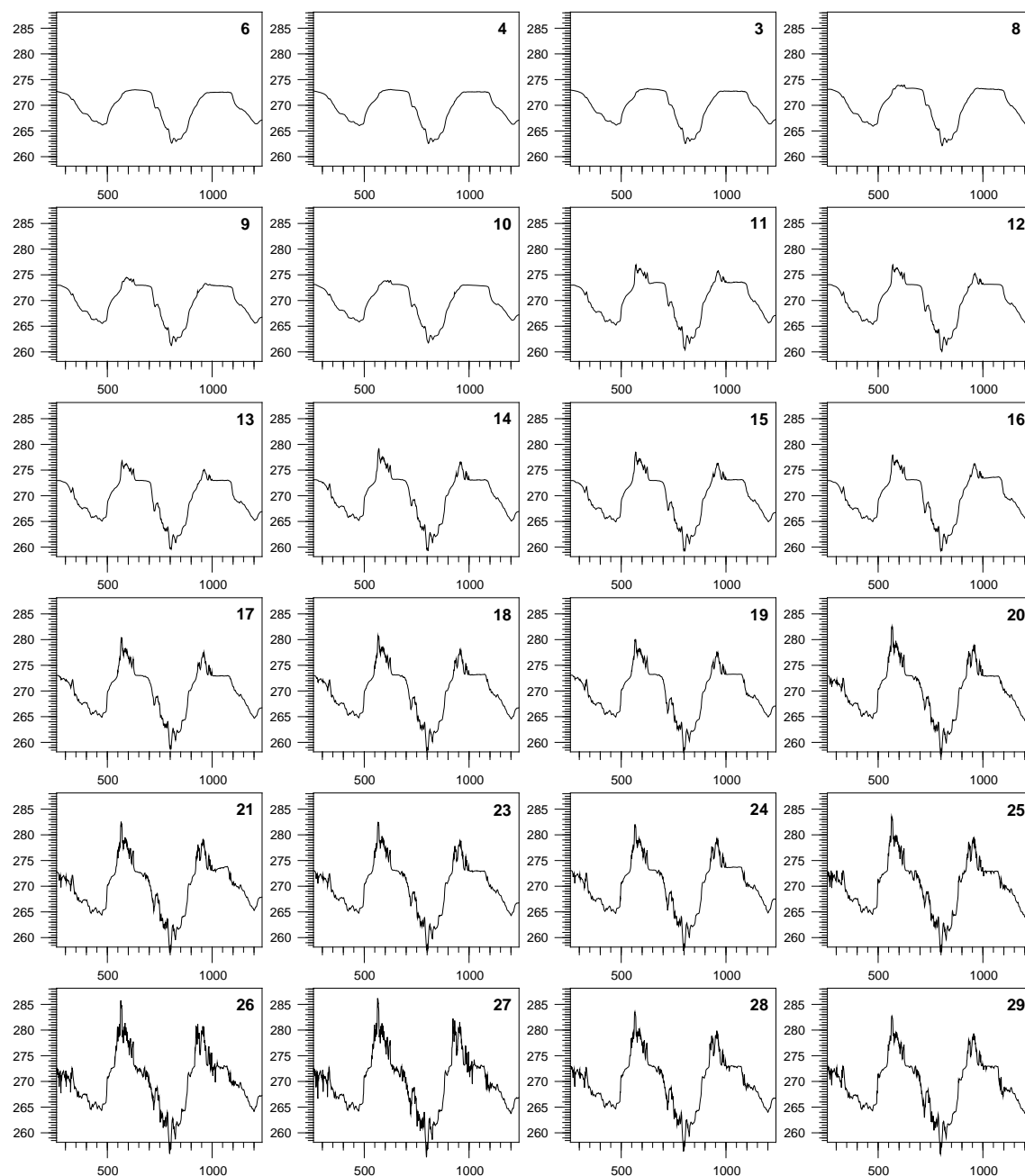
Relative Permittivity
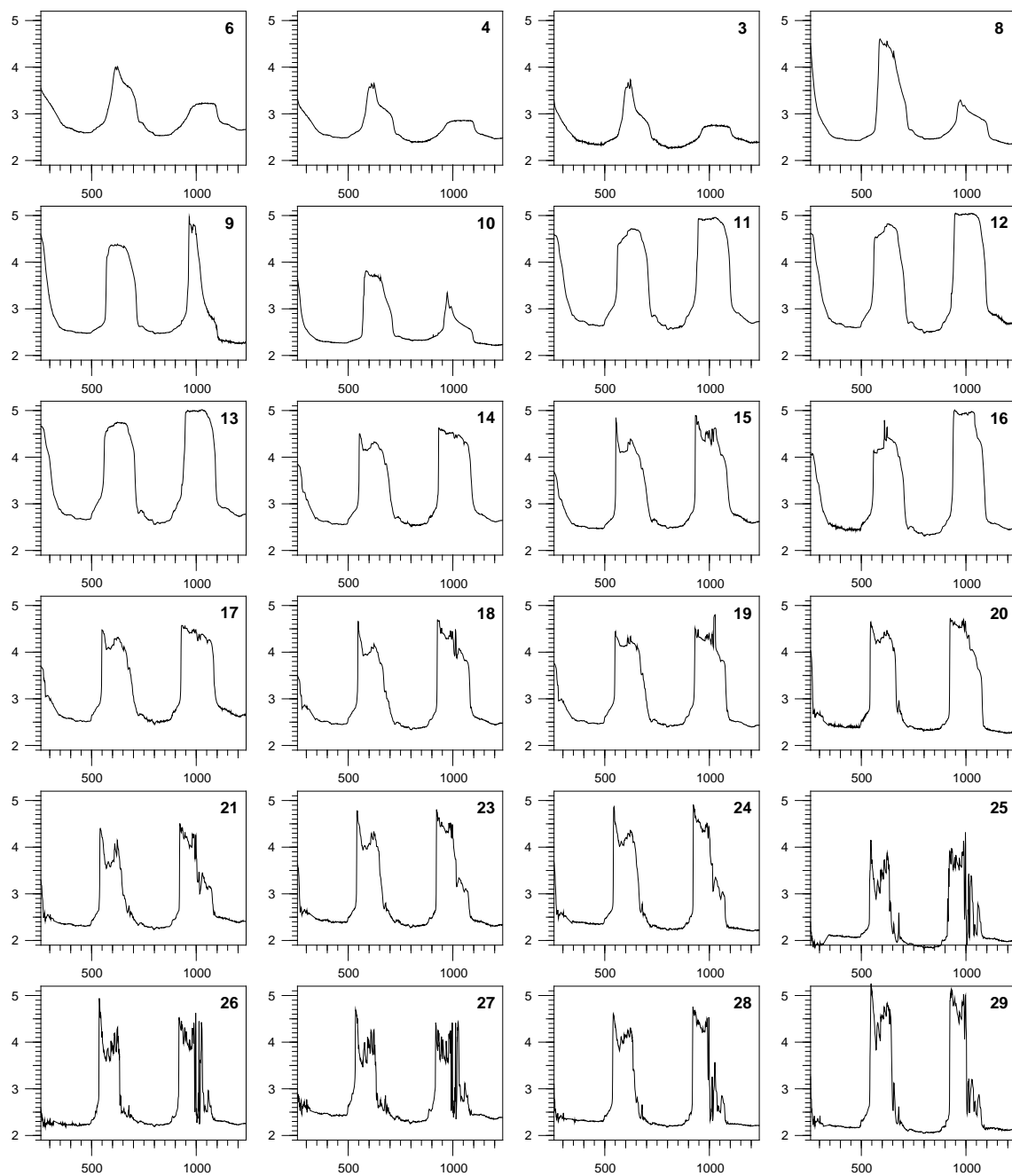
E.2.   Loam/Silt Homogeneous

Temperature
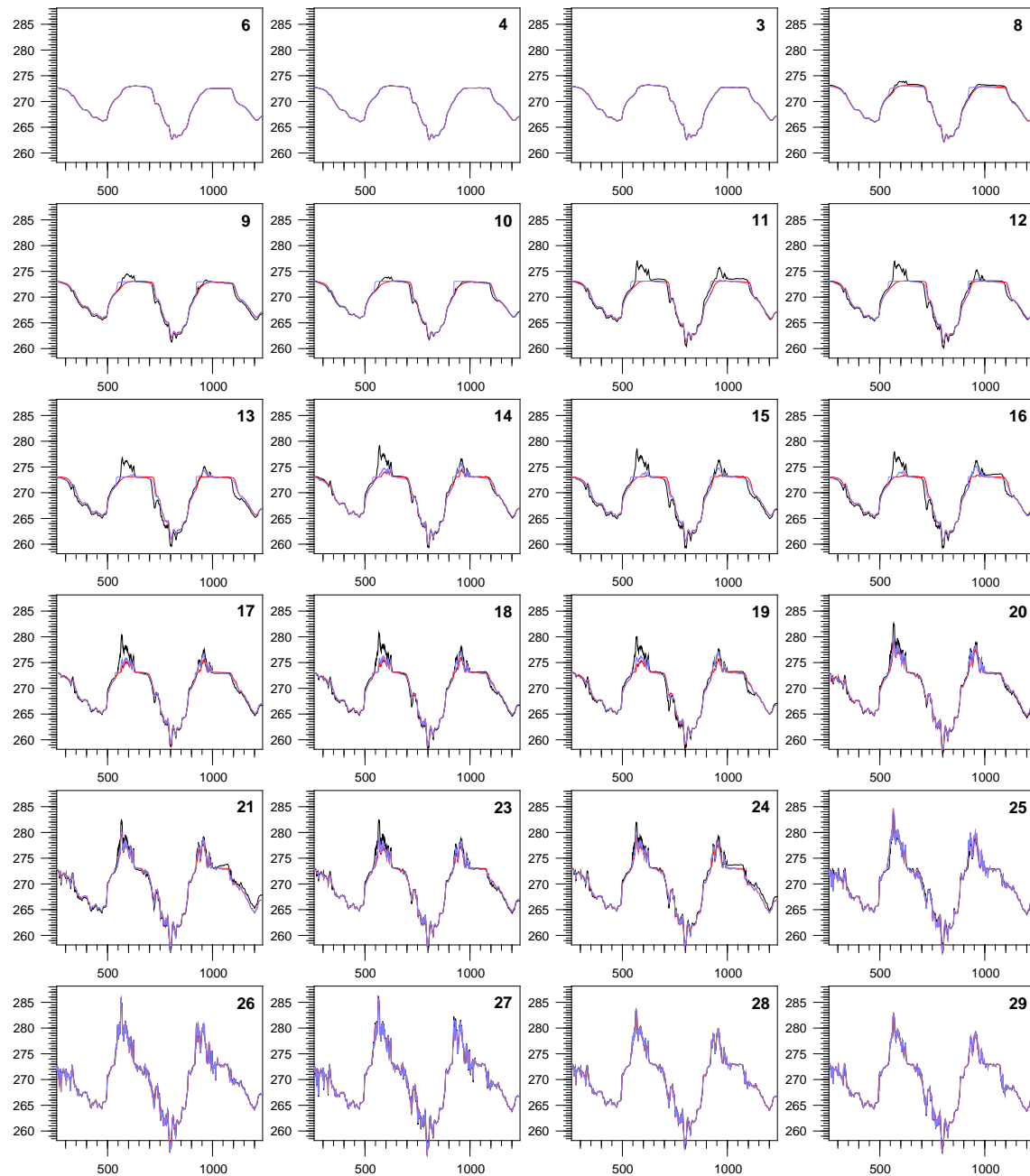
Relative Permittivity
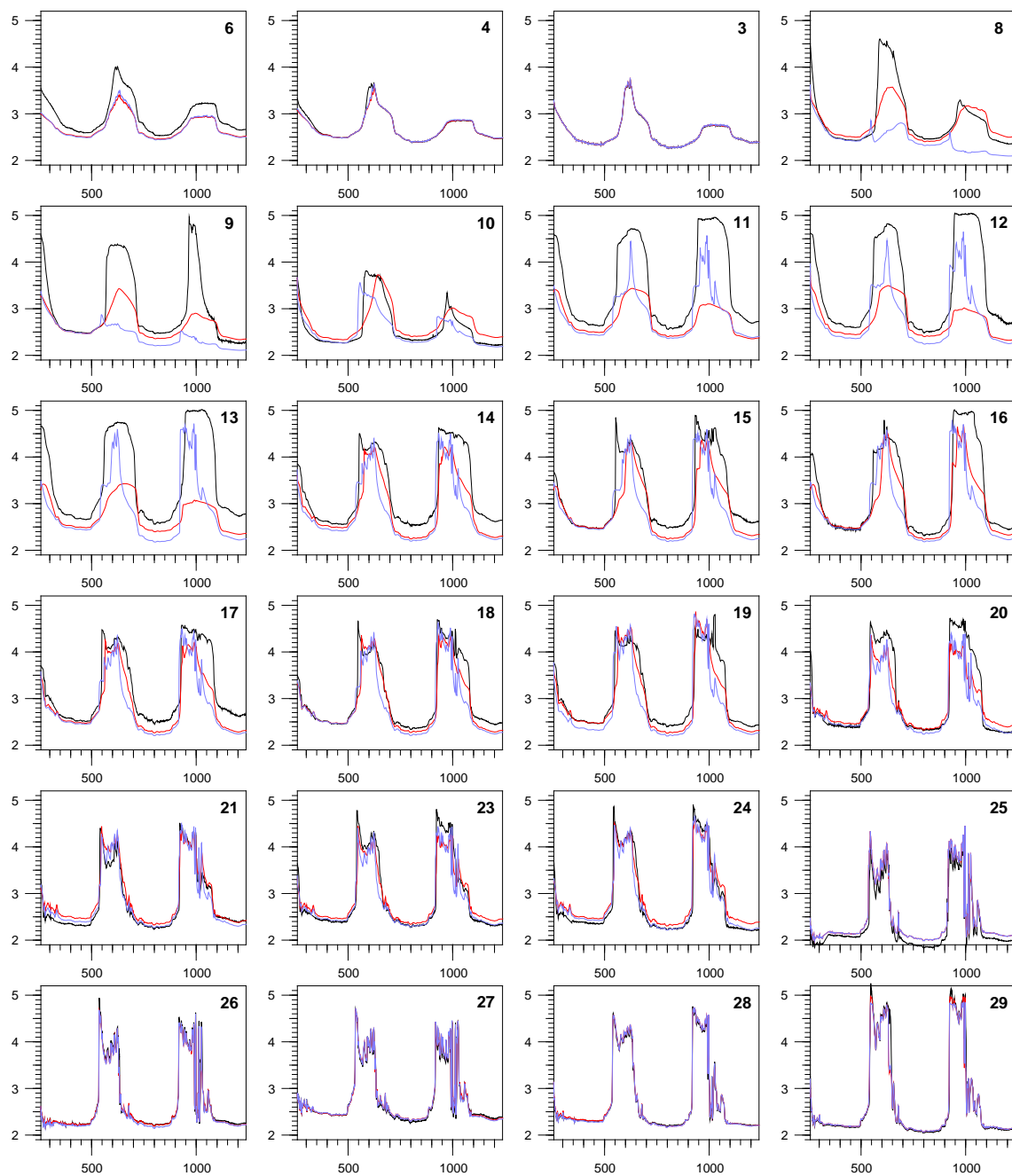
E.3. Loam/Silt with Reduced Permeability

Temperature
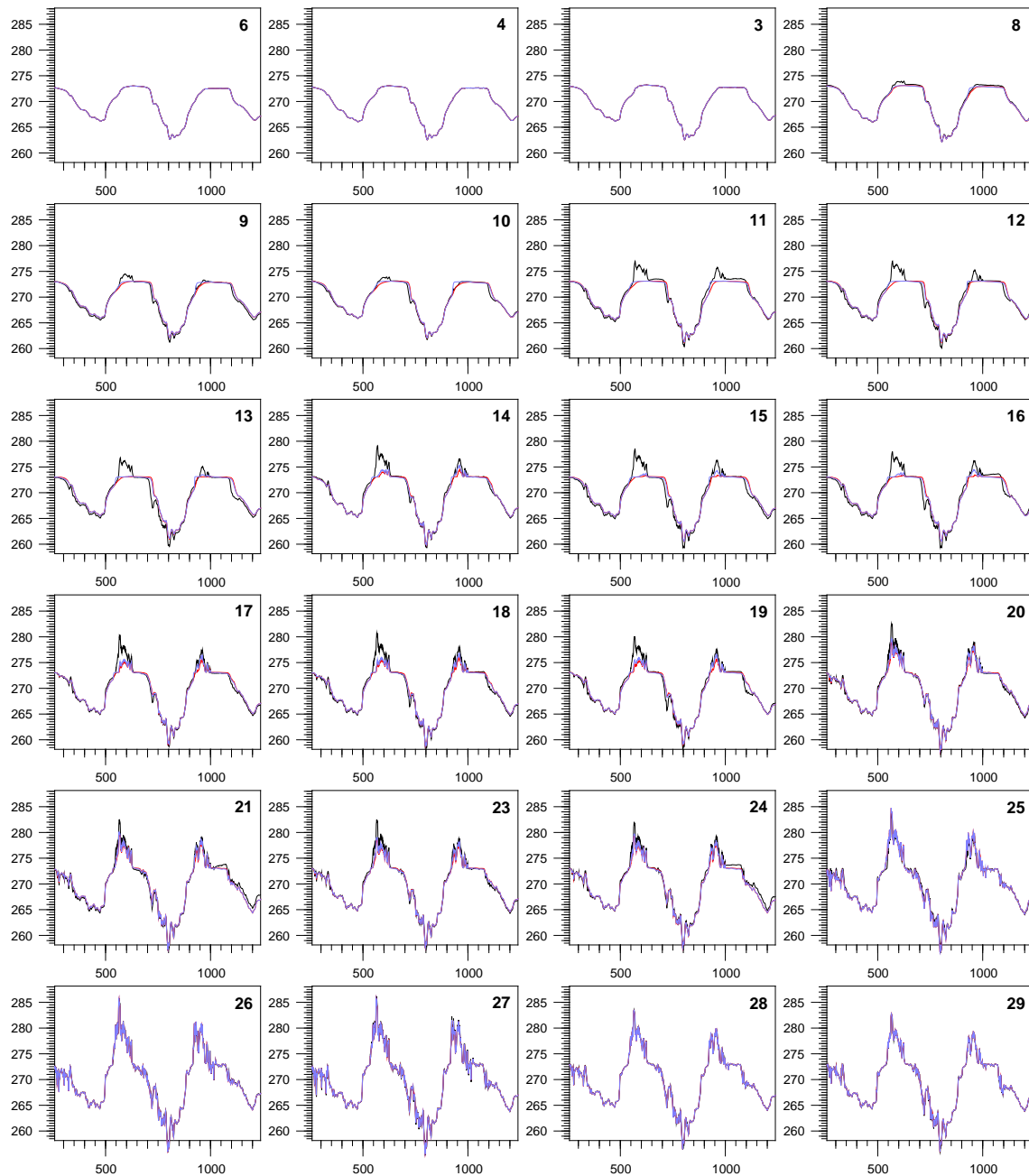
Relative Permittivity
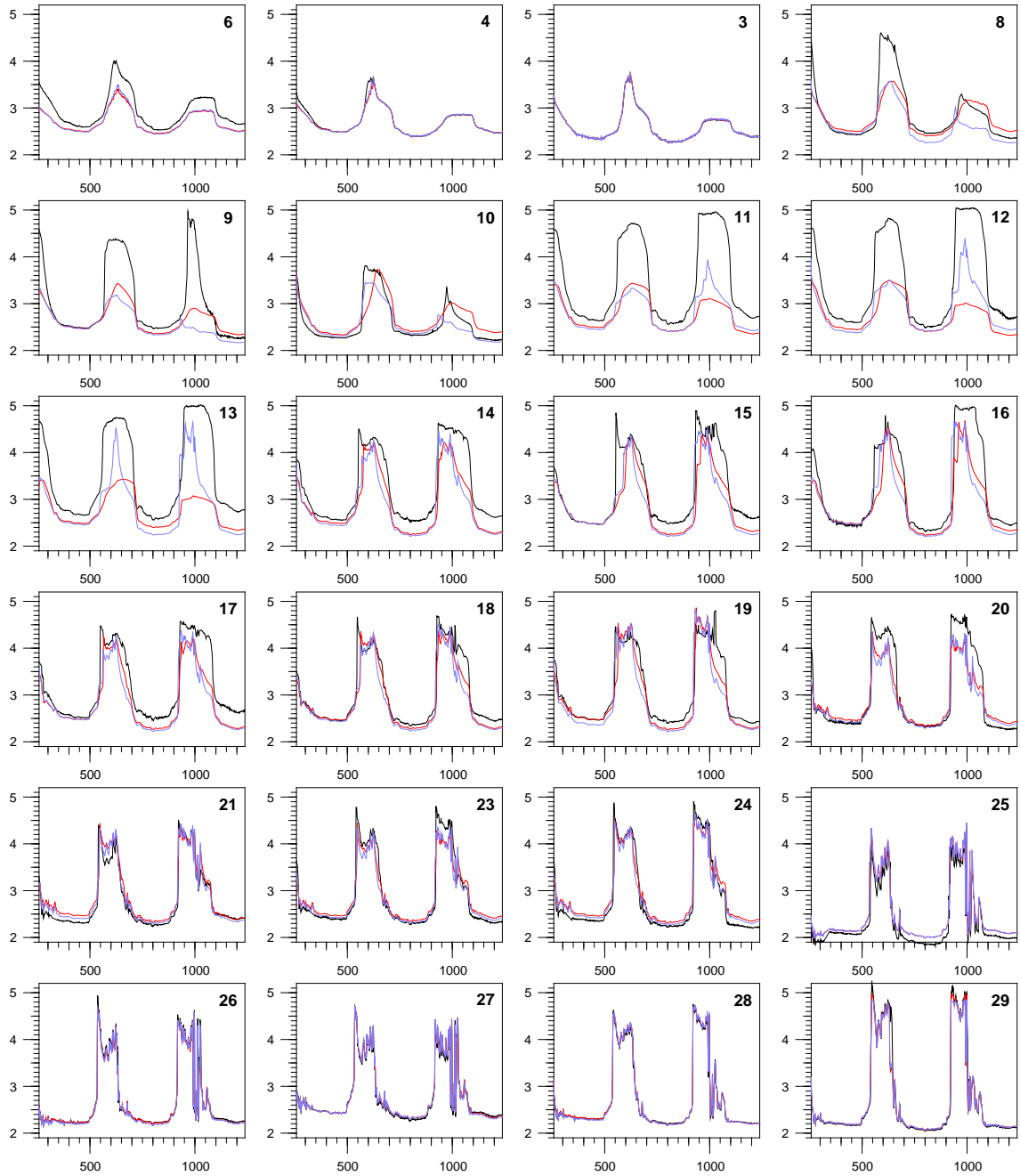
E.4.   Loam Freezing/not Freezing

Temperature
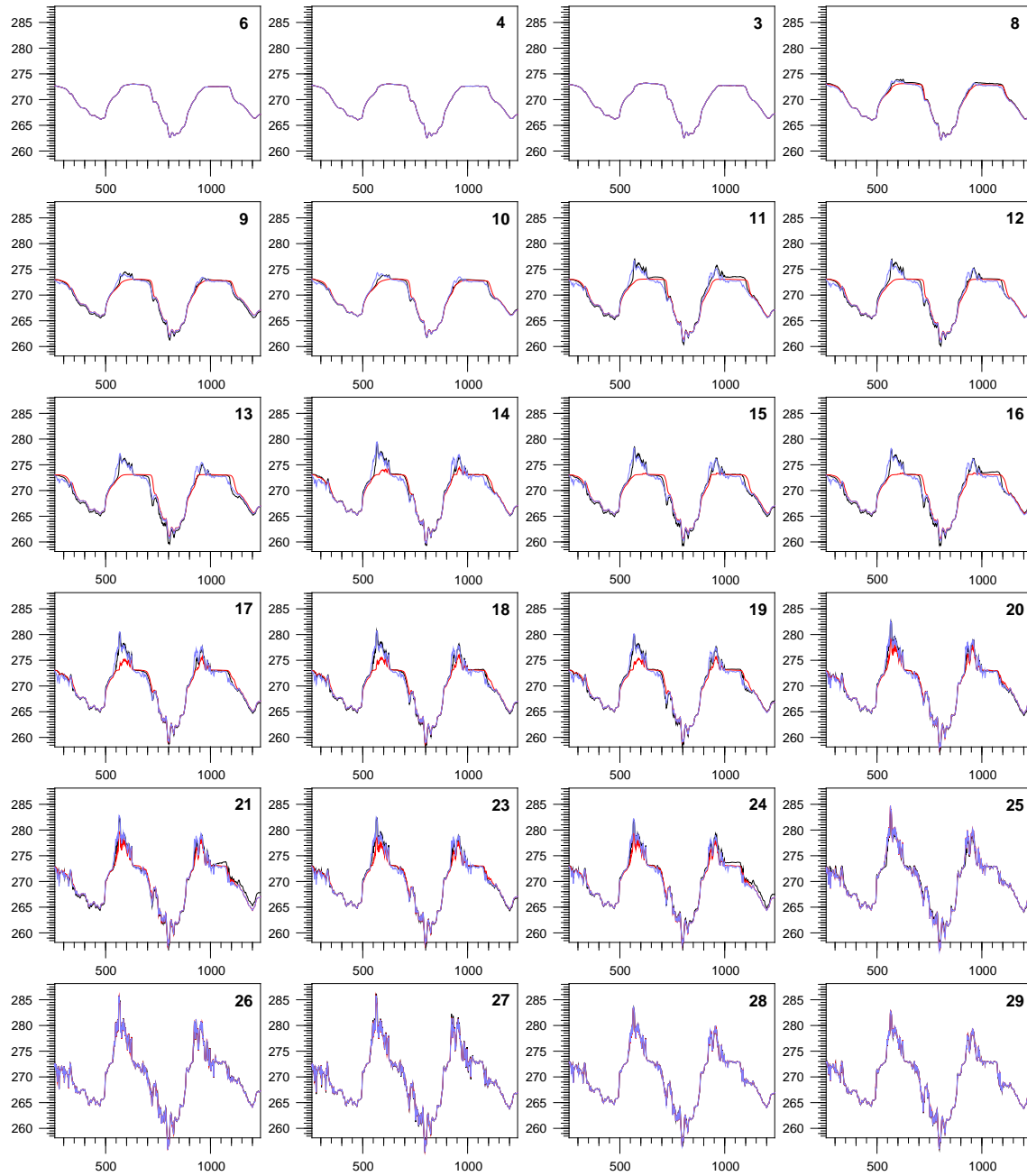
Relative Permittivity
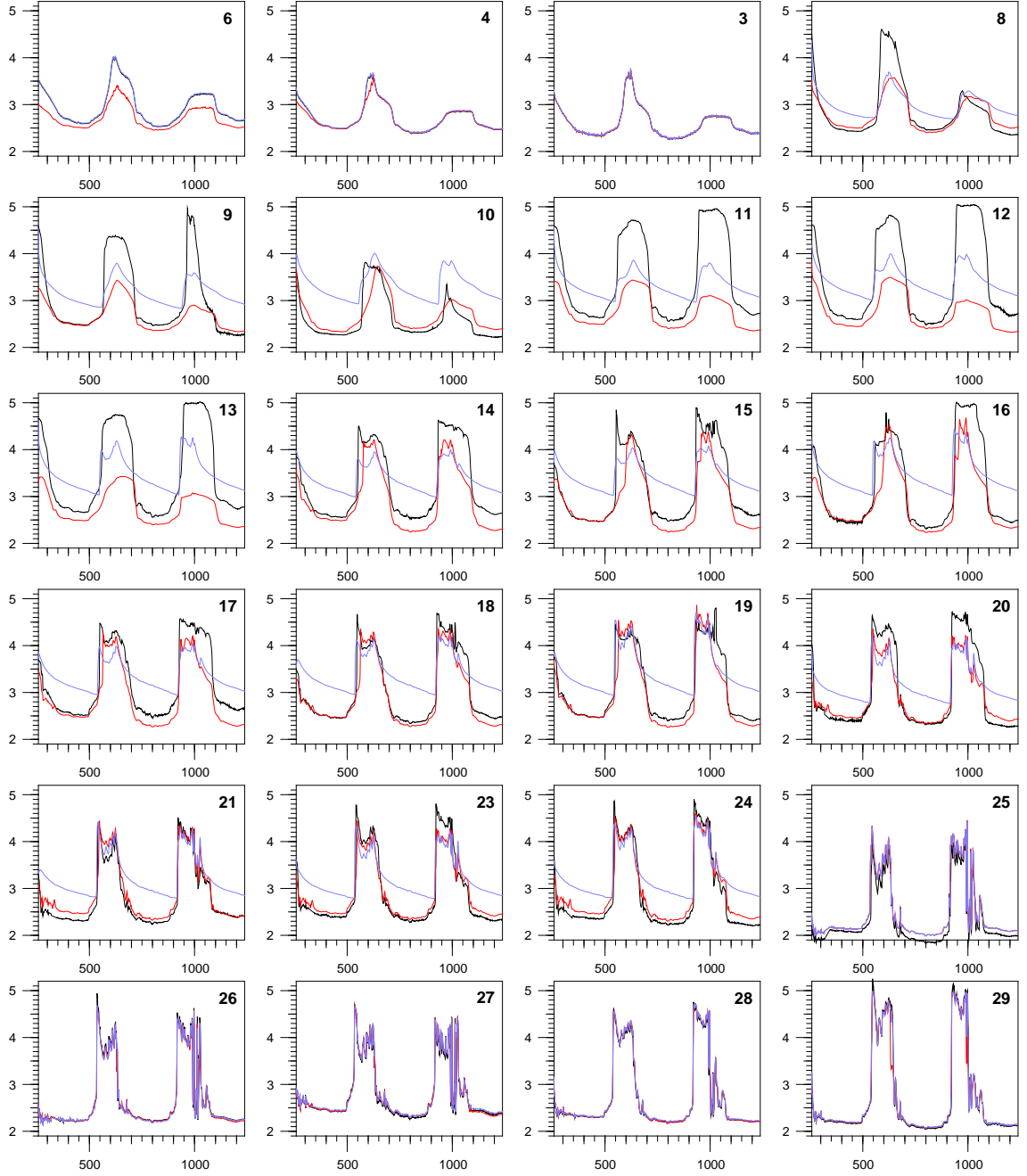
E.5. Loam Coarse Grid/Fine Grid

Temperature
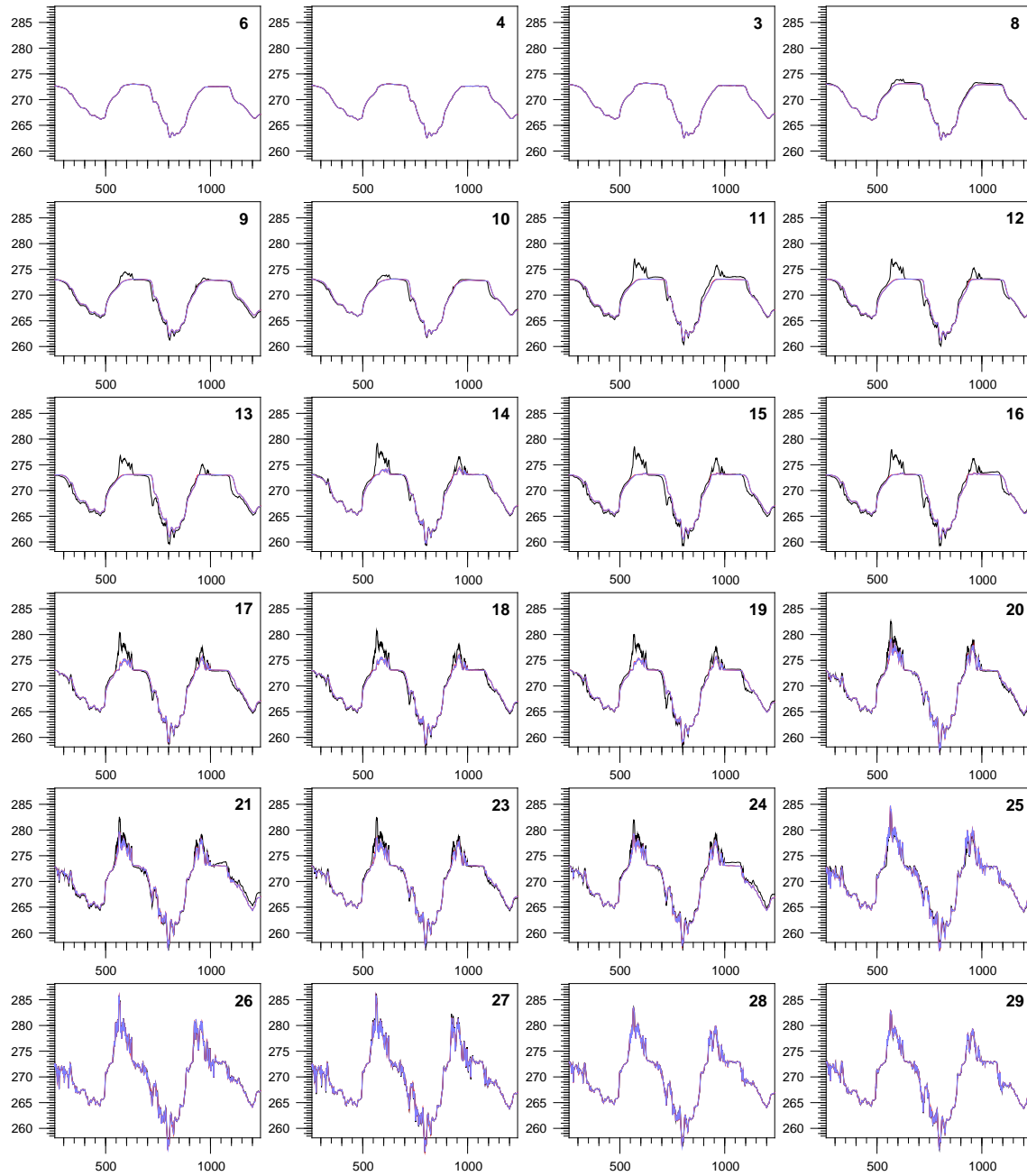
Relative Permittivity
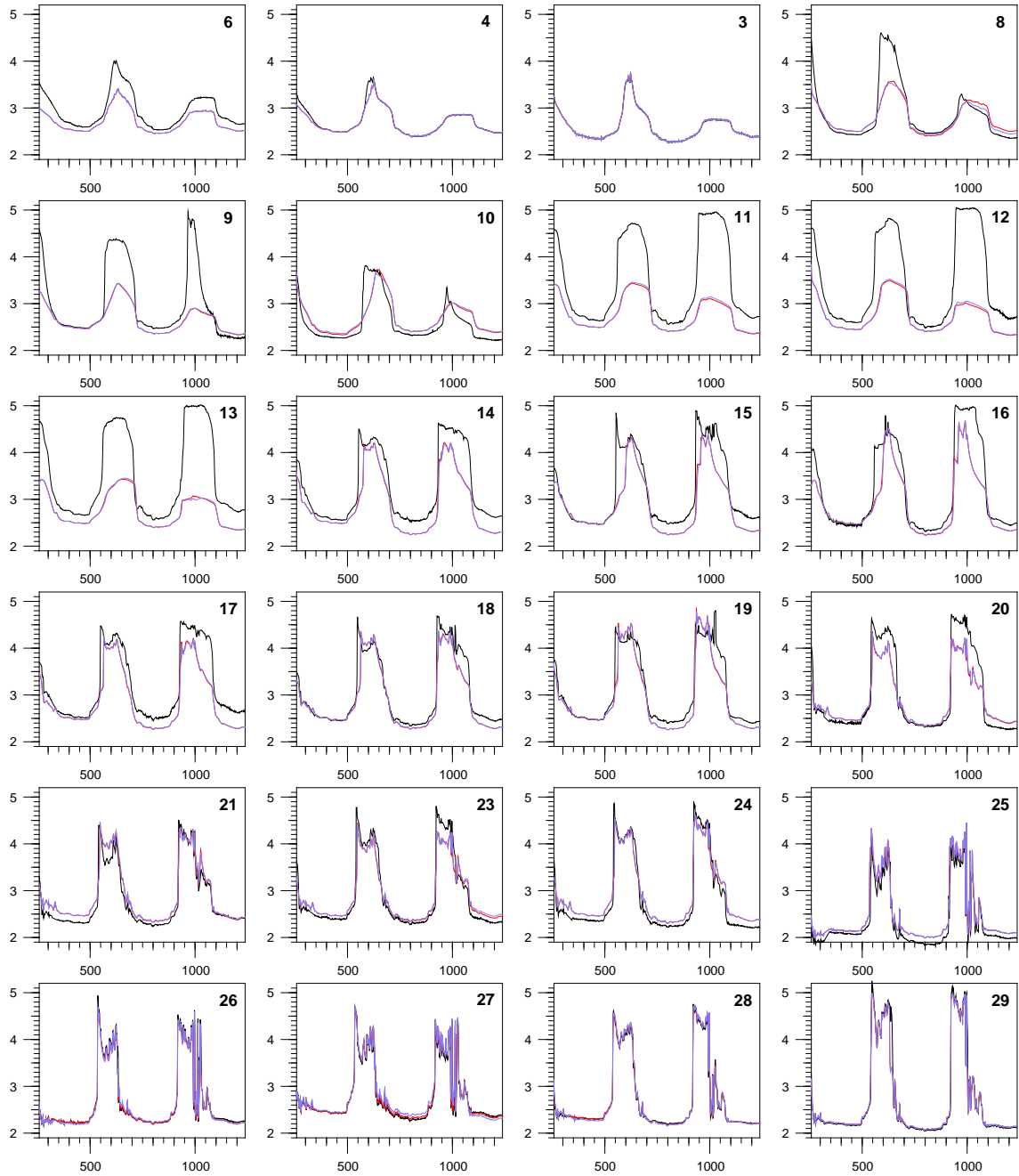
E.6. Loam with Different Initial Conditions

Temperature
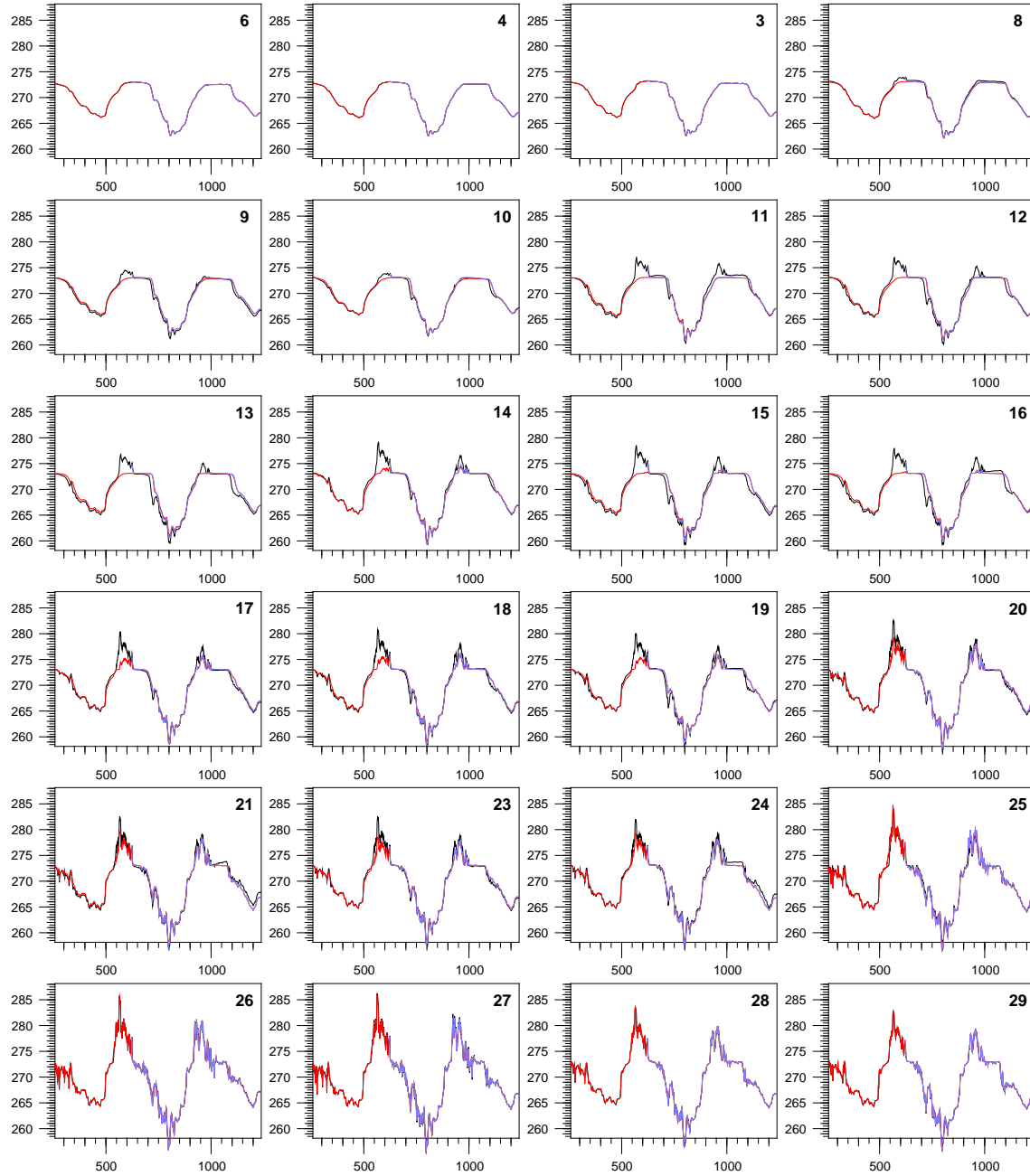
Relative Permittivity
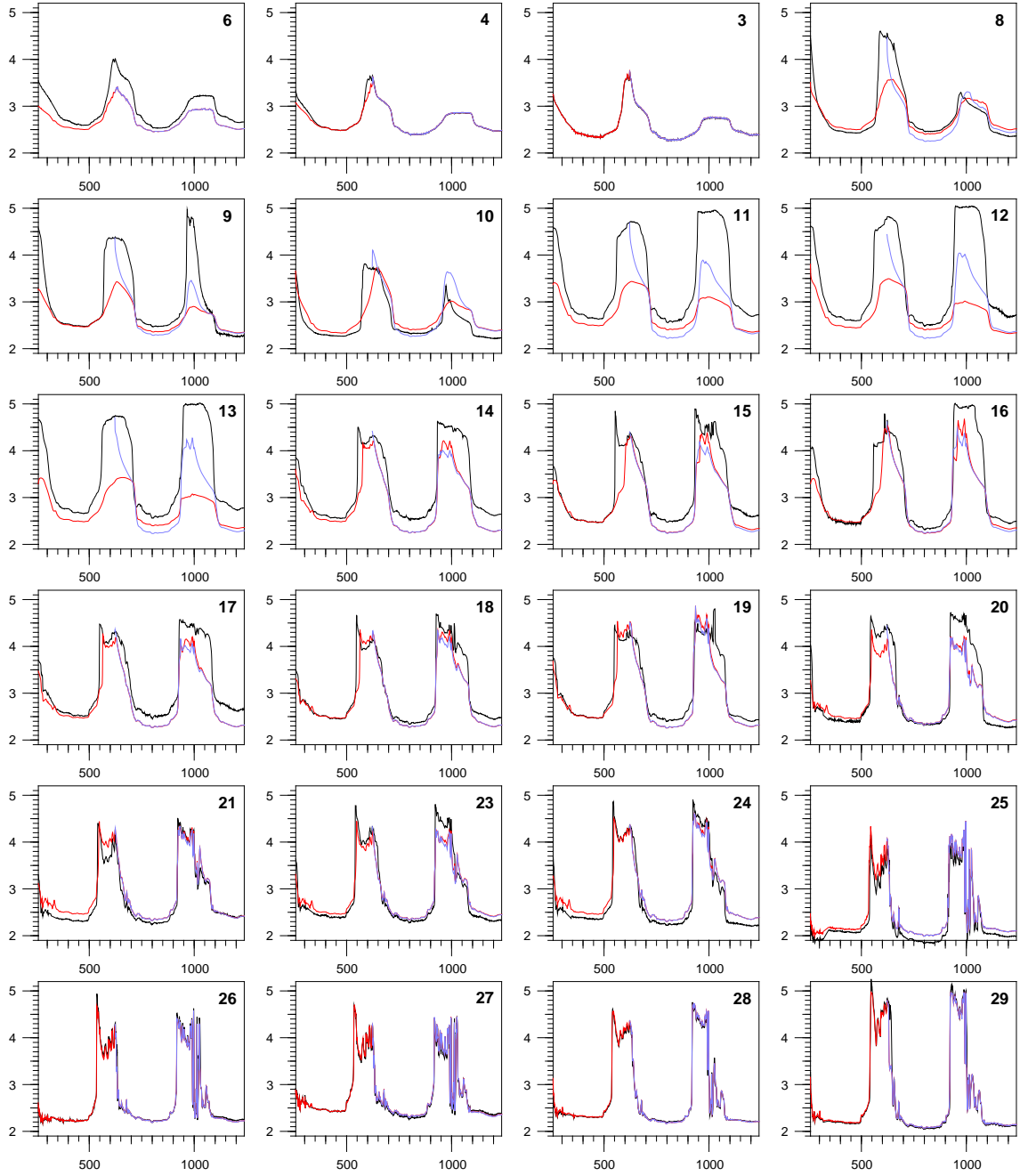
E.7.   Loam with Dirichlet Boundaries at the Sides

Temperature
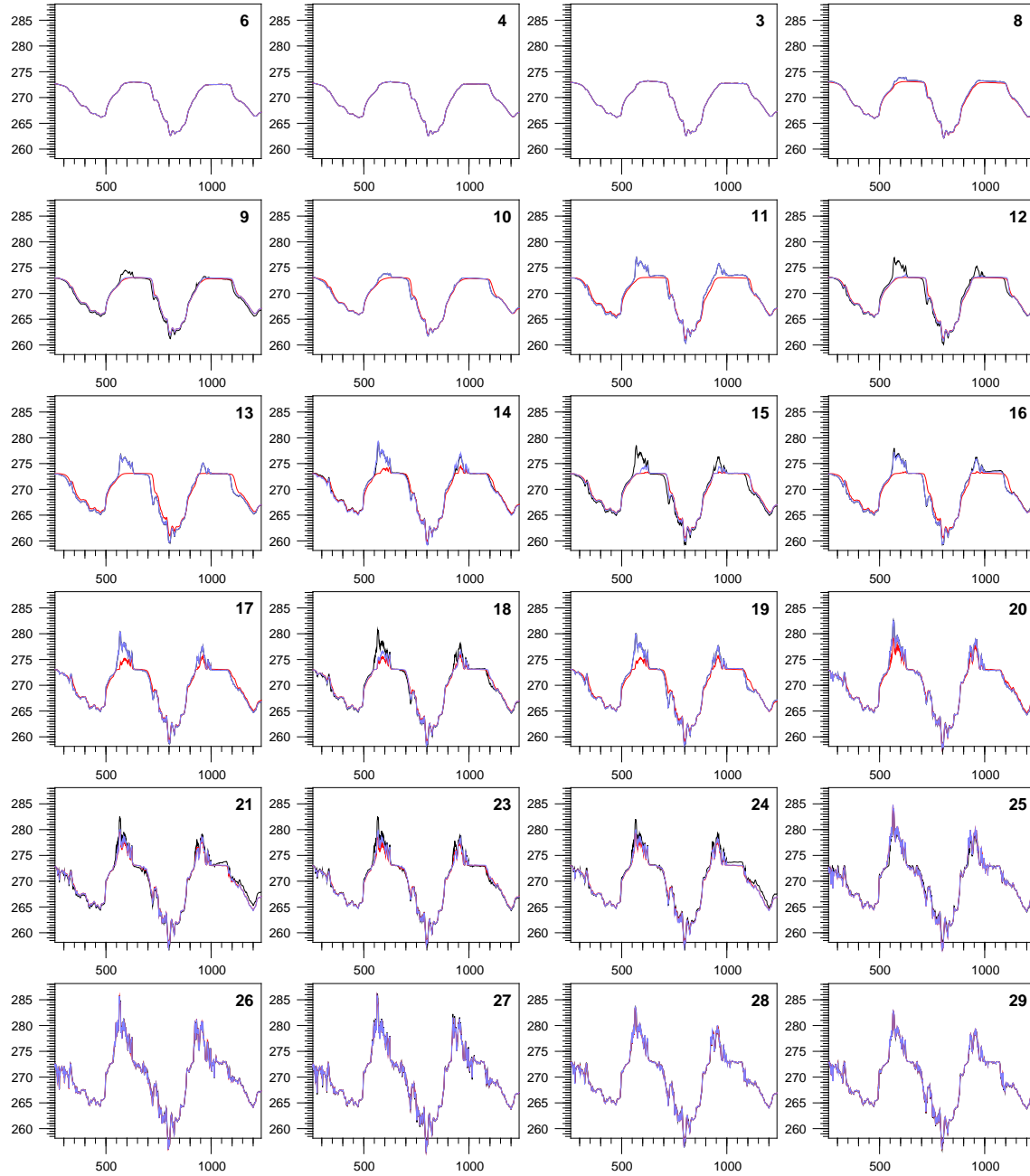
Relative Permittivity
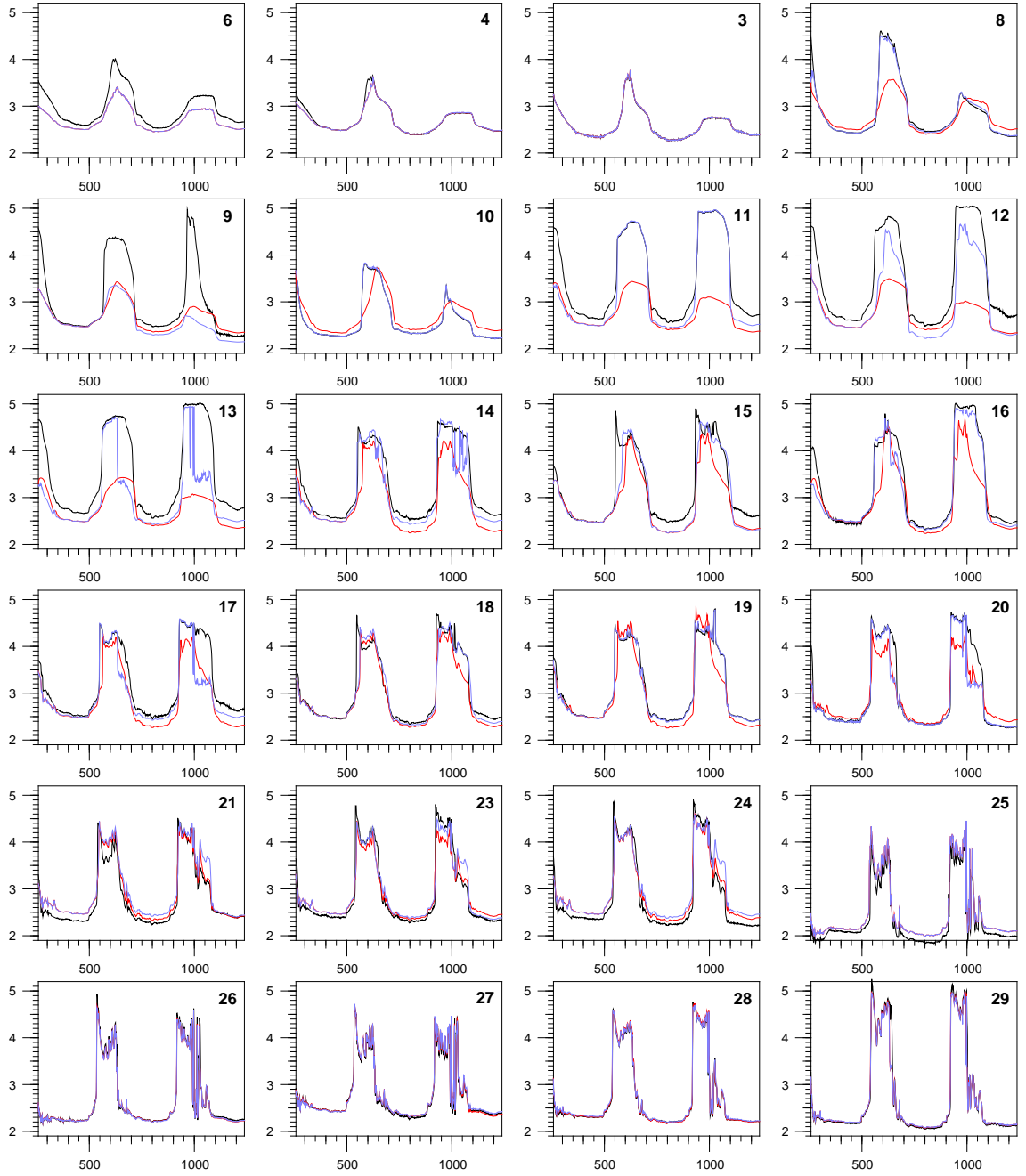
E.8. Loam with 2m deep Lower Boundary

Temperature
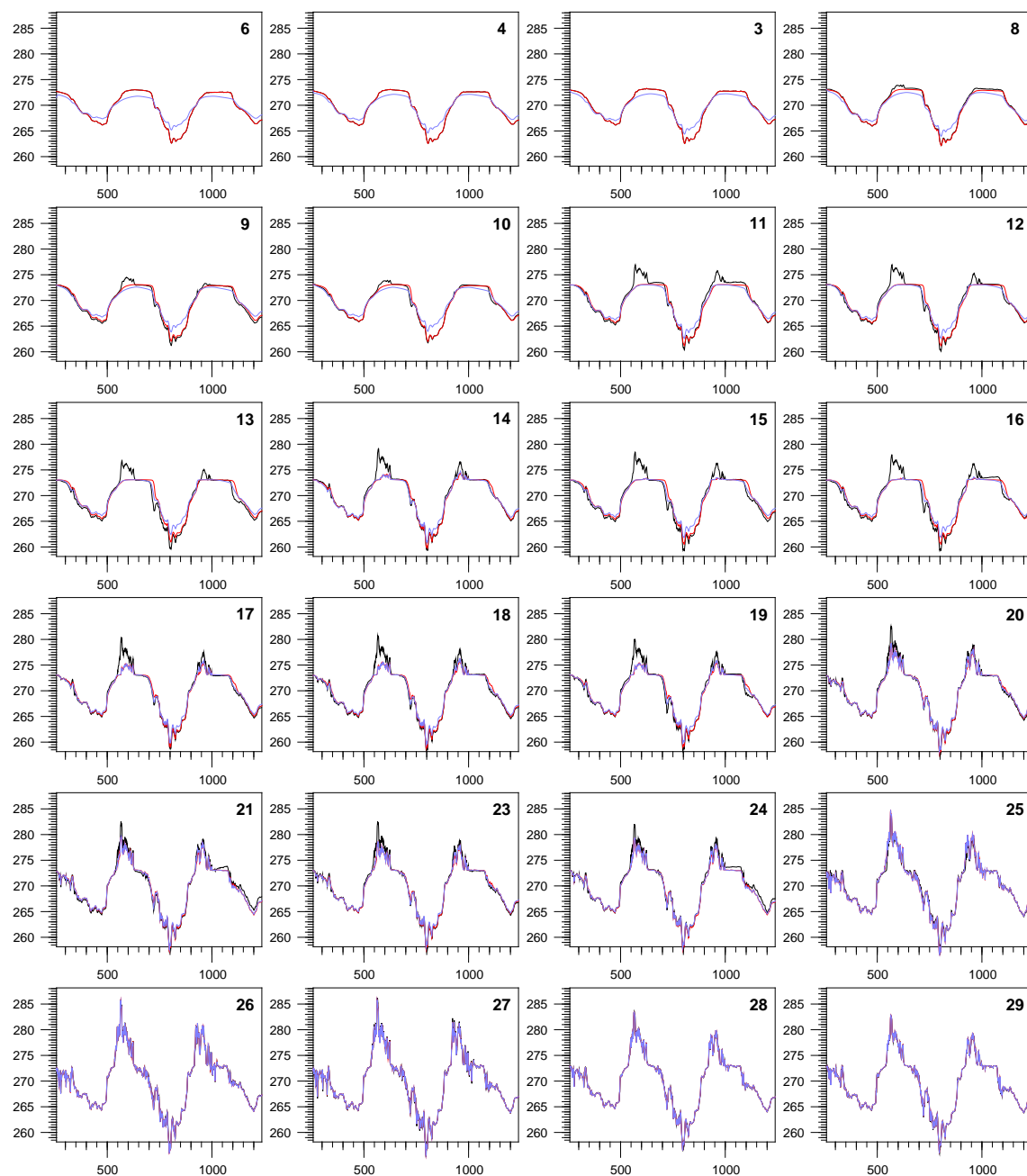
Relative Permittivity
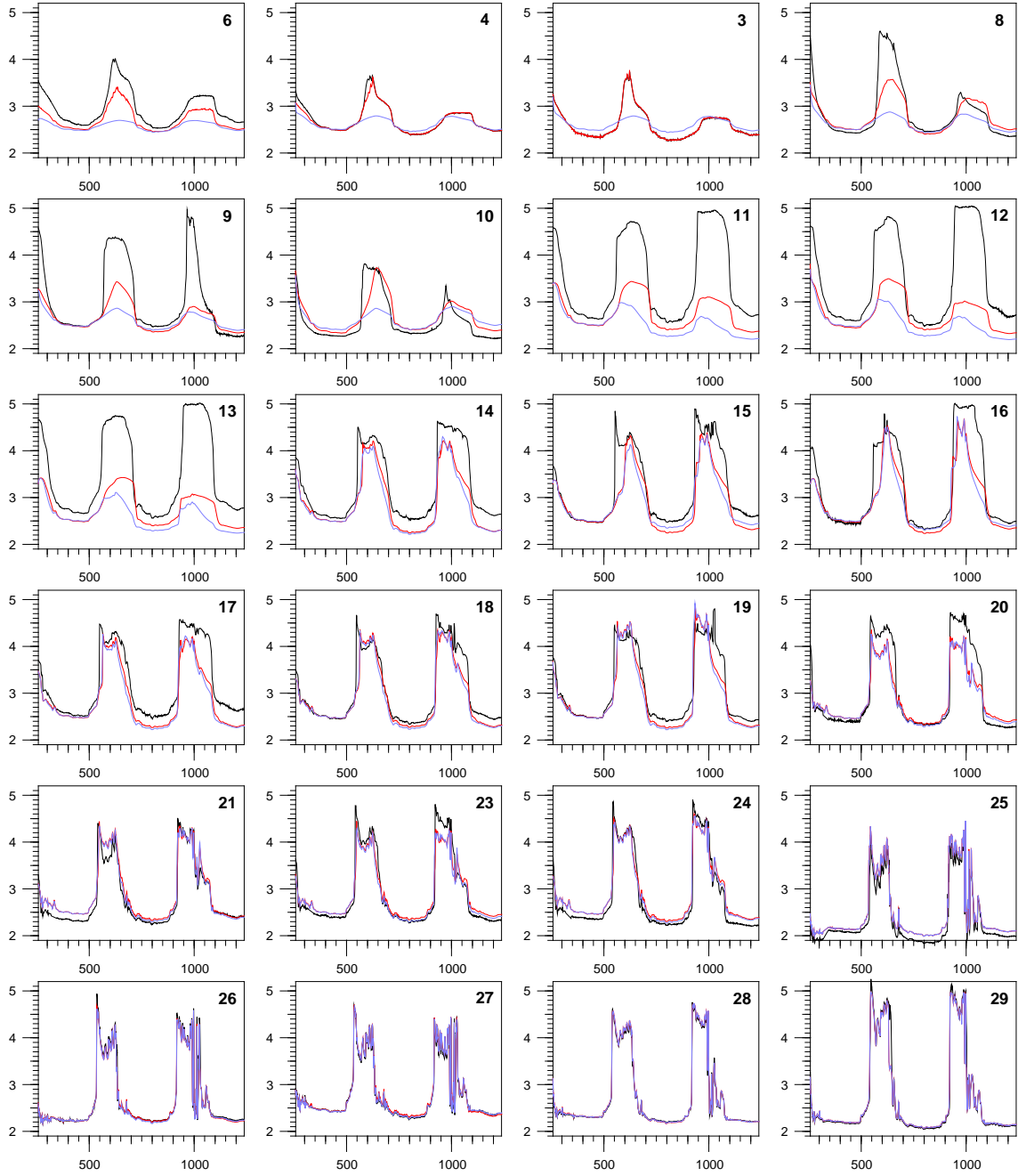
E.9.   Loam 3D Simulation

Temperature
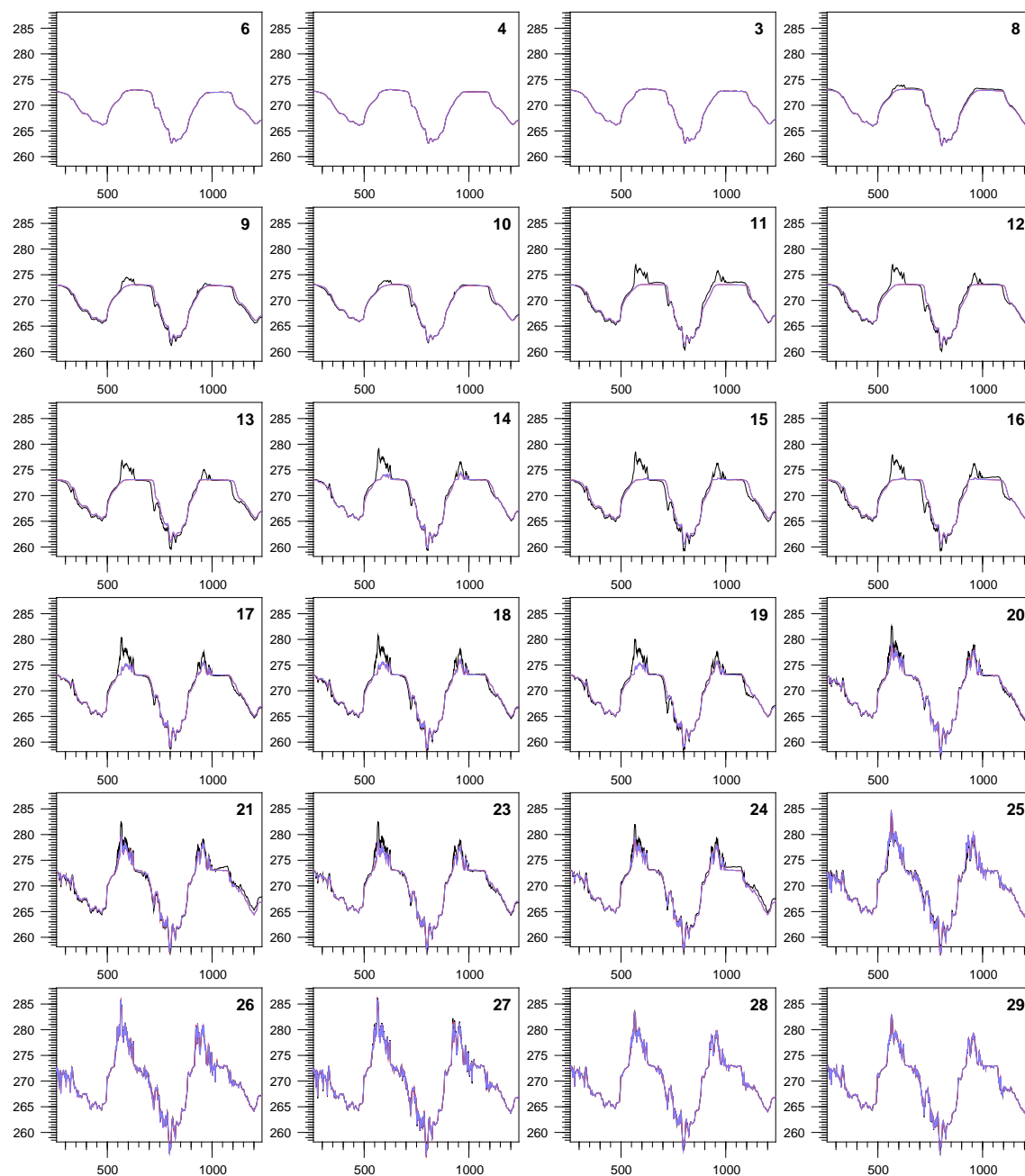
Relative Permittivity
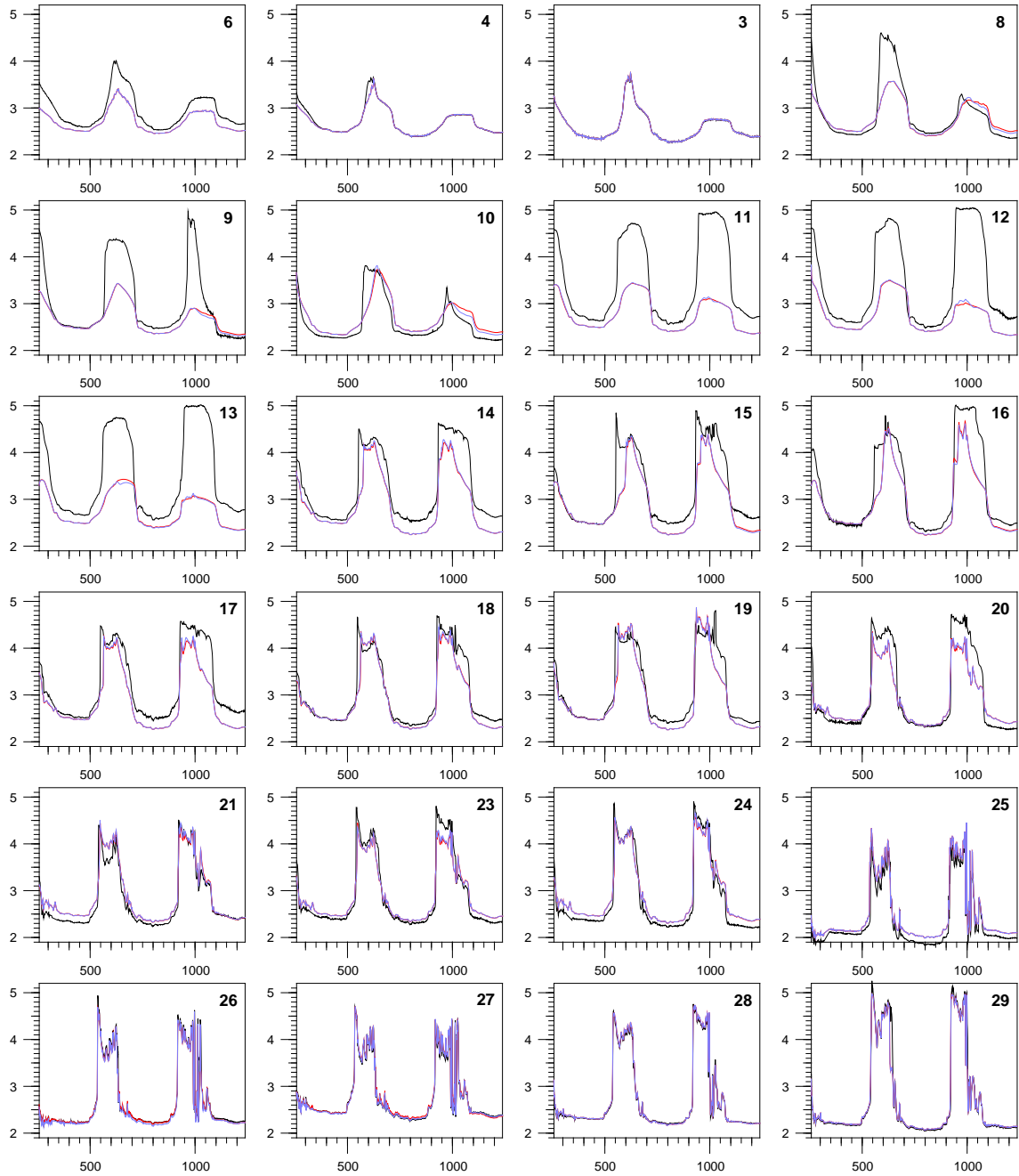
E.10.   Loam without Vapor Transport

Temperature
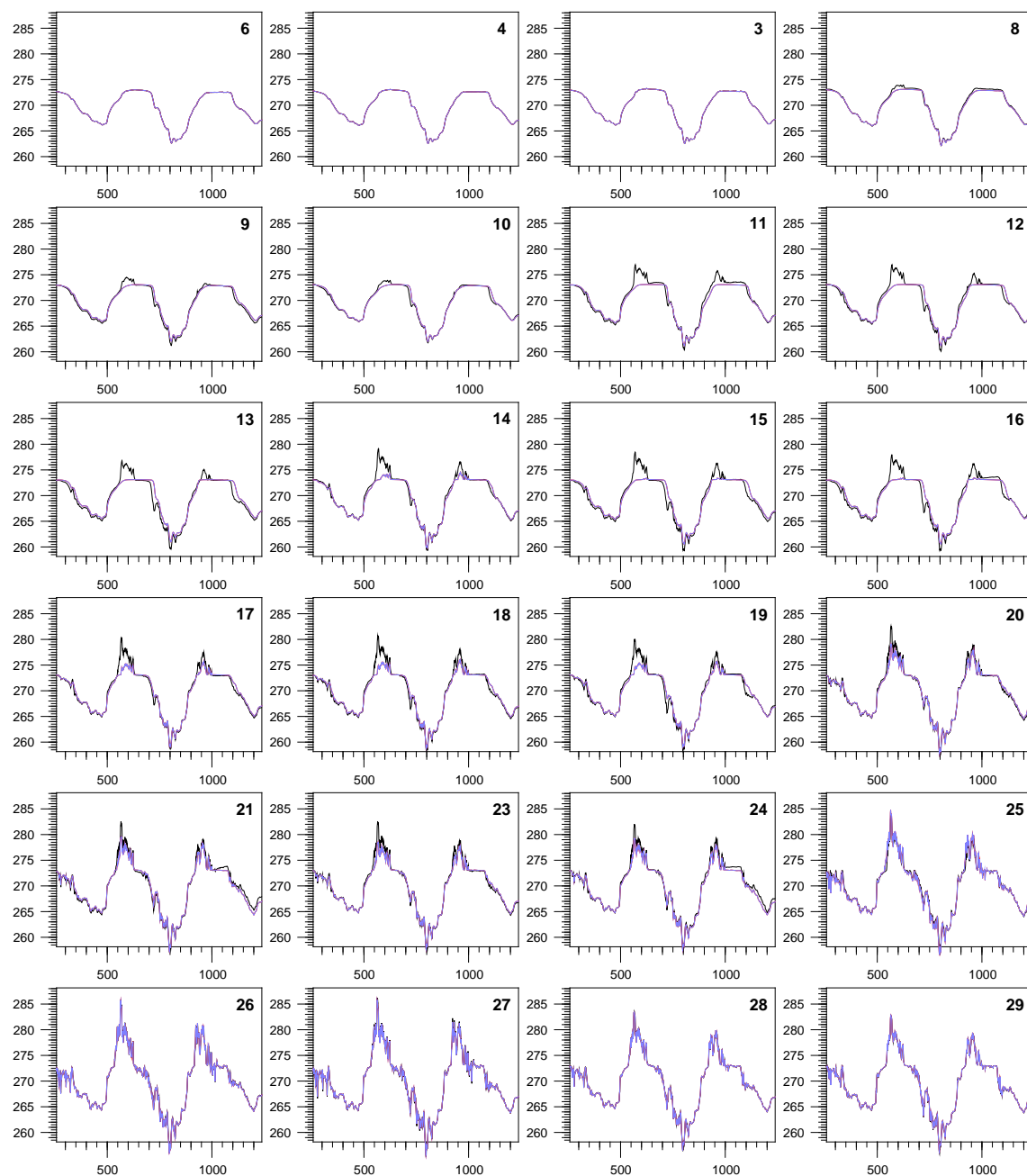
Relative Permittivity
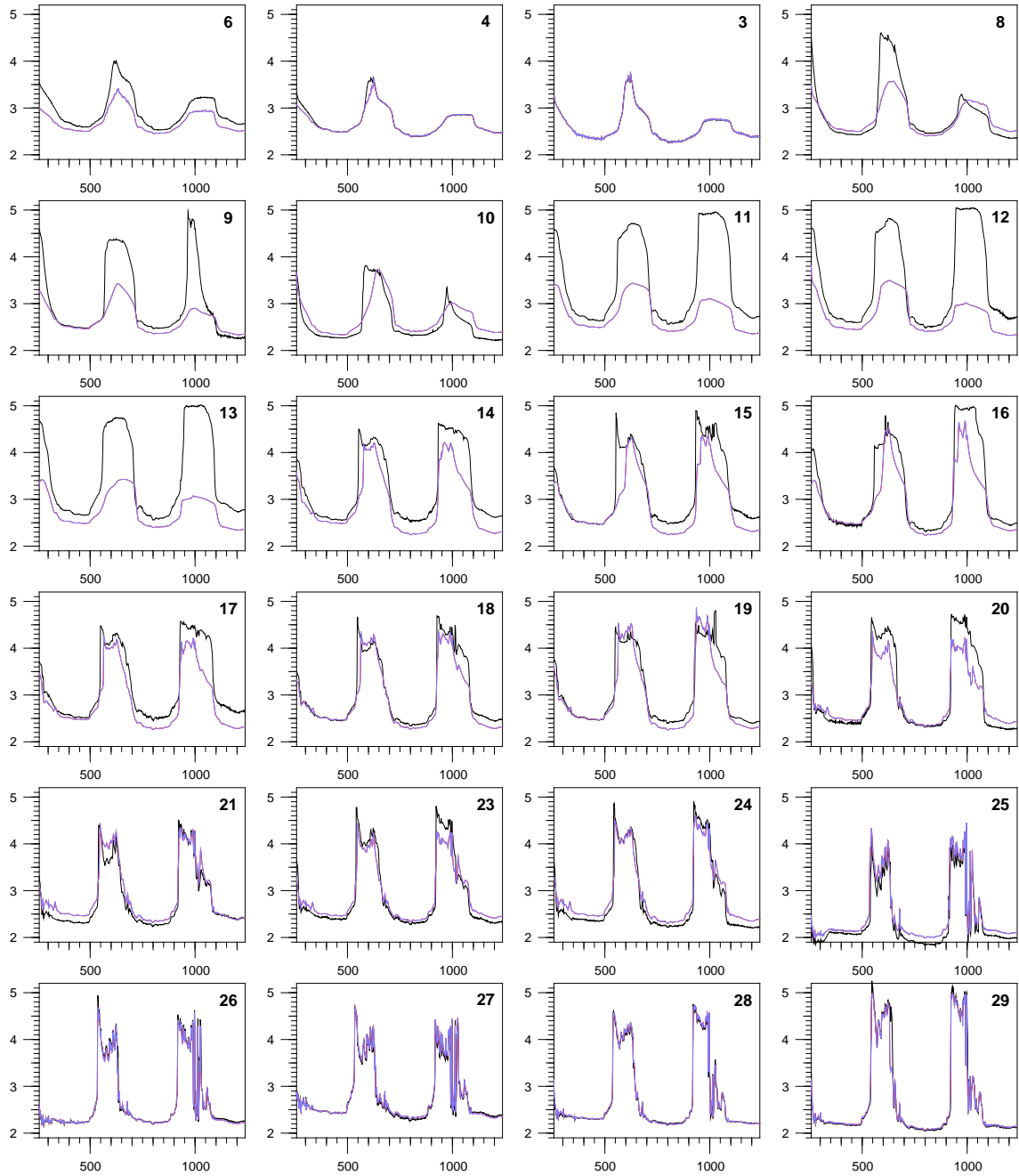
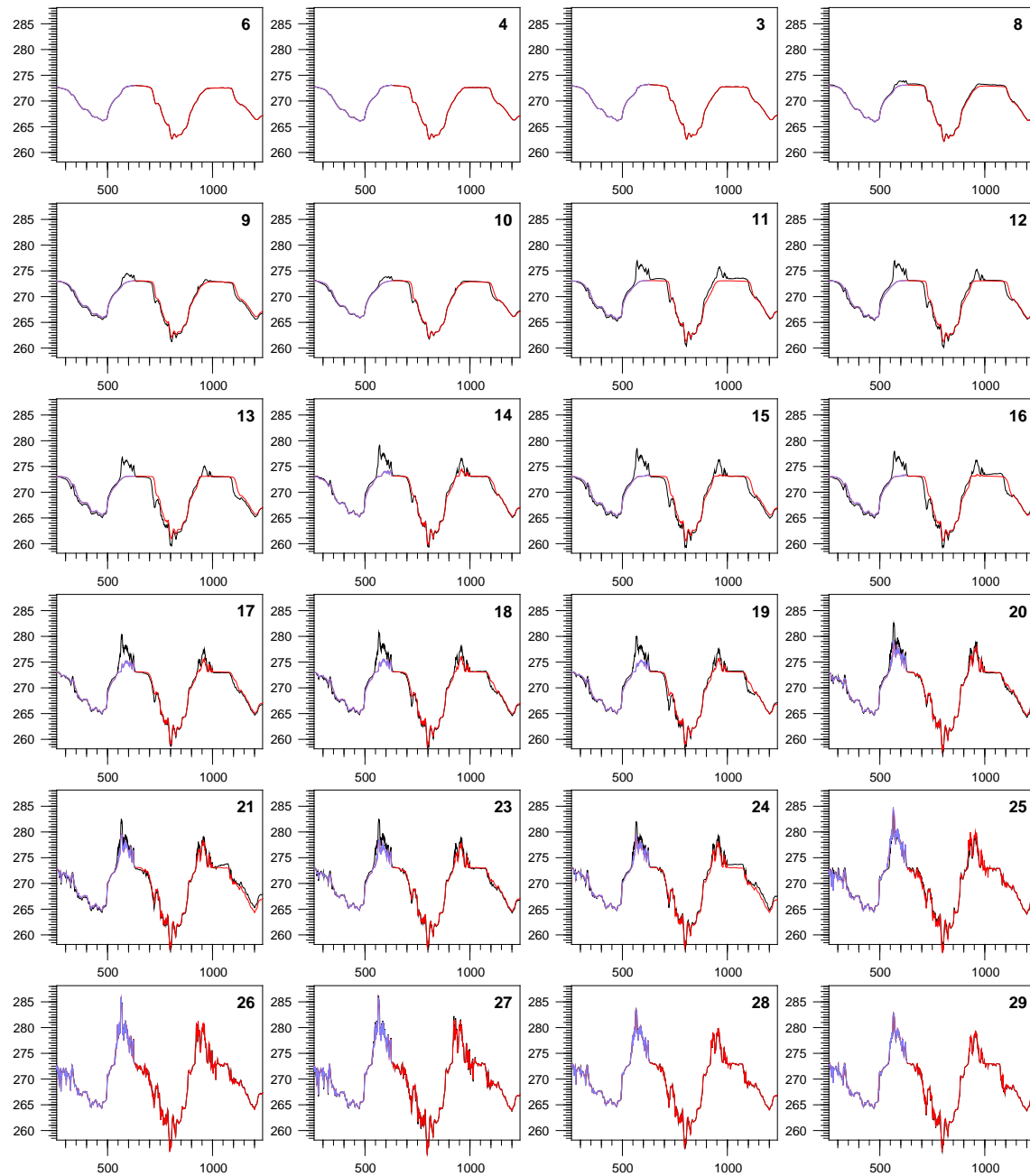# E.11.   Loam with Vapor Transport Formulated According to Philip and de Vries
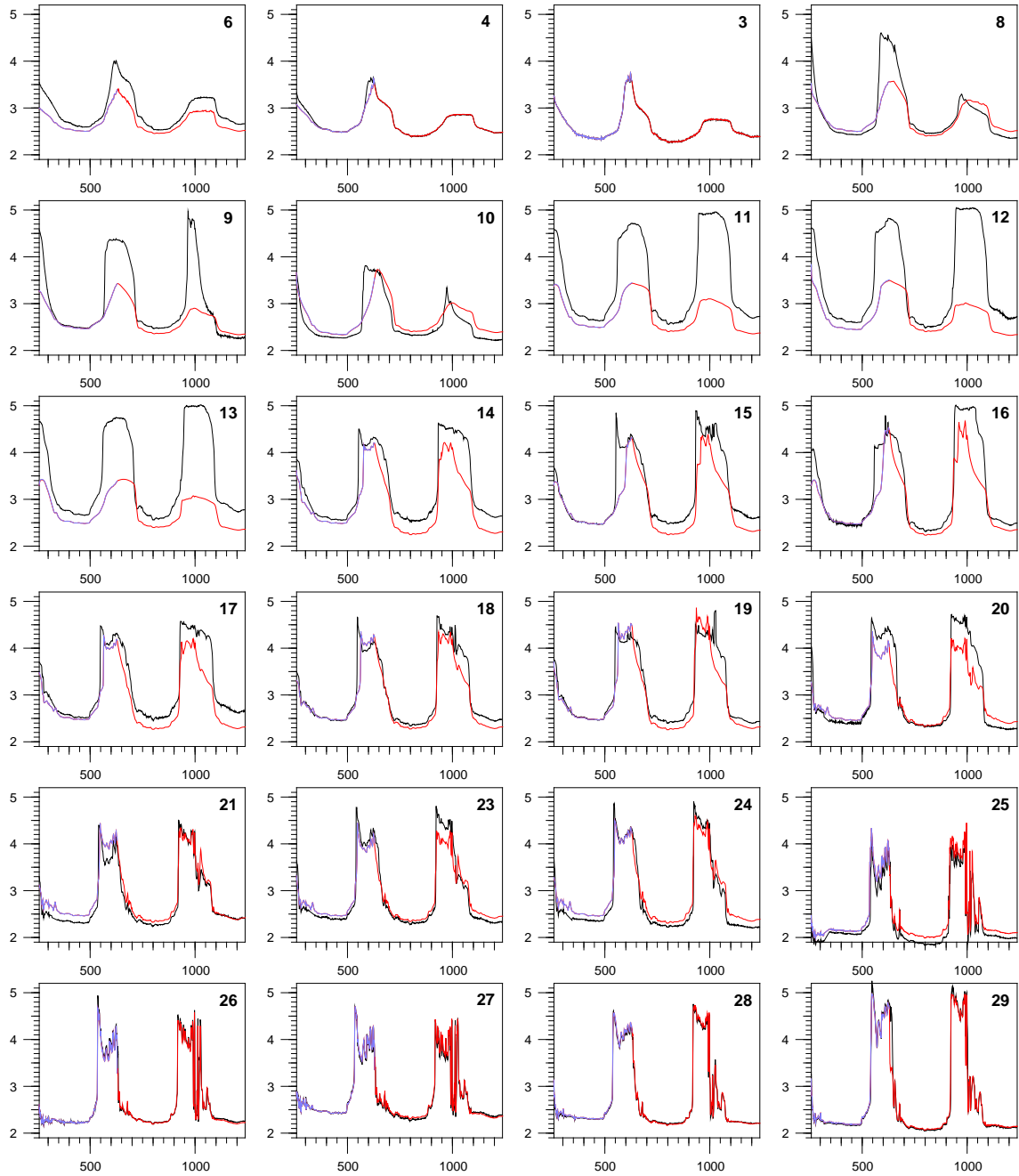
Temperature
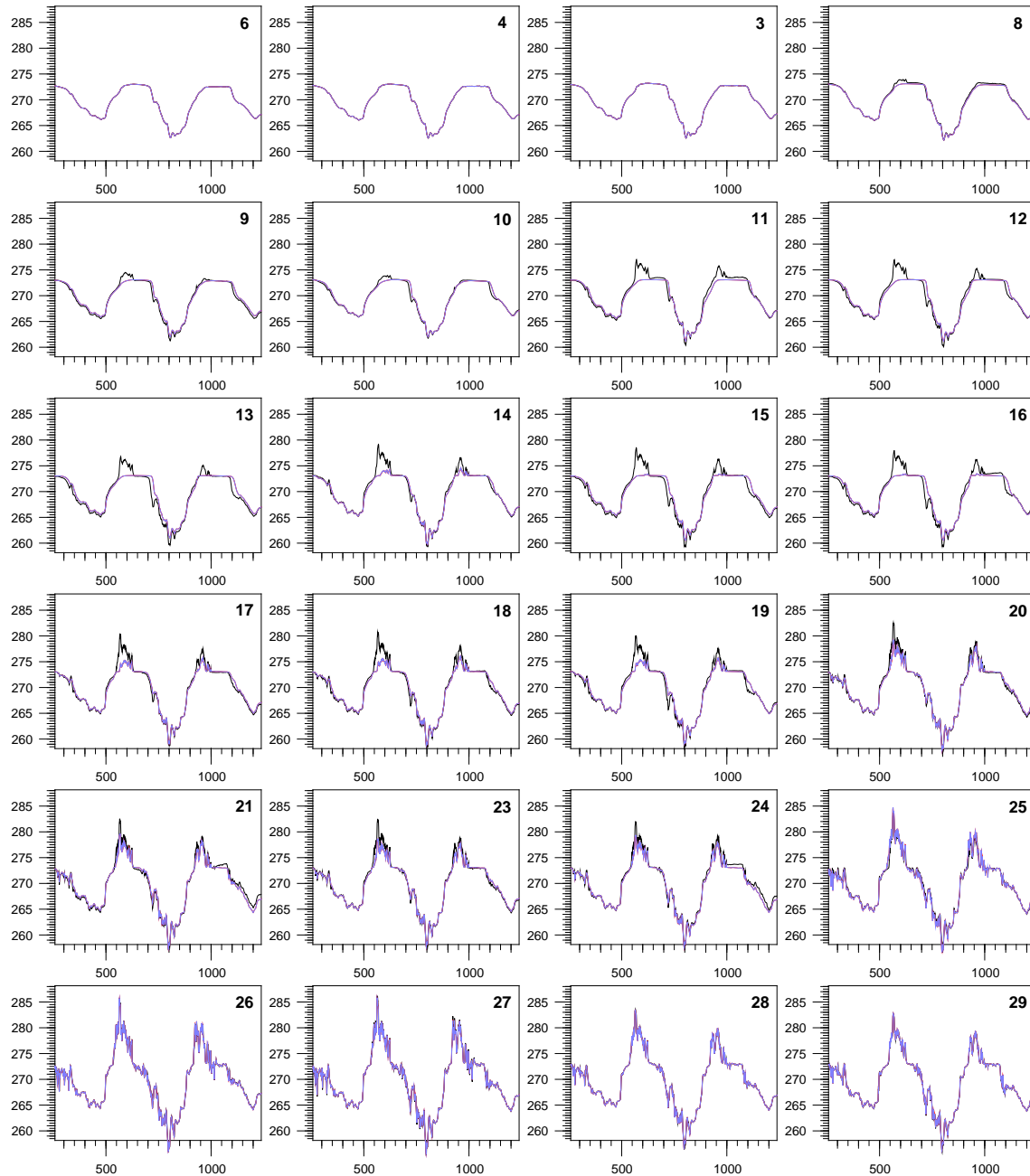
Relative Permittivity
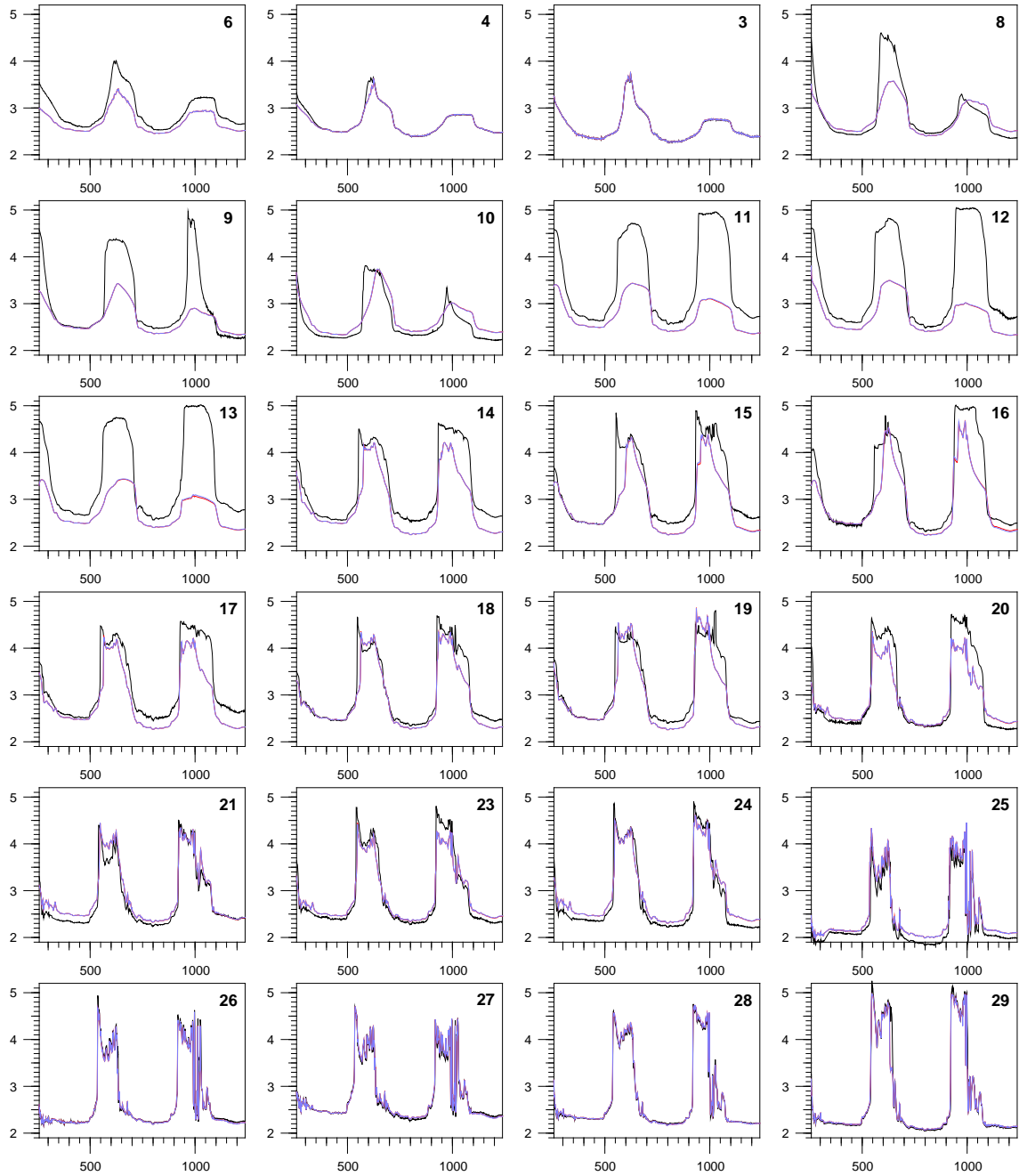
E.12. Loam with Inclusion of Solute Transport
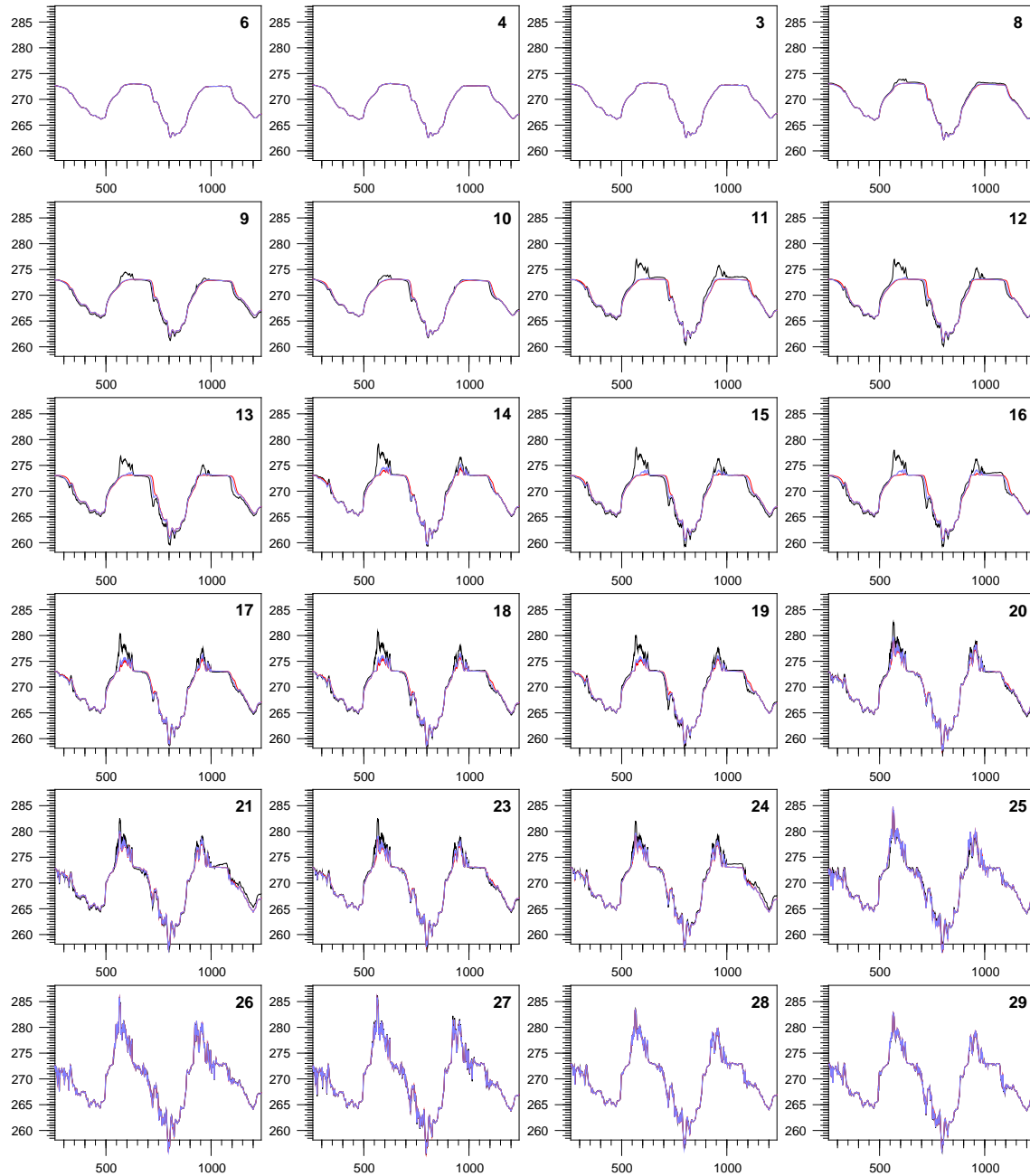
Temperature

Relative Permittivity

E.13.   Heterogeneous Simulation

Temperature

Relative Permittivity